2009

Estuarine Influence On Tidally Driven Circulation In The South Atlantic Bight

Peter Bacopoulos
University of Central Florida

ESTUARINE INFLUENCE ON TIDALLY DRIVEN CIRCULATION IN THE SOUTH ATLANTIC BIGHT

by

PETER BACOPOULOS
B.S. University of Central Florida, 2003
M.S. University of Central Florida, 2005

A dissertation submitted in partial fulfillment of the requirements
for the degree of Doctor of Philosophy
in the Department of Civil, Environmental, and Construction Engineering
in the College of Engineering and Computer Science
at the University of Central Florida
Orlando, Florida

Fall Term
2009

Major Professor: Scott C. Hagen

ABSTRACT

A high-resolution, finite element-based, shallow water equation model is developed to simulate the tides in the South Atlantic Bight. The model is constructed to include all of the estuarine features along the southeastern United States seaboard: coastal inlets, rivers and tidal creeks, sounds and lagoons, intertidal zones including salt marshes and mangrove swamps, and the Atlantic Intracoastal Waterway. The estuaries are represented in the finite element mesh using triangular elements with side lengths on the order of tens of meters. Also incorporated into the model is a spatially distributed bottom friction parameterization, based on the various landcover and benthic characteristics in the domain. The motivation to use this comprehensive representation of the system was inspired by a desire to capably account for the full estuarine tidal physics. In this approach, no calibration is performed and the model is used as a tool to assess the physical processes it describes.

Upon its development, the model is first validated by accurately simulating tidal hydrodynamics in the South Atlantic Bight including the described estuaries. Variants of the model are then constructed by selectively removing estuarine features from the domain. All model representations are subsequently applied in nearly identical simulations: the only differing factor between the simulations being the inland extent of the estuaries described. The solutions are compared with respect to including versus excluding the estuarine features of the domain. Where water surface elevations are shown to be unaffected by the estuarine features of the South Atlantic Bight, tidal velocities exhibit far more sensitivity. This effect is pronounced locally, with regional effects extending offshore. Further analysis is performed on cross-sectional flows

recomposed locally and on tidal energetics diagnosed throughout the domain. It is discovered that the high frictional environment of the vast estuarine surface area plays a role in local and regional tidal circulation in the South Atlantic Bight.

ACKNOWLEDGMENTS

Foremost, I acknowledge my family for their continued love and support. This dissertation would not have been possible without them: parents, Peter and Eleanor, and twin brother, Kenny. Thank you for always being there for me.

I am grateful to my advisor and committee chair, Scott Hagen, for the many opportunities he has shared with me. In short, we operate together as an excellent team and have built a strong work and personal relationship from doing so. I also thank the other committee members: Lakshmi Reddi, George Yeh, Manoj Chopra, and Alain Kassab. I have had the fortune to interact with each of them on a variety of topics. The advice received from the committee strengthened this dissertation overall.

"UCF stands for opportunity." I acknowledge this as fact and thank the greater community as a whole for enabling the opportunities. Thank you Drs. Young and Georgiopoulos for the opportunities through UCF EXCEL: http://www.excel.ucf.edu/. Thanks to the department for the opportunity to teach the undergraduate hydrology course for three semesters and for other opportunities. Thanks to the UCF Institute of Simulation and Training (IST) for the opportunity to use their computing resources. I send special thanks to Sergio Tafur at IST for his close attention to my needs. Sergio was always quick to assist.

Many thanks to the UCF CHAMPS Laboratory (http://www.champs.cecs.ucf.edu/). My tenure there was lengthy and I am grateful to have shared experiences with the lab's former members: Daniel Dietsche; Yuji Funakoshi, Satoshi Kojima, David Coggin, and Mike Salisbury; Michael Parrish; Qing Wang and Naeko Takahashi; and Derek Giardino. I thank the active

members of the lab: Alfredo Ruiz, Hitoshi Tamura, Lillie Thomas, Matthew Bilskie, and Daina Smar. I especially thank Stephen Medeiros for all the knowledge he has shared firsthand with me. Stephen also deserves credit for his review of the dissertation. His feedback was very helpful.

I must also acknowledge those outside of UCF: Ethan Kubatko at The Ohio State University; John Atkinson at Arcadis, Inc.; Peter Sucsy of the St. Johns River Water Management District; David Scharff at the National Oceanic and Atmospheric Administration; Bill Dally of Surfbreak Engineering Sciences, Inc.; and Alan Zundel at Brigham Young University. These gentlemen have assisted on various issues both directly and indirectly. I am also very grateful to have collaborated with Vincent Cardone and Andrew Cox of Oceanweather, Inc. on a journal paper.

This study is funded in part under Award No. NA04NWS4620013 from the National Oceanic and Atmospheric Administration and the U.S. Department of Commerce, Contract No. SK91912 from the St. Johns River Water Management District, Contract No. 4500019382 from the South Florida Water Management District, and the U.S. Army Corps of Engineers, Jacksonville District, in support of the Jacksonville Harbor Deepening Project. The statements, findings, conclusions, and recommendations expressed herein are those of the author and do not necessarily reflect the views of National Oceanic and Atmospheric Administration, the U.S. Department of Commerce, the St. Johns River Water Management District, the South Florida Water Management District, the U.S. Army Corps of Engineers, Jacksonville District, or their affiliates.

TABLE OF CONTENTS

LIST OF FIGURES

LIST OF TABLES

CHAPTER 1. INTRODUCTION AND RESEARCH OBJECTIVE

The term South Atlantic Bight refers to the coastal zones found along the southeastern United States seaboard and more primarily the ocean region bounded to the west by the states of Florida, Georgia, and the Carolinas (Figure 1.1). The South Atlantic Bight coast is a heavily estuarine environment, consisting of coastal inlets, rivers and tidal creeks, sounds and lagoons, intertidal zones including salt marshes and mangrove swamps, and the Atlantic Intracoastal Waterway. Of course the estuaries are connected to the open ocean; however, on the inshore side the estuaries are hydraulically linked via the Atlantic Intracoastal Waterway such that the numerous inlets penetrate and interconnect the full range of the South Atlantic Bight coast. Intertidal zones, interspersed with tidal creek networks, provide additional hydraulic conduits within the South Atlantic Bight estuaries.

In the following dissertation, tidally driven circulation in the South Atlantic Bight is studied using the shallow water equations code ADCIRC-2DDI. A model is constructed to include all of the estuarine features along the southeastern United States seaboard. To do this, finite elements are used, which are at an unprecedented level of resolution on the order of tens of meters throughout the estuaries. This comprehensive representation of the system is motivated by a desire to capably account for the full estuarine tidal physics. Afterward, a spatially distributed bottom friction parameterization, based on the various landcover and benthic characteristics in the domain, is incorporated into the model. The end result is a calibration-free modeling tool that can be used to assess the physical processes it describes.

Figure 1.1. South Atlantic Bight: the coastal and ocean region off the states of the Florida, Georgia, and the Carolinas.

It should be noted that it is common practice to calibrate tidal models, which do not include a high-resolution description of the estuarine features, to observed water levels taken from stations along the coast. Since the observational data contain influence from the estuarine features, it must be recognized that to adjust a tidal model without the estuarine features included to such observational data will result in some of the described physics being enveloped into the calibration parameters. More so, much of the calibration exercised in tidal modeling is with water levels. Using this approach, excluding the estuarine features seems to produce an accurate solution along the coast. It is therefore assumed that the solution, both in water level and velocity, is around that level of accuracy domain-wide. By this, the model can be calibrated until the water levels are satisfactorily simulated at the coastal stations; however, this can result in degradation of the solution elsewhere in the domain.

This dissertation exemplifies how the above approach can lead to non-first principle-based solutions of the physics, particularly with simulated tidal currents. Foremost, the comprehensive high-resolution model constructed herein is established to accurately simulate tidal hydrodynamics in the South Atlantic Bight including the described estuaries. Next, variants of the model are developed by selectively removing estuarine features from the domain. All model representations of the domain are then applied in nearly identical simulations: the only differing factor between the simulations being the inland extent of the estuaries described. The solutions are compared with respect to including versus excluding the estuarine features of the South Atlantic Bight. Tidal velocities are shown to be appreciably more sensitive than water surface elevations with regard to the influence caused by the South Atlantic Bight estuaries, although the intertidal zones are also shown to influence simulated water surface elevations. In addition, cross-sectional flows are recomposed locally and tidal energetics are diagnosed

throughout the domain to further illustrate the estuarine influence. Overall, this dissertation elucidates how the increased dissipation in the estuaries plays a role in local and regional tidal circulation in the South Atlantic Bight.

CHAPTER 2. MODELING PHILOSOPHY AND SCIENTIFIC HYPOTHESIS

2.1. Verification, Validation, and Calibration

Verification is "the process of determining that a computational model accurately represents the underlying mathematical model and its solution" (American Society of Mechanical Engineers, 2006). Verification deals with mathematics and algorithms. Kinnmark (1985) provides an excellent overview of the shallow water equations with regard to their mathematical and algorithmic development. Verification issues include: 1) the fidelity of mapping the mathematical model; and 2) the accuracy of the calculation. In the context of the shallow water equations, the former deals with the discrete representation of the continuous equations and the latter deals with the solution algorithms used to solve the discrete mathematical problem.

Validation is "the process of determining the degree to which a model is an accurate representation of the real world from the perspective of the intended uses of the model" (American Society of Mechanical Engineers, 2006). Validation deals with physics. Werner and Lynch (1987) demonstrate a blind (uncalibrated) validation exercise using finite element-based solutions to the shallow water equations and include references to other such validation studies. Validation issues include experimental activities: initial and boundary conditions; response measurements; and uncertainty assessment. In the context of shallow water modeling, the major validation issue that arises is with data and its implementation in the modeling process.

Calibration is "the process of adjusting physical modeling parameters in the model to improve agreement with experimental data" (American Society of Mechanical Engineers, 2006).

When assessed accuracy of a model is inadequate, calibration takes place. Certainly the practice of calibration occurs in the shallow water modeling community and is often justified. However, calibration can be misused when the model parameters are simply tuned to the point where they mask relevant physics that are absent from the model. With misuse by tuning of calibration parameters the model departs from being first principle-based.

2.2. Statements of Philosophy and Hypothesis

In this dissertation, a model is constructed for tidal simulation in the estuaries of the southeastern United States seaboard. The model is designed to accurately represent the regional geography. The modeling philosophy is such that the model parameters are never adjusted in order to improve the match to historical data. Parameter values used are either standardized in practice or justified by their physical relevance. Further, calibration of any of the models in this dissertation would invalidate the methodology and thus the results and the interpretations thereof. Instead, the validation process involves comparing calibration-free model results to observations and the analysis involves interpreting model solutions that are first principle-based.

To follow, the scientific hypothesis of this dissertation is: where the coastline perforations of the southeastern United States seaboard have been shown to affect the tidal hydrodynamics locally and regionally (Blanton et al., 2004; Bacopoulos and Hagen, 2009), the interconnectedness of the system and increased dissipation present in the intertidal zones plays a direct role in the tidal hydrodynamics. Furthermore, although the estuaries are marginal features with regard to the greater geography of the region, they are physically relevant in local and regional tidal processes.

CHAPTER 3. SOUTH ATLANTIC BIGHT

3.1. Geological and Geographical Setting

The continental shelves of the western North Atlantic Ocean are characteristically wide and shallow. Sharp slopes at the edges are another signature to the Atlantic-basin shelves. The east coast of the United States exhibits these geological properties. The coastlines of Florida, Georgia, and the Carolinas form a natural cusp in the regional geology and define the land boundary of the South Atlantic Bight (Figure 3.1). From the South Atlantic Bight coast, the inner continental shelf (herein alternatively referred to as the nearshore region) extends out to the 25-m isobath. From there, the midshelf spans out to depths of 50 m, beyond which extends the outer shelf out to the break, defined at the 150-m isobath. The width of the shelf is variable in the latitudinal direction, with the maximum cross-shelf length (of more than 120 km) found east of Georgia and the minimum cross-shelf length (of less than 10 km) found east of southeastern Florida. On the shelf, bathymetric contours run parallel to the coast. Seaward of the shelf break lies Blake's Plateau: a large expanse of relatively flat submarine floor, which drops off abruptly at the 1200-m isobath. Beyond the edge of Blake's Plateau is the deep ocean on to the abyssal plain.

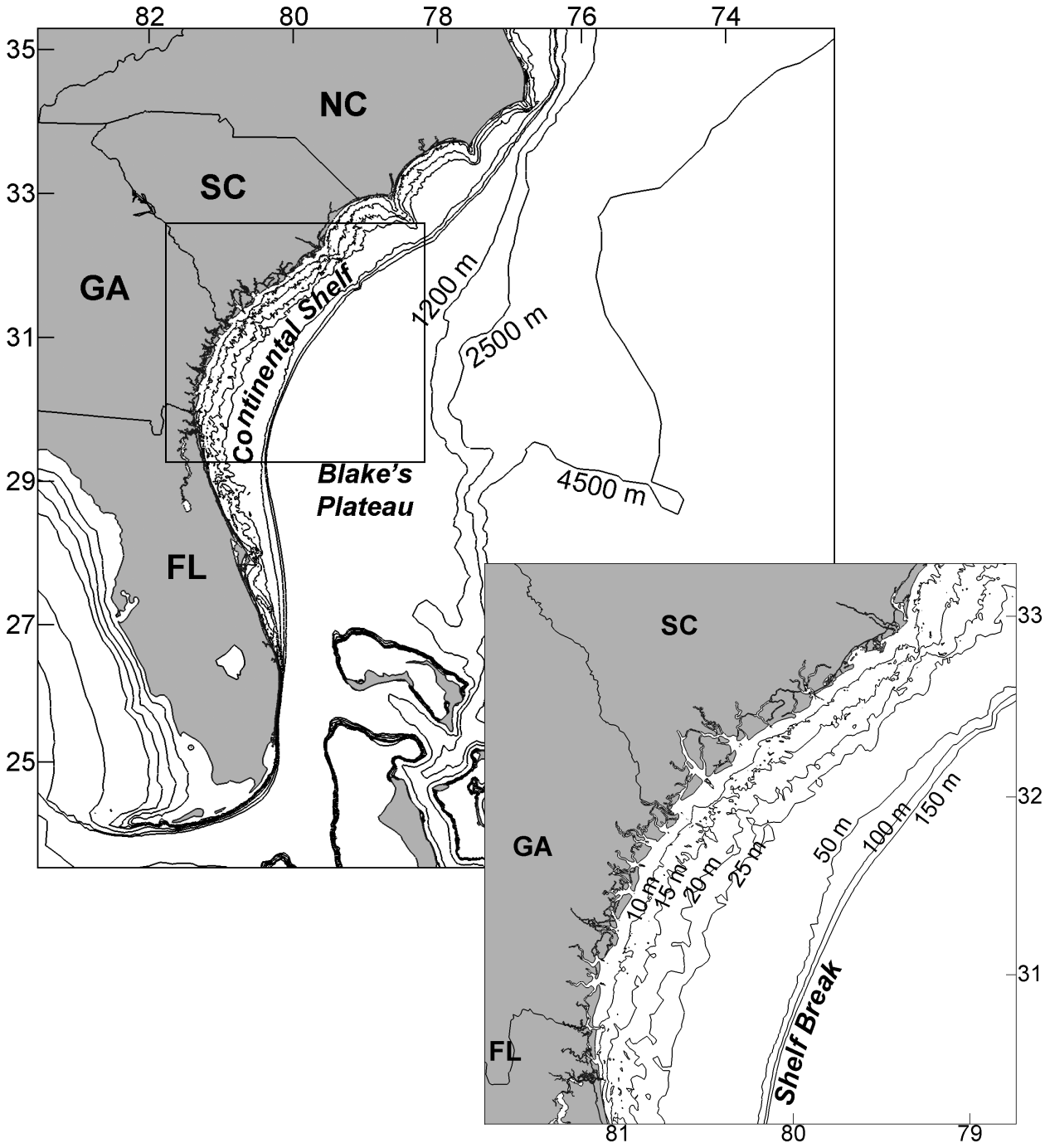

Figure 3.1. Depths in the South Atlantic Bight: the 10-, 15-, 20-, 25-, 50-, 100-, 150-, 1200- (edge of Blake's Plateau), 2500-, and 4500-m isobaths are displayed. The inset follows from the box in the larger view.

3.2. Oceanographic Setting

Unlike other shelf regions, the South Atlantic Bight does not have a clearly defined mean circulation, but instead exhibits variability. Boicourt et al. (1998) explain that observed mean circulation is a climatological average of the variability driven by atmospheric forcings and by offshore fluctuations in the Gulf Stream, rather than it being a product of a consistent, large-scale pressure gradient. The exception to this is the inner shelf, which is characterized by an along-shelf band of low-salinity stratified waters near the coast formed by freshwater river runoff (Blanton, 1980; Blanton and Atkinson, 1983). This, combined with local winds, contributes to nearshore circulation in the South Atlantic Bight (Blanton, 1981). Circulation at the midshelf is mainly the result of synoptic-scale pressure systems (Blanton et al., 1985). Circulation on the outer shelf is the most variable in the region due to meanders in the Gulf Stream (Lee et al., 1984; Atkinson and Menzel, 1985).

3.3. Tidal Signature

Tabeau and Lee (1979) and Lee and Brooks (1979) determined that the variance in the tidal frequency band accounts for 80 – 90% and 20 – 40% of the cross-shelf and along-shelf current variance, respectively, at the midshelf. Pietrafesa et al. (1985) identified a partitioning of the cross-shelf current variance, with semi-diurnal frequencies accounting for 75 – 90% of the total energy in the nearshore regions and at the midshelf, and 30% of the total energy in the outer shelf.

Table 3.1 shows the M2 tidal constituent as the dominant frequency in the South Atlantic Bight. Tidal response in the western North Atlantic Ocean is chiefly semi-diurnal, because the basin dimensions give it a natural period of oscillation near the M2 frequency (refer to Appendix A). On the shelf, tides are primarily a co-oscillation with the M2-dominated ocean tide (Redfield, 1958). This suggests that the coastal water level at semi-diurnal frequencies is in phase, and that maximum shoreward tidal currents lead the time of high water by a quarter period.

Table 3.1. Principal tidal constituents in the South Atlantic Bight (after Pietrafesa et al. [1985]).

Constituent		Period	Percent contribution
Name	Symbol	(hr)	(normalized by M2 value)
Principal lunar	M2	12.42	100.0
Principal solar	S2	12.00	46.6
Larger lunar elliptic	N2	12.66	19.2
Luni-solar semi-diurnal	K2	11.97	12.7
Luni-solar diurnal	K1	23.93	58.4
Principal lunar diurnal	O1	25.82	41.5

Because of standing wave dynamics, the amplification of the coastal water level due to shelf width means that maximum amplification occurs at Georgia, where the shelf is widest in the region. M2 water level amplitudes are greatest at Georgia (1 m) and reduce north and south to slightly less than half this amount (Center for Operational Oceanographic Products and Services: website http://tidesandcurrents.noaa.gov/ accessed on March 15, 2008). Standing wave dynamics are also evident in the South Atlantic Bight by inspection of tidal ellipses (refer to Appendix B). M2 tidal ellipses are generally oriented cross-shelf, with minor semi-axis lengths

at about half the length of the major semi-axes (Clarke and Battisti, 1981). Maximum M2 currents at midshelf are greatest off the Georgia coast (30 cm/s) and, in a similar sense as water levels, reduce north and south to slightly less than half this amount (Pietrafesa et al., 1985). M2 tidal currents rotate clockwise except very near the South Atlantic Bight coast (Blanton et al., 2004).

3.4. Coastal Indentations

The South Atlantic Bight coast is punctuated by many coastal indentations, including bays, ports, harbors, and inlets. The inlets hydraulically connect the South Atlantic Bight estuaries to the open ocean. A total of 64 inlets are identified from Cape Lookout, North Carolina to the Florida Keys (Table 3.2). The orientation of each inlet is unique, in addition to its structural form, usually meaning with or without jetties. The following assessment does not examine such specific details, but instead generalizes the inlets based on the widths and coastline distances between adjacent inlets.

Table 3.2. Inlets (64 total) from Cape Lookout, North Carolina to the Florida Keys. Shaded rows are excluded from the inlet analysis (see related text). Text coloring is based on the geographical partitioning of the inlets: blue corresponds to inlets in the "central" category and red corresponds to inlets in the "north and south" category.

Inlet	State(s)	Width (m)	Depth (m)	Average coastline distance to adjacent inlets (km)
Bogue Inlet	NC	718	2.8	7.4
Bear Inlet	NC	798	3.5	5.7
Browns Inlet	NC	879	3.5	12.7
New River Inlet	NC	1298	2.4	35.9
New Topsail Inlet	NC	813	3.5	7.9
Middle Inlet	NC	413	3.5	8.4
Wrightsville Inlet	NC	661	3.5	8.1
Masonboro Inlet	NC	564	4.2	13.1
Myrtle Grove Inlet	NC	1165	3.5	35.5
Southport Entrance	SC	2314	6.1	21.9
Lockwoods Folly Inlet	SC	629	1.9	13.2
Shallotte Inlet	SC	811	1.9	10.5
Tubbs Inlet	SC	1036	2.2	7.3
Little River Inlet	SC	323	2.3	86.2
North Inlet	SC	1327	2.8	14.9
Winyah Bay Entrance	SC	1733	2.5	10.1
North Santee River Entrance	SC	1420	2.0	5.6
South Santee River Entrance	SC	510	2.0	33.8

Inlet	State(s)	Width (m)	Depth (m)	Average coastline distance to adjacent inlets (km)
Bulls Bay Entrance	SC	11077	1.7	17.5
Bull Island Pass	SC	845	0.8	5.3
Dewees Island Pass	SC	715	0.7	3.8
Wild Dunes Pass	SC	873	1.4	16.9
Charleston Harbor Entrance	SC	2320	6.4	18.0
Folly Island Pass	SC	3239	1.9	22.6
Wadmalaw River Entrance	SC	962	2.1	19.4
Edisto Inlet	SC	3642	1.8	8.0
St. Helena Inlet	SC	9026	2.3	12.8
Hunting Island Pass	SC	2294	6.3	15.8
Old Island Pass	SC	710	2.8	6.8
Port Royal Inlet	SC	4358	3.5	26.0
Tybee Roads Entrance	SC/GA	10517	4.7	10.4
Little Tybee Island Pass	GA	616	1.9	10.2
Wassaw Inlet	GA	3650	2.3	13.2
Ossabaw Inlet	GA	6361	2.6	18.5
St. Catherine Inlet	GA	3280	3.2	20.8
Sapelo Inlet	GA	3847	2.7	21.1
Doboy Inlet	GA	3349	3.1	6.9
Altamaha River Entrance	GA	4017	1.9	12.7
Little St. Simon Island Pass	GA	673	2.7	8.7
Sea Island Pass	GA	425	3.6	5.3
St. Simon Inlet	GA	1554	3.9	15.1
St. Andrew Inlet	GA	4165	3.0	36.4
St. Mary’s Inlet	GA/FL	721	4.4	24.9

Inlet	State(s)	Width (m)	Depth (m)	Average coastline distance to adjacent inlets (km)
Nassau Inlet	FL	3162	1.4	10.7
Fort George Inlet	FL	342	1.6	3.6
Mayport Entrance	FL	324	14.2	56.9
St. Augustine Inlet	FL	555	4.1	23.3
Matanzas Inlet	FL	140	4.0	77.3
Ponce de Leon Inlet	FL	590	3.8	164.2
Port Canaveral Entrance[a]	FL	–	–	–
Sebastian Inlet	FL	168	7.5	46.4
Fort Pierce Inlet	FL	257	8.3	37.6
St. Lucie Inlet	FL	892	5.5	26.0
Jupiter Inlet	FL	99	5.0	19.4
Lake Worth Inlet	FL	200	3.5	25.2
South Lake Worth Inlet	FL	29	4.8	23.4
Boca Raton Inlet	FL	45	4.8	8.8
Hillsboro Inlet	FL	84	4.5	18.4
Port Everglades Entrance	FL	226	2.8	22.0
Bakers Haulover Canal	FL	109	1.8	16.1
Government Cut	FL	220	3.8	2.2
Norris Cut	FL	671	1.0	2.6
Bear Cut	FL	1104	1.2	24.8
Biscayne Bay Entrance	FL	32761	3.3	164.2

[a] Not hydraulically connected to the South Atlantic Bight estuaries.

Inlet widths are assessed: Port Canaveral Entrance is excluded because it is not hydraulically connected to the estuaries; and Bulls and Biscayne Bays are excluded because their

inlets are excessively wide compared to the overall population. A geographical partitioning of the 61 inlets then splits the overall population into two sets (Figure 3.2): 1) "central" includes 27 inlets south from Winyah Bay Entrance to Mayport Entrance; and 2) "north and south" includes 34 inlets either north or south of those marked as "central." The "central" inlets occupy the Georgia coast, including a small portion of northeastern Florida, along with the southern two-thirds of the South Carolina coast: 450 km total. The "north and south" inlets occupy most of Florida's east coast, the northern South Carolina coast, and the North Carolina coast to Cape Lookout, North Carolina: 1,050 km total.

The widths corresponding to the "central" and "north and south" inlets are plotted as a histogram (Figure 3.2, inset). The "central" inlets are wider than the "north and south" inlets. The distribution of "central" inlet widths is double-peaked at the 500 – 1000 m and 3500 – 5000 m bins: 9 and 6 inlets per bin, respectively. The average width of the "central" inlets is 2861 m with a standard deviation of 2495 m. The distribution of "north and south" inlet widths is right-skewed with 15 and 12 inlets per bin in the < 500 and 500 – 1000 m bins, respectively. The average width of the "north and south" inlets is 633 m with a standard deviation of 511 m.

The density of inlets along the coast is also variable. The measure used herein is based on the coastline distance between adjacent inlets. At a given inlet, the average coastline distance to its adjacent inlets (Table 3.2) is computed as the average of the two coastline distances to its adjacent inlets. Using the geographical partitioning of the inlets, the average "average coastline distance to adjacent inlets" for the "central" inlets is 15 km with a standard deviation of 6 km; and is 26 km with a standard deviation of 25 km for the "north and south" inlets. Although there are fewer "central" inlets (27) than "north and south" inlets (34), they still more densely populate the coast since they occupy less coastline distance (450 km versus 1,050 km).

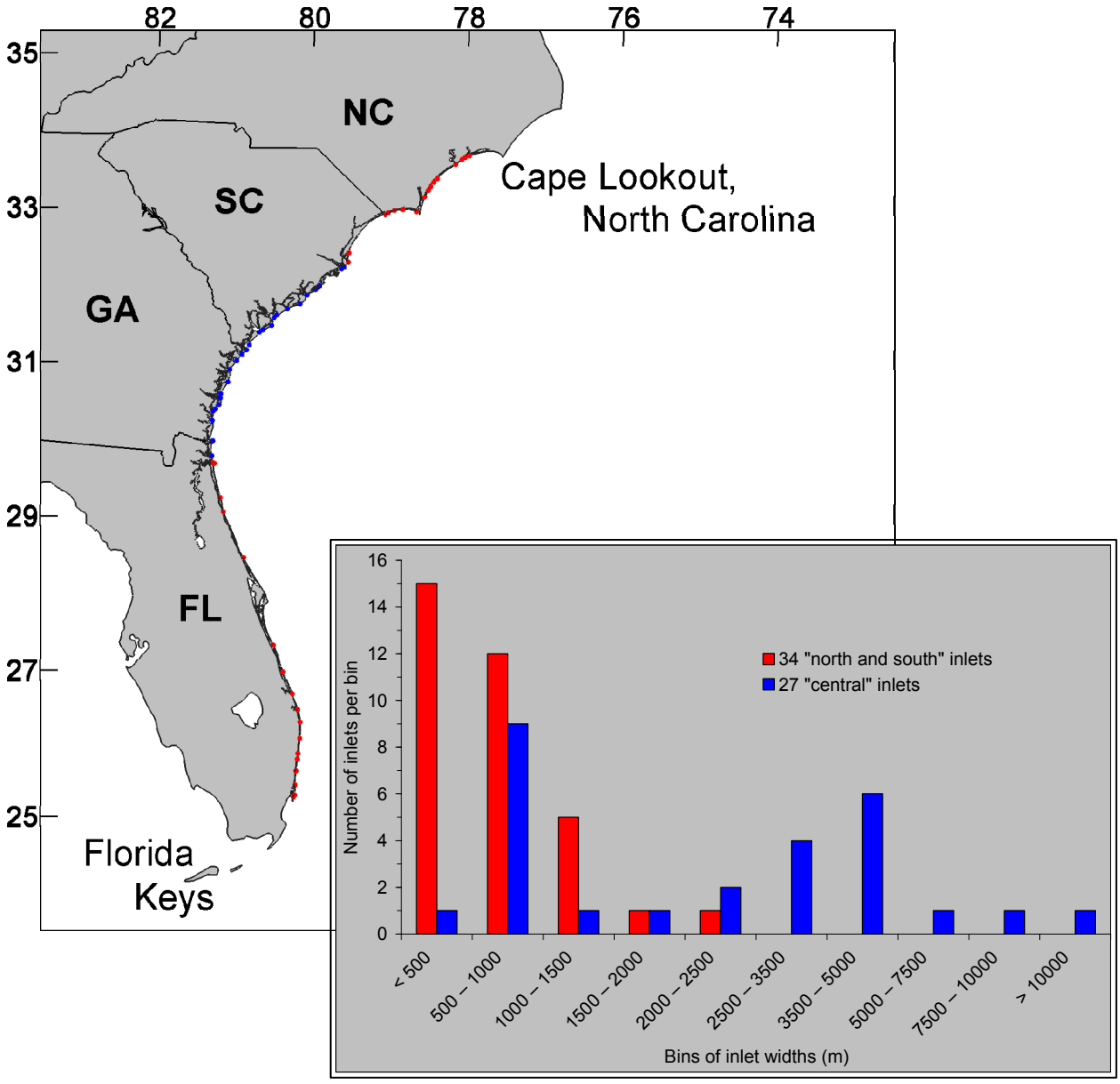

Figure 3.2. Geographical partitioning of 61 inlets from Cape Lookout, North Carolina to the Florida Keys: blue identifies inlets in the "central" category and red identifies inlets in the "north and south" category (see related text). (inset) Histogram of widths corresponding to the "central" and "north and south" inlets.

3.5. Estuarine Features

The southeastern United States seaboard is a broad coastal plain bordered with barrier islands and beaches interspersed with tidal inlets and rivers. Dame et al. (2000) divide the southeastern coastal plain of the United States into two geographical regions: 1) the South Atlantic Bight, which they define from Cape Hatteras, North Carolina to Cape Canaveral, Florida; and 2) the southeastern Florida coast, stretching from Cape Canaveral to the Florida Keys.

Along the South Atlantic Bight coast, tidal creek networks and intertidal zones occupy the low elevation areas between the mainland and the barrier islands. The intertidal zones attain their greatest width (approximately 12 km) at the apex of the South Atlantic Bight: roughly located at the state border between Georgia and South Carolina. Rivers of piedmont and coastal plain origin (defined shortly hereafter) dot the coast and contribute fluvial discharge to the South Atlantic Bight estuaries.

Two major estuarine systems occupy the southeastern Florida coast: 1) the Indian River lagoon; and 2) Biscayne Bay. The Indian River lagoon can be demarcated into three main waterbodies: 1) Mosquito Lagoon to the north; 2) the Banana River lagoon in the central; and 3) the Indian River lagoon proper through the central into the south. Further south, Biscayne Bay is bounded to the north by Dumfoundling Bay and to the south by Florida Bay.

Dame et al. (2000) identify three types of estuaries for the southeastern coast of the United States: 1) bar-built; 2) coastal plain; and 3) piedmont. Bar-built estuaries, sometimes referred to as lagoonal systems, form behind offshore sandy barrier islands and usually drain small adjacent upland watersheds. Because of the protection by the barrier islands, wetlands are

extensive in bar-built estuaries. Vernberg et al. (1992) report that there are more than 320 small ($< 60 \times 10^6$) bar-built systems along the South Atlantic Bight coast.

The latter two estuaries, coastal plain and piedmont, are riverine. Coastal plain estuaries have rivers that drain watersheds contained completely within the coastal plain and are usually characterized by lower discharges. Because of the flat topography and vegetative environment, flow is typically sluggish in coastal plain estuaries. The St. Johns River in northeastern Florida is an example of a coastal plain estuary. Piedmont estuaries have rivers which drain larger watersheds at higher elevations, and are usually characterized by higher discharges.

Some estuaries exhibit mixed properties of the above: for example, Winyah Bay, South Carolina is a composite system of coastal plain rivers (Sampit, Black, and Waccamaw) and piedmont rivers (Little Pee Dee and Great Pee Dee). Table 3.3 presents the physical characteristics of the major estuaries located along the southeastern United States seaboard, which indicate the variability of the different systems. This list is only partial, but indicates a total estuary area of 3,234 km^2 for the estuaries listed. Depth and volumes are rather minimal because of the shallow water environment. In general, the estuarine features of the South Atlantic Bight are vast and relatively shallow.

Table 3.3. Physical characteristics of the major estuaries located along the southeastern United States seaboard (after Coastal Assessment and Data Synthesis System [1999]).

Estuary	State(s)	Drainage area (km^2)		Estuarine zones (km^2)			Estuary area (km^2)	Average depth (m)	Volume ($m^3 \times 10^9$)
		Estuarine	Fluvial	Tidal fresh	Mixing	Seawater			
Cape Fear River	NC	11176	12413	1	76	23	100	3.4	0.3
Winyah Bay/Pee Dee/Black Rivers	SC	24671	22288	12	59	17	88	3.0	0.4
North/South Santee Rivers	SC	1818	0	0	18	0	18	2.1	0.0
Charleston Harbor/Wando/Cooper/ Ashley Rivers	SC	3089	38028	1	58	25	84	4.9	0.6
St. Helena Sound/S. Edisto/Coosaw Rivers	SC	3809	8454	0	111	92	203	4.0	1.0
Savannah River	SC/GA	3263	24760	7	37	77	121	4.6	0.8
Ossabaw Sound/Ogeechee River	GA	3752	8381	11	39	38	88	4.0	0.4
Altamaha River	GA	3907	33055	5	29	5	39	3.4	0.1
St. Andrew/ St. Simon's Sounds/ Satilla River	GA	8219	2023	7	103	67	177	4.0	0.8
St. Mary's River/Cumberland Sound	GA/FL	4386	0	0	7	57	64	6.1	0.5
St. Johns River	FL	15840	7375	511	156	17	684	3.4	2.3
Indian River Lagoon	FL	3093	0	0	0	866	866	2.1	1.7
Biscayne Bay	FL	6746	0	0	94	608	702	2.4	1.6

Vascular plants common to the South Atlantic Bight estuaries include salt marshes, mangroves, and seagrasses. Along the Georgia coast and into South Carolina, *Spartina*[§] salt marshes dominate. Moving south into northeastern Florida, *Juncus*[†] begins to appear in the salt marshes. Table 3.4 lists the areal extents of the different salt marsh communities along the southeastern Atlantic coast. This list is fairly complete and indicates a total intertidal area of 4,238 km^2 in the southeastern United States seaboard.

Table 3.4. Distribution of salt marshes along the southeastern Atlantic coast.

State	Area (km^2)			Source
	Spartina	*Juncus*	Total	
North Carolina	429	407	836	Critcher (1967)
South Carolina	1128	369	1496	Alexander et al. (1986)
Georgia	1213	303	1517	Eleuterius (1976); Alexander et al. (1986)
Florida	105	283	388	Eleuterius (1976)

South of Daytona Beach, Florida, the black mangrove, *Avicennia germinans*, gradually replaces *S. alterniflora* in the intertidal zones (Dame et al., 2000). In southeastern Florida, the red mangrove, *Rhizophora mangle*, thrive in the ubiquitous saltwater regime. Seagrasses are found along Florida's east coast; the common species being Florida turtlegrass, *Thalassia testudinum*.

[§] *Spartina alterniflora*, or smooth cordgrass, is the dominant aquatic plant in the intertidal zones along the South Atlantic Bight coast (Wiegert and Freeman,1990). Higher production rates of *S. alterniflora* tend to be where tidal variability is greater in the region: much along the Georgia coast. Shoots can grow up to 3 m high and stem density can range from 30 to 300 stems/m^2, in the lower and higher marshes, respectively (Chalmers, 1982).

[†] *Juncus roemerianus*, or black needlerush, is a vascular plant community generally found along the fringes of brackish embayments (Marshall, 1974). The stands are typically small, commonly forming a narrow band adjacent to the shore of both the barrier island and mainland sides of the estuary (Eleuterius, 1976).

3.6. Atlantic Intracoastal Waterway

The Atlantic Intracoastal Waterway runs continuously along the southeastern United States seaboard (Figure 3.3). It consists of a system of canals and landcuts, free of human-operated controls, that hydraulically connects the estuaries along the South Atlantic Bight coast. Construction of the Atlantic Intracoastal Waterway was a long-term and expensive effort. The historical details are excluded from this chapter, but are presented elsewhere: overall in Parkman (1983) and The History Channel (2006); and with focus on Florida in Crawford (2006).

The geometric dimensions and physical properties of the Atlantic Intracoastal Waterway are fairly uniform along the South Atlantic Bight coast. The side banks narrow in the reaches between the estuaries to form channels of about 100 m wide. The Atlantic Intracoastal Waterway in these reaches, and in shallow sounds and lagoons, is maintained at depths generally at 3.5 m (Parkman, 1983). Otherwise, the channel takes advantage of deeper harbor waters and river entrances. The length of the Atlantic Intracoastal Waterway along the South Atlantic Bight coast is a continuous 1,500 km.

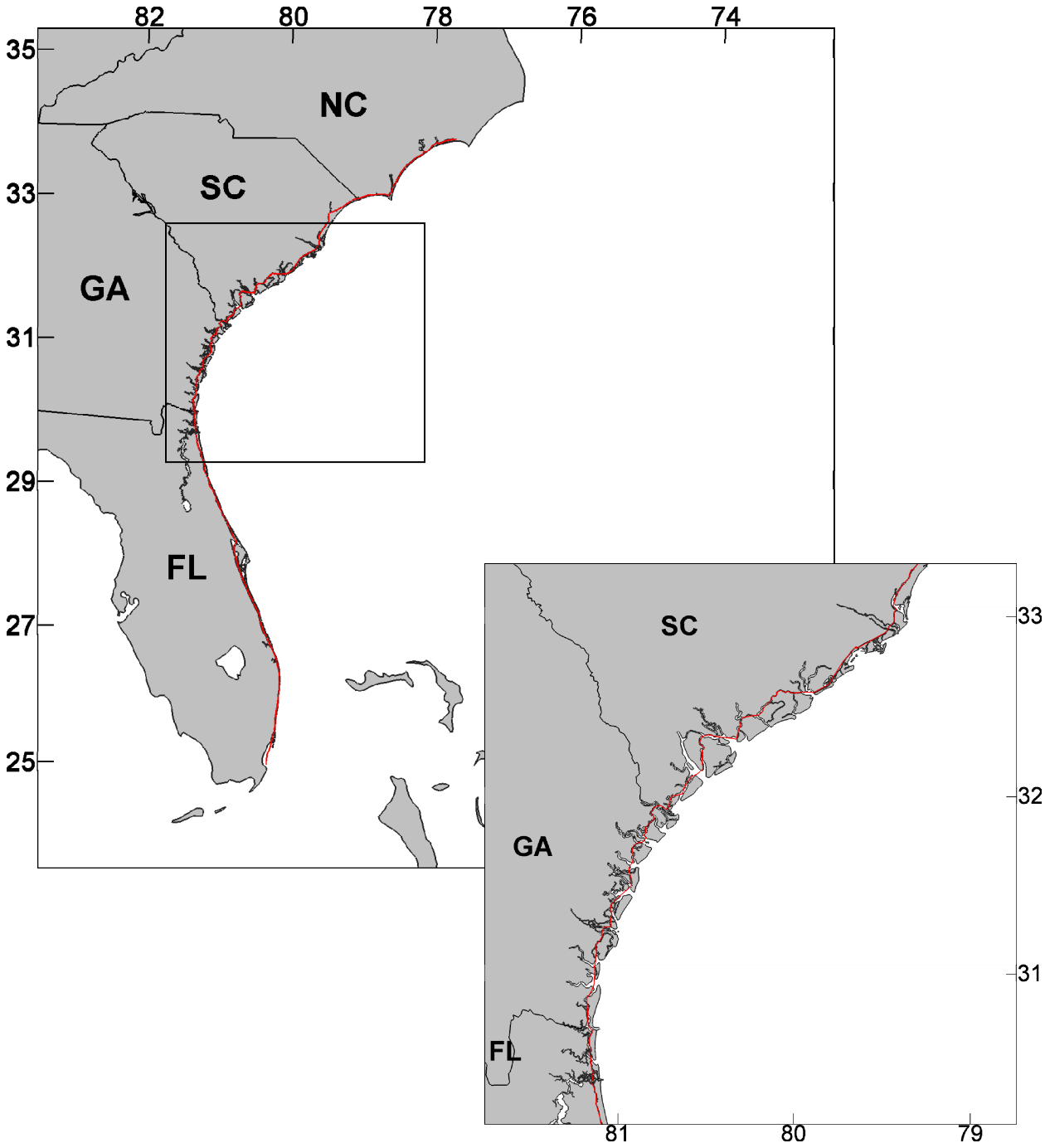

Figure 3.3. The 1,500 km of continuous length of the Atlantic Intracoastal Waterway along the South Atlantic Bight coast (displayed in red). The inset follows from the box in the larger view.

CHAPTER 4. LITERATURE REVIEW

4.1. Theory of Tidal Motions on Continental Shelves

The continental shelf and slope present a sharp perturbation in the nearly constant depth of the sea floor in the South Atlantic Bight. Because of this, the tide can be severely distorted over this topography. Clarke (1991) discusses an analytical treatment of the barotropic tide on "smooth" continental shelves where a shelf is considered to be "smooth" if the coastline is quasi-straight (i.e., curvatures in the coastline have horizontal scales much greater than the width of the shelf). In the theoretical development, Clarke and Battisti (1981) and Clarke (1991) apply the Laplace tidal equations with frictional effects included. Direct tidal loading is neglected under the assumption that it is minimal. Coriolis effects are considered in the approach, which leads to the shelf theory of the tides.

Clarke and Battisti (1981) describe the tendency of semi-diurnal tides to amplify on wide shelves located at midlatitudes in terms of a cross-shelf scale:

$$\nu = \left(\frac{\omega^2 - f^2}{g\alpha} \right) a \quad \ldots\ldots\ldots\

inertial (i.e., $\omega/f \approx 1$ or $\omega/f < 1$), the tide cannot propagate onto the continental shelf as an inertia-gravity wave, cannot constructively interfere, and hence does not amplify. For the South Atlantic Bight, assume its latitudinal center to be approximately 30°N ($f = 7.29\times10^{-5}$ rad/s ; taken from Pugh [2004]):

$$\frac{\omega_{\text{semi-diurnal}}}{f} = \frac{1.41\times10^{-4}\ \text{rad/s}}{7.29\times10^{-5}\ \text{rad/s}} = 1.93 > 1 \quad (\text{amplification will occur})$$

$$\frac{\omega_{\text{diurnal}}}{f} = \frac{7.29\times10^{-5}\ \text{rad/s}}{7.29\times10^{-5}\ \text{rad/s}} = 1.00 \approx 1 \quad (\text{amplification will not occur}) \quad \ldots\ldots (4.2)$$

where tidal amplification occurs only at the semi-diurnal frequency. Diurnal shelf tides will not amplify at this latitude.

Coriolis acceleration is also responsible for the right-deflecting (in the northern hemisphere) pattern of the tidal current. This acts to rotate the current vector in the clockwise direction in the northern hemisphere (the opposite occurs in the southern hemisphere):

$$\frac{d}{dt}v = -fu \quad \ldots\ldots (4.3)$$

where in the examples concerning the shelf theory of the tides, u and v relate to the cross- and along-shelf velocity components, respectively. Clarke and Battisti (1981) and Clarke (1991) add linearized frictional effects $\tau_b^y = \rho r v$ to the balance statement of Eq. (4.3):

$$\left(\frac{d}{dt} + \frac{r}{h}\right)v = -fu \quad \ldots\ldots (4.4)$$

where r denotes the resistance coefficient.

In the frictionless case (see Eq. [4.3]), when the Coriolis force $-fu$ is maximum, v is zero because it requires a quarter period to accelerate the water to maximum v. With frictional effects considered, a non-zero v results when $|u|$ is maximum (see Eq. [4.4]). Recognize that the maximum current is no longer when u is maximum (as it is in the frictionless case when $\omega/f > 1$). Thus, the semi-major axis of the tidal ellipse (refer to Appendix B) is rotated in the same direction of the Coriolis force (i.e., clockwise in the northern hemisphere and counterclockwise in the southern hemisphere). This is the case for semi-diurnal shelf tides at midlatitudes (i.e., when $\omega/f > 1$); the opposite is the case for diurnal tides[‡]. Bottom friction also tends to resist the inertial motion of the tidal current, which effectively narrows the tidal ellipse (Kundu et al., 1981).

The theory of tidal motions on continental shelves has been shown to perform well for the Atlantic coast of the United States (Battisti and Clarke, 1982). Clarke (1991), however, alludes to additional factors (not considered in the shelf theory of the tides) that may influence tidal currents on the continental shelf. In particular, he cites the irregularity of the coastline (not just in its geometry, but also in its perforation by shallow estuaries) as a physical complexity that is not presently accounted for in the shelf theory of the tides.

[‡] For diurnal shelf tides at midlatitudes (i.e., when $\omega/f \approx 1$ or $\omega/f < 1$), the minor semi-axes are directed cross-shelf in the frictionless case (see Eq. [4.3]). In case of friction, v is non-zero when $|u|$ is maximum, and the minimum current no longer occurs when $|u|$ is maximum, but instead, occurs earlier when $|u|$ is smaller. Thus, bottom friction causes the tidal ellipse axes to rotate counterclockwise in the northern hemisphere and clockwise in the southern hemisphere.

4.2. Nonlinearities in Shallow Waters

The two-dimensional momentum equations can be simplified for the *x*-direction as:

$$\underbrace{\frac{\partial}{\partial t}U}_{\text{Local acceleration}} + \underbrace{(U+V)\nabla U}_{\text{Advection}} - \underbrace{fV}_{\text{Coriolis effects}} + \underbrace{g\frac{\partial}{\partial x}\zeta}_{\text{Water level}} + \underbrace{\tau U}_{\text{Bottom stress}} = 0 \quad \ldots\ldots\ldots\ldots\ldots\ldots\ldots\ldots (4.5)$$

and for the y-direction as:

$$\underbrace{\frac{\partial}{\partial t}V}_{\text{Local acceleration}} + \underbrace{(U+V)\nabla V}_{\text{Advection}} + \underbrace{fU}_{\text{Coriolis effects}} + \underbrace{g\frac{\partial}{\partial y}\zeta}_{\text{Water level}} + \underbrace{\tau V}_{\text{Bottom stress}} = 0 \quad \ldots\ldots\ldots\ldots\ldots\ldots\ldots\ldots (4.6)$$

where U and V relate to the *x*- and *y*-velocities, respectively, and ζ corresponds to the water level height, relative to a datum. Eqs. (4.5) and (4.6) described in words: time-variance of local velocity ("local acceleration") is a function of the local spatial gradients of the water level and velocity fields ("water level" and "advection," respectively), rotational effects ("Coriolis effects"), and friction ("bottom stress"). To close the simplified equations of motion, mass conservation:

$$\frac{\partial}{\partial t}\zeta + \nabla H \cdot (U+V) = 0 \quad \ldots\ldots\ldots\ldots\ldots\ldots\ldots\ldots\ldots\ldots\ldots\ldots\ldots\ldots\ldots\ldots\ldots\ldots\ldots\ldots (4.7)$$

applies a balance between time-variance of local water level (first term) and local mass divergence (second term), where H is referencing the total height of the water column, which consists of a bathymetric depth h, relative to a datum, with the addition of the water surface deviation ζ, relative to the same datum.

Three nonlinear terms are present in the equations of motion (Parker, 1991): the mass divergence term* in the continuity equation (Eq. [4.7]) and the advection and bottom stress terms in the momentum equations (Eqs. [4.5] and [4.6]). The nonlinear continuity term includes the spatial gradient of the water mass ∇H. In shallow water $<< h$, the water surface deviation ζ contributes a non-negligible effect on the water mass $H = h + \zeta$. This distorts a progressive wave (refer to Appendix A) in shallow water because of faster propagating peaks and slower propagating troughs (Figure 4.1): $c = \sqrt{g(h+\zeta)}$ versus $c = \sqrt{g(h-\zeta)}$.

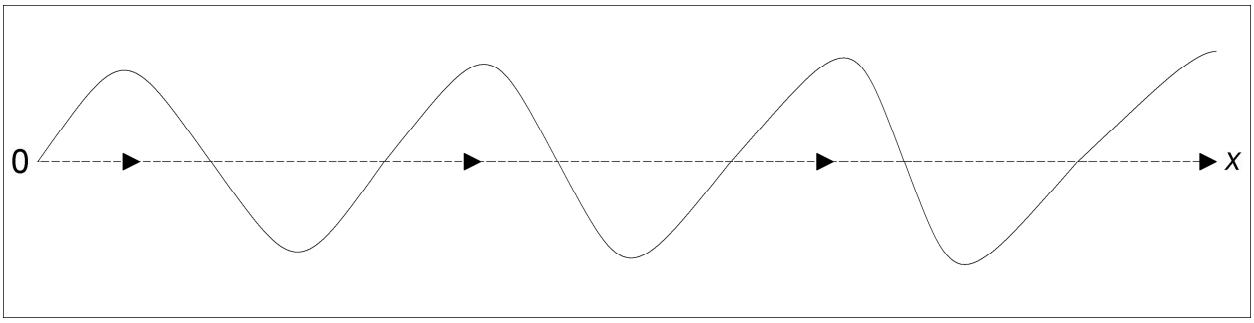

Figure 4.1. A progressive wave in shallow water distorted by faster propagating peaks and slower propagating troughs.

Advection relates to the interaction between a velocity $\mathbf{w}$ and the spatial gradient of the velocity $\nabla \mathbf{w}$. Distortion due to advection is similar to the effects caused by the nonlinear continuity term. Parker (1991) approximates the tidal current amplitude as a function of the wave speed: $u = \frac{\zeta}{h} c$. In shallow water $<< h$, the tidal current amplitude u is non-negligible

* Hereafter, "nonlinear continuity term" and "finite amplitude effects" will be used interchangeably for "mass divergence term."

with respect to the wave speed c, leading to faster propagating crests and slower propagating troughs: $c+u$ versus $c-u$.

Parker (1991) divides bottom friction effects into two nonlinear aspects: 1) $\zeta u|u|$ causes frictional loss per unit volume of fluid to be smaller for larger depths and to be larger for smaller depths; and 2) $u|u|$ causes maximum attenuation and minimum wave propagation speed at both maximum flood and maximum ebb (which coincides with high and low water, respectively, if the wave is progressive), with the opposite occurring at slack tide. The former induces an asymmetric distortion, similar to that caused by finite amplitude effects and bottom friction. The latter induces a symmetric distortion, which is distinguished from asymmetric by its quadratic nature $u|u|$ and because the sign on the water level deviation $\pm\zeta$ does not enter into the effect.

The forces influencing motion provide a combined linear and nonlinear effect. Linear effects are to decrease the wave propagation speed and to attenuate the wave amplitude. Distortion will not arise from linear effects: high and low waters will both be delayed and each with reduced amplitudes. Nonlinear effects cause distortion by the transfer of spectral energy; that is, decay of the fundamental wave generates higher harmonic waves. The higher harmonics act at frequencies that are multiples of the fundamental frequency. The fourth-diurnal overtide M4 is generated generally by the nonlinear continuity term and locally by advection and depth-dependent bottom friction $\zeta u|u|$ (Aubrey and Speer, 1985). Quadratic bottom friction $u|u|$ is the most dominant effect in generating the sixth-diurnal overtide M6 (Walters and Werner, 1991).

4.3. Previous Tidal Studies in the South Atlantic Bight

Lynch et al. (2004) constructed a data assimilative forecast system for the South Atlantic Bight. Two different domain representations were employed: 1) a mesh that included the tidal inlets and coastal rivers of Georgia; and 2) another that did not include the inlet/river features. The comprehensive mesh consisted of 57,824 nodes and 100,823 elements: the inlets and rivers were resolved at 500 m, and where data inversion took place, the mesh was resolved down to 250 m.

Both models were implemented in a data inversion procedure (Lynch et al., 2004). It was demonstrated that "quality" could be attained for both meshes; "quality" in the sense that the mesh without the inlets and rivers of Georgia permitted for improved local performance, but at the expense of polluting the solution over the continental shelf. For the mesh including the inlet/river features, performance was improved locally while preserving the solution over the continental shelf. Their end conclusion: "inshore resolution is absolutely necessary" in order to faithfully capture the tidal physics.

Blanton et al. (2004) performed a data and numerical model study of the barotropic tides in the South Atlantic Bight and demonstrated improved model skill with the Georgia/South Carolina inlets and rivers resolved. Their unstructured mesh consisted of 63,076 nodes and 111,748 elements, with resolution reducing down to 50 – 100 m at the inlets and rivers. Simulated M2 tidal currents on the shelf were shown to be affected by including the Georgia/South Carolina inlets and rivers in the domain. Observed data corroborated their model results. It was also shown that the inlets and rivers act to dissipate energy in the system.

Lynch et al. (2004) and Blanton et al. (2004) contain the latest in technology towards simulating the tides in the South Atlantic Bight and represent the latest knowledge on tidal

dynamics in the domain. Their domain representations perforated the coastline: the major finding was that the perforated coastline impacts the reflectivity of the boundary. This dissertation intends to expand on previous efforts in two ways: 1) higher resolution of the domain throughout; and 2) overall greater extent of the estuarine features including Florida's east coast, the Atlantic Intracoastal Waterway in its entirety within the region, and all intertidal zones. To advance the general understanding of the system, the hydrodynamics within the South Atlantic Bight estuaries are established as being highly interconnected. This dissertation also examines how this interconnectedness within the estuaries plays a role on tidal dynamics (standing versus progressive) in the South Atlantic Bight.

CHAPTER 5. SURFACE IMAGERY AND LANDCOVER DATA

5.1. Satellite Imagery

Surface imagery is collected for the purpose of using it as a background layer in the model building process. GeoCover Landsat mosaics (circa 2000) are downloaded from the National Aeronautics and Space Administration (website https://zulu.ssc.nasa.gov/mrsid/ accessed on June 15, 2009). The images are based on three Landsat Enhanced Thematic Mapper bands: 1) Band 7 (mid-infrared light) is displayed as red; 2) Band 4 (near-infrared light) is displayed as green; and 3) Band 2 (visible green light) is displayed as blue. Mosaics are collected for Universal Transverse Mercator (UTM) zones 17N and 18N. Longitudinally, each mosaic spans the width of its respective UTM zone. Overall, the latitudinal extent of the mosaics collected is 20°N – 40°N. The satellite imagery is assembled in GIS and geographically covers the South Atlantic Bight (Figure 5.1).

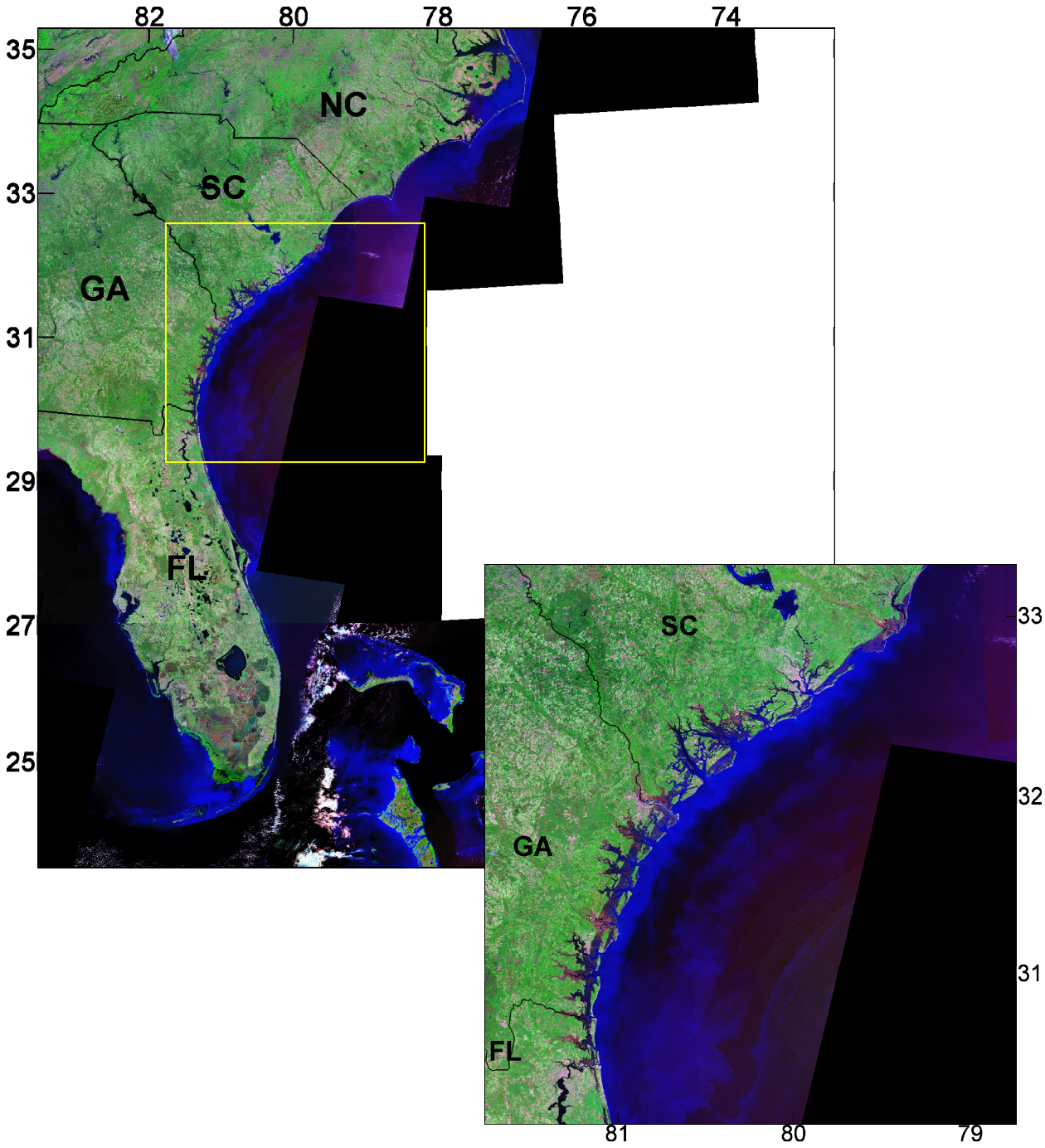

Figure 5.1. Satellite imagery (circa 2000) for the South Atlantic Bight (sourced from the National Aeronautics and Space Administration). The inset follows from the box in the larger view.

5.2. Landcover Data

Landcover data are collected for the purpose of using them as additional layers in the model building process. Two sources supply landcover data in this study: 1) National LandCover Database 2001 (NLCD 2001) raster maps; and 2) GIS products from the St. Johns River and South Florida Water Management Districts. The NLCD 2001 landcover data are based on Landsat imagery, improved with a 30-m digital elevation model (Homer et al., 2004). Raster maps are obtained from the Multi-Resolution Land Characteristics Consortium (website http://www.mrlc.gov/ accessed on June 15, 2009). Superzone 14 is selected, which includes mapping zones 54 through 59. This geographically covers the South Atlantic Bight (Figure 5.2).

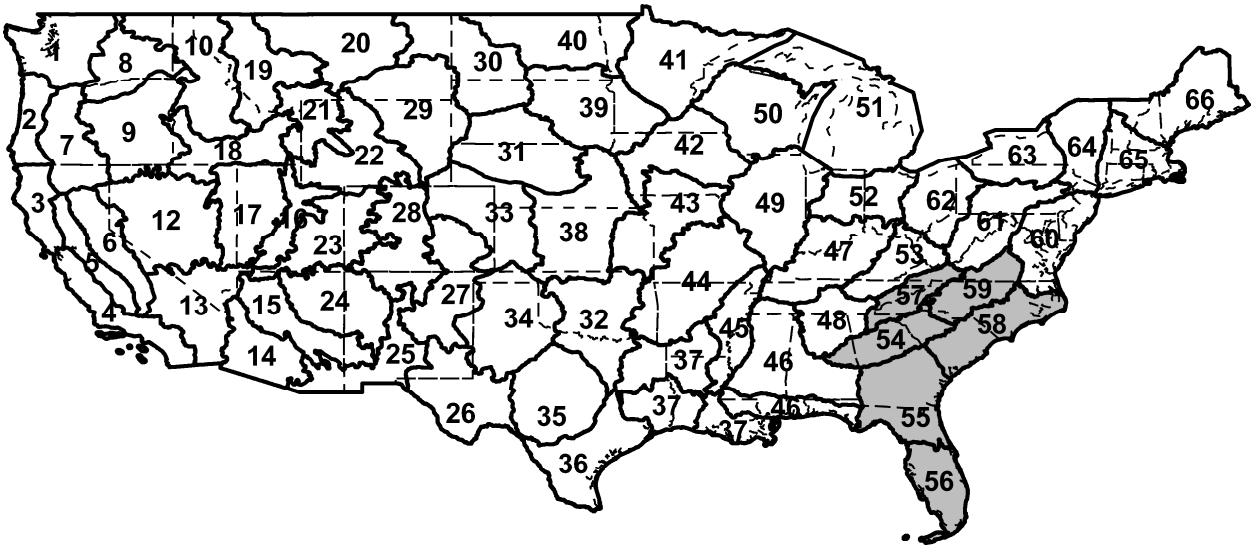

Figure 5.2. Contiguous mapping zones used by the National LandCover Database 2001 (after Homer et al. [2004]) displayed over state boundaries (dashed lines). Mapping zones 54 through 59 (shaded in grey) correspond to the landcover data obtained for this study.

Homer et al. (2004) use a decision tree methodology to classify the land according its characteristics. Listed in Table 5.1 are the descriptions of 19 different landcover classifications used by NLCD 2001. Classes 11, 90, and 95 will be employed in this study: "open water" will be used be used to identify fully wetted regions; and "woody wetlands" and "emergent herbaceous wetlands" will be used to identify intertidal zones. The two intertidal classes (90 and 95) are differentiated primarily by the type of vegetation they promote: "woody wetlands" contain rigid forms of vegetation (e.g., trees) whereas "emergent herbaceous wetlands" contain flexible forms of vegetation (e.g., reeds). Figure 5.3 displays the NLCD 2001 landcover data relative to the South Atlantic Bight. In the inset, the cities of Jacksonville, Florida; Savannah, Georgia; and Charleston, South Carolina are visible in shades of red ("developed"). Wide bands of intertidal zones spanning between the developed coastal areas are visible in lighter shades of blue ("wetlands").

Additional landcover data are obtained from the St. Johns River and South Florida Water Management Districts and geographically cover the east coast of Florida (Figure 5.4). These data were developed using 2004 natural color and infrared aerial photography. This source imagery was combined with field reconnaissance to delineate different regions of common landcover attributes. The classification system used is the Florida Land Use, Cover and Forms Classification System (FLUCCS), which was originally compiled by the Florida Department of Transportation (1985).

Table 5.1. Descriptions of 19 different landcover classifications used by the National LandCover Database 2001 (after Homer et al. [2004]). Classes shaded in grey are exposed to the tides on a constant or regular basis.

Val	Class: Description
11.	**Open Water:** All areas of open water, generally with less than 25% cover of vegetation or soil.
12.	**Perennial Ice/Snow:** All areas characterized by a perennial cover of ice and/or snow, generally greater than 25% of total cover.
21.	**Developed, Open Space:** Includes areas with a mixture of some constructed materials, but mostly vegetation in the form of lawn grasses. Impervious surface account for less than 20% of total cover. These areas most commonly include large-lot single-family housing units, parks, golf courses, and vegetation planted in developed settings for recreation, erosion control, or aesthetic purposes.
22.	**Developed, Low Intensity:** Includes areas with a mixture of constructed materials and vegetation. Impervious surfaces account for 20–49% of total cover. These areas most commonly include single-family housing units.
23.	**Developed, Medium Intensity:** Includes areas with a mixture of constructed materials and vegetation. Impervious surface account for 50–79% of the total cover. These areas most commonly include single-family housing units.
24.	**Developed, High Intensity:** Includes highly developed areas where people reside or work in high numbers. Examples include apartment complexes, row houses, and commercial/industrial. Impervious surfaces account for 80–100% of the total cover.
31.	**Barren Land (Rock/Sand/Clay):** Barren areas of bedrock, desert pavement, scarps, talus, slides, volcanic material, glacial debris, sand dunes, strip mines, gravel pits, and other accumulations of earthen material. Generally, vegetation accounts for less than 15% of total cover.
41.	**Deciduous Forest:** Areas dominated by trees generally greater than 5 meters tall, and greater than 20% of total vegetation cover. More than 75% of the tree species shed foliage simultaneously in response to seasonal changes.
42.	**Evergreen Forest:** Areas dominated by trees generally greater than 5 meters, and greater than 20% of total vegetation cover. More than 75% of the three species maintain their leaves all year. Canopy is never without green foliage.
43.	**Mixed Forest:** Areas dominated by trees generally greater than 5 meters tall, and greater than 20% of total vegetation cover. Neither deciduous nor evergreen species are greater than 75% of total tree cover.
51.	**Dwarf Scrub:** Alaska only areas dominated by shrubs less than 29 centimeters tall with shrub canopy typically greater than 20% of total vegetation. This type is often co-associated with grasses, sedges, herbs, and non-vascular vegetation.
52.	**Shrub/Scrub:** Areas dominated by shrubs: less than 5 meters tall with shrub canopy typically greater than 20% of total vegetation. This class includes true shrubs, young trees in an early successional stage, or trees stunted from environmental conditions.
71.	**Grassland/Herbaceous:** Areas dominated by grammanoid or herbaceous vegetation, generally greater than 80% of total vegetation. These areas are not subject to intensive management such as tilling, but can be utilized for grazing.
72.	**Sedge/Herbaceous:** Alaska only areas dominated by sedges and forbs, generally greater than 80% of total vegetation. This type can occur with grasses or other grass like plants, and includes sedge tundra, and sedge tussock tundra.
74.	**Moss:** Alaska only areas dominated by mosses, generally greater than 80% of total vegetation.

Val	Class: Description
81.	**Pasture/Hay:** Areas of grasses, legumes, or grass-legume mixtures planted for livestock grazing or the production of seed or hay crops, typically on a perennial cycle. Pasture/hay vegetation accounts for greater than 20% of total vegetation.
82.	**Cultivated Crops:** Areas used for the production of annual crops, such as corn, soybeans, vegetables, tobacco, and cotton, and also perennial woody crops such as orchards and vineyards. Crop vegetation accounts for greater than 20% of total vegetation. This class also includes all land being actively tilled.
90.	**Woody Wetlands:** Areas where forest or shrubland vegetation accounts for greater than 20% of vegetative cover and the soil or substrate is periodically saturated with or covered with water.
95.	**Emergent Herbaceous Wetlands:** Areas where perennial herbaceous vegetation accounts for greater than 80% of vegetative cover and the soil or substrate is periodically saturated with or covered with water.

Each FLUCCS code consists of 4 digits and the system is hierarchal in structure (Table 5.2). Of the 1000 through 9000 series, the 5000, 6000, and 9000 series are applicable to regions with exposure to the tides. The 5000 series represents "water," which is delineated as open areas and for channels that are wider than 30 m, and has three categories related to the coastal and estuarine environment: 1) "streams and waterways" (5100) classifies streams and waterways, both natural and channelized; 2) "bays and estuaries" (5400) classifies open and closed embayments; and 3) "ocean and gulf" (5700) classifies open waters. Some examples include: the St. Johns River as a "stream and waterway," the Indian River lagoon as a "bay and estuary," and the Atlantic Ocean as an "ocean and gulf."

The 6000 series represents "wetlands," which includes various freshwater types and two saltwater types: 1) "saltwater marshes" (6420); and 2) "mangrove swamps" (6120). The hydrology for both types is described as being directly influenced by tidal fluctuations (Florida Department of Transportation, 1985). "Saltwater marshes" are extensive in regions of low relief and high tidal range (northeastern Florida) whereas "mangrove swamps" fringe the coastal waterbodies of southeastern Florida.

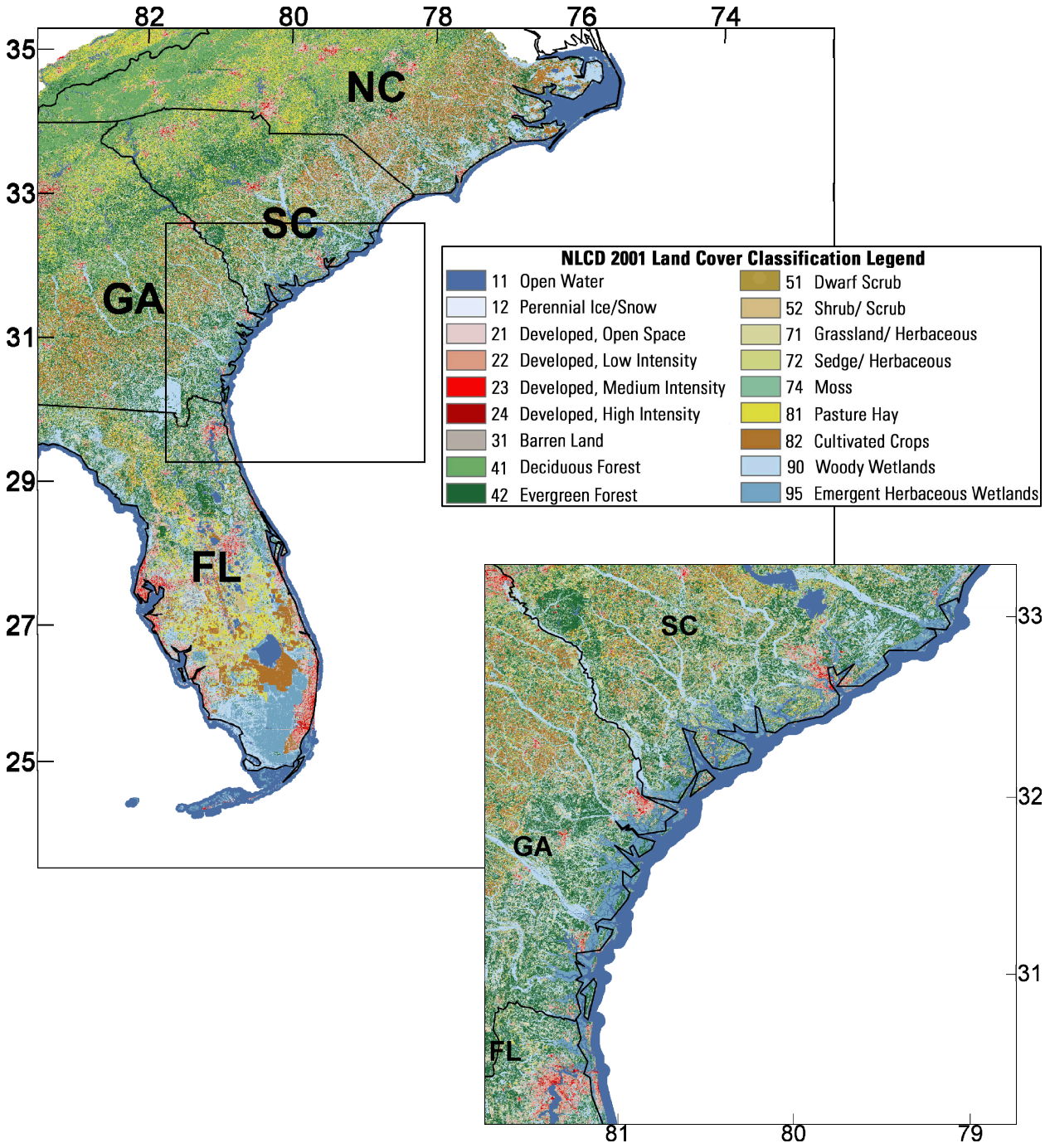

Figure 5.3. National LandCover Database 2001 raster map for the South Atlantic Bight displayed according to the classification legend. The inset follows from the box in the larger view.

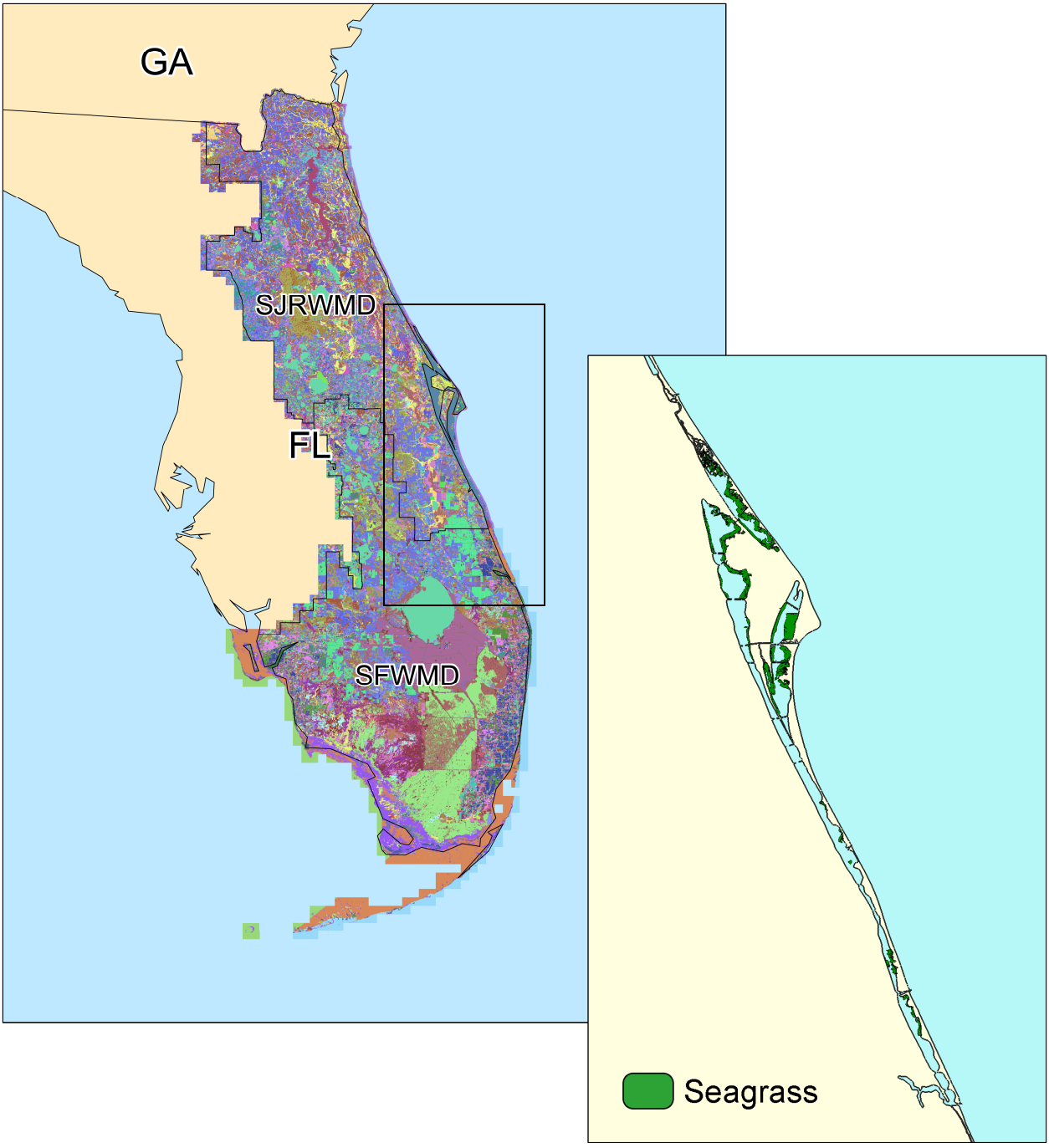

Figure 5.4. Landcover data obtained from St. Johns River and South Florida Water Management Districts geographically cover the east coast of Florida. The inset follows from the box in the larger view and shows the distribution of "seagrass beds" (class 9110) in the Indian River lagoon.

Table 5.2. Partial listing of FLUCCS (Florida Land Use, Cover and Forms Classification System) codes (after Florida Department of Transportation [1985]).

1000	**Urban and built-up**
2000	**Agricultural**
3000	**Upland non-forested**
4000	**Upland forested**
5000	**Water**
	5100 Streams and waterways
	5400 Bays and estuaries
	5700 Gulf and ocean
6000	**Wetlands**
	6100 Wetland hardwood forest
	6110 Bay swamps
	6120 Mangrove swamps
	6170 Mixed wetland hardwoods
	6400 Vegetated non-forested wetlands
	6420 Saltwater marshes
	6500 Non-vegetated wetlands
	6510 Tidal flats
7000	**Barren land**
8000	**Transportation, communication, and utilities**
9000	**Aquatic vegetation**
	9100 Seagrass and algae beds
	9110 Seagrass
	9120 Algae

"Saltwater marshes" are described as communities of non-woody, salt-tolerant plants occupying intertidal zones that are at least occasionally inundated with saltwater (Figure 5.5). The vegetation is generally short and flexible with coverage of the landscape being widespread and consisting of dense patches. Classes similar to "saltwater marshes" include 6500 ("non-vegetated wetlands") and 6510 ("tidal flats").

Figure 5.5. "Saltwater marshes" are described as communities of non-woody, salt-tolerant plants occupying intertidal zones that are at least occasionally inundated with saltwater (photo courtesy of the South Florida Water Management District).

"Mangrove swamps" are described as communities of mangrove species that are subject to periodic or continual inundation by saltwater or brackish water (Figure 5.6). The vegetation generally consists of a thicket of woody roots around the water line with landscape coverage limited to the fringes of coastal waterbodies. Classes similar to "mangrove swamps" include 6110 ("bay swamps") and 6170 ("mixed wetland hardwoods").

Figure 5.6. "Mangrove swamps" are described as communities of mangrove species that are subject to periodic or continual inundation by saltwater or brackish water (photo courtesy of the South Florida Water Management District).

The 9000 series represents “aquatic vegetation,” which includes the following benthic plant species: 1) “seagrass beds” (class 9110); and 2) “algae beds” (class 9120). These classes identify areas that include greater than 50% vegetative cover (Florida Department of Transportation, 1985). Seagrasses are vascular flowering plants; not algae. The inset of Figure 5.4 shows the distribution of “seagrass beds” (class 9110) in the Indian River lagoon, which is broad in its coverage: 200 km^2.

CHAPTER 6. BATHYMETRIC DATA

The bathymetric data used in this study are presented here in order of precedence. Generally, high-resolution bathymetric data are used for the estuarine and shelf waters whereas medium-resolution data are used for the deep ocean. The end of this chapter discusses datum issues and the merging of the different bathymetric datasets into a single digital elevation model.

6.1. Estuarine Waters

Bathymetric depths for the Lower St. Johns River, Northern Coastal Basin, Indian River lagoon, and most other estuaries in central and northeastern Florida are supplied by the St. Johns River Water Management District (Figure 6.1, red). The data consist mainly of transects along the Lower St. Johns River with sounding tracks elsewhere. The transects are spaced 1 km apart in the longitudinal (river) axis and points on the transects are spaced on the order of meters to tens of meters. Resolution of the sounding data is on the order of tens to hundreds of meters. In all, there are over 2 million data points, which results in coverage for nearly all of Florida's east coast. Where coverage lacks, bathymetric data from previous studies are used. Lake George, located 170 km upstream in the Lower St. Johns River (Figure 6.1, middle arrow), is accounted for using bathymetric depths from the model of Bacopoulos et al. (2009). Lake Worth lagoon and the Loxahatchee and St. Lucie Rivers (Figure 6.1, bottom arrow) are accounted for using bathymetric depths from the model of Bacopoulos and Hagen (2009).

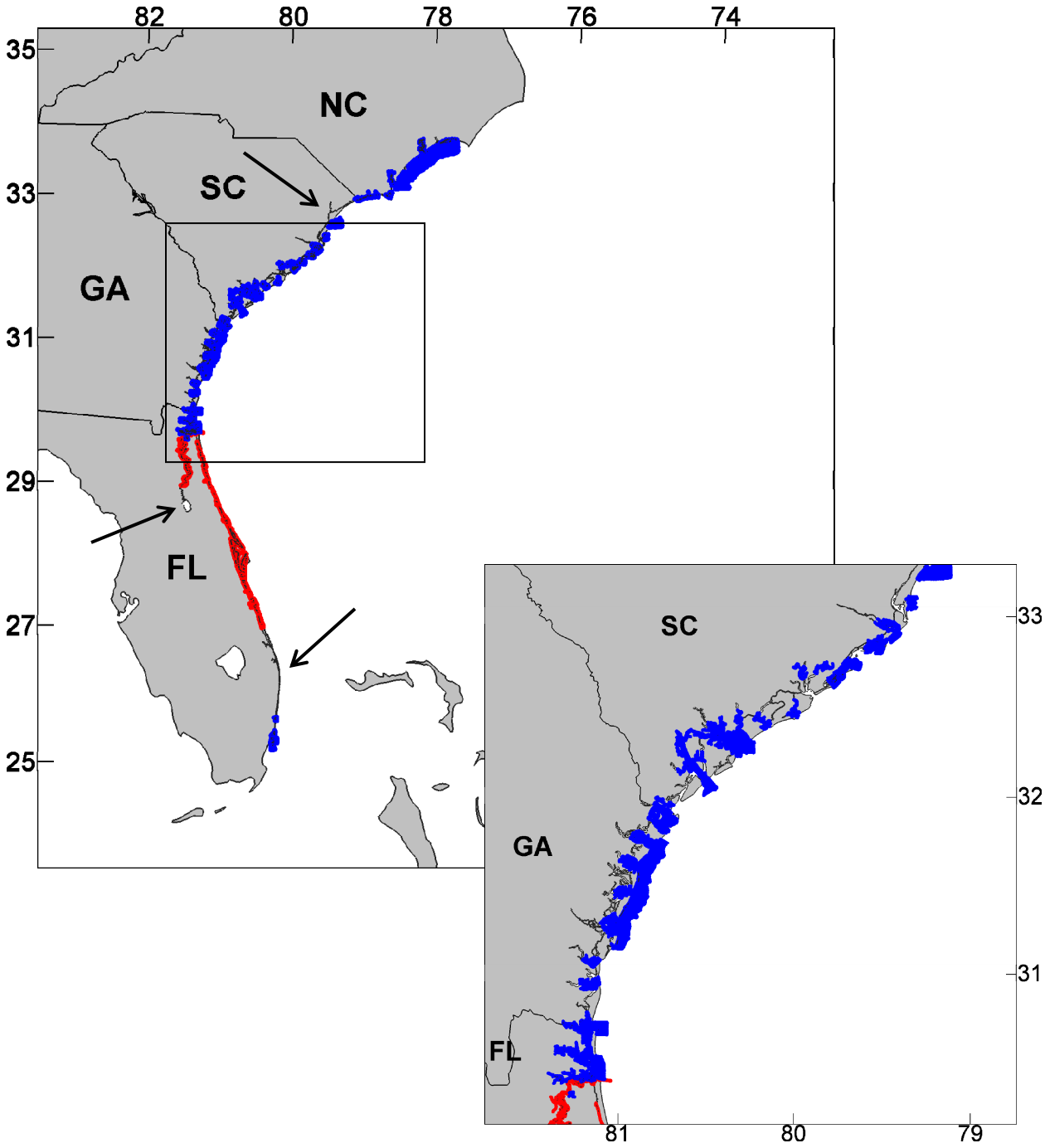

Figure 6.1. Bathymetric data for the South Atlantic Bight estuaries: (red) St. Johns River Water Management District; and (blue) National Ocean Service. The three arrows point to areas where data from previous studies are used (see related text). The inset follows from the box in the larger view.

Bathymetric depths for the estuaries in the Carolinas, Georgia, and extreme northeastern and southeastern Florida are supplied by National Ocean Service hydrographic surveys (obtained from the Office of Coast Survey and National Geophysical Data Center: website http://map.ngdc.noaa.gov/website/mgg/nos_hydro/viewer.htm accessed on March 15, 2008) (Figure 6.1, blue). Resolution of the survey data is on the order of tens to hundreds of meters, which allows for the capture of rivers and tidal creeks. In all, there are over 750,000 data points. Bathymetric depths for the Winyah Bay and Waccamaw River system (Figure 6.1, top arrow) result from the model of Dietsche et al. (2007).

6.2. Shelf and Ocean Waters

The Coastal Relief Model provides bathymetric data for the United States (accessible via DVD-ROM available from the National Geophysical Data Center). The Coastal Relief Model extends from the coastal state boundaries to beyond the shelf break. Elevation grids are downloaded at 3-arc-second (~30 m) resolution for the shelf waters of the South Atlantic Bight (Figure 6.2, red). In all, there are over 15 million data points. Bathymetric depths in the deep ocean and all other waters are based on the Western North Atlantic Tidal model domain (Hagen et al., 2006) (Figure 6.2, blue).

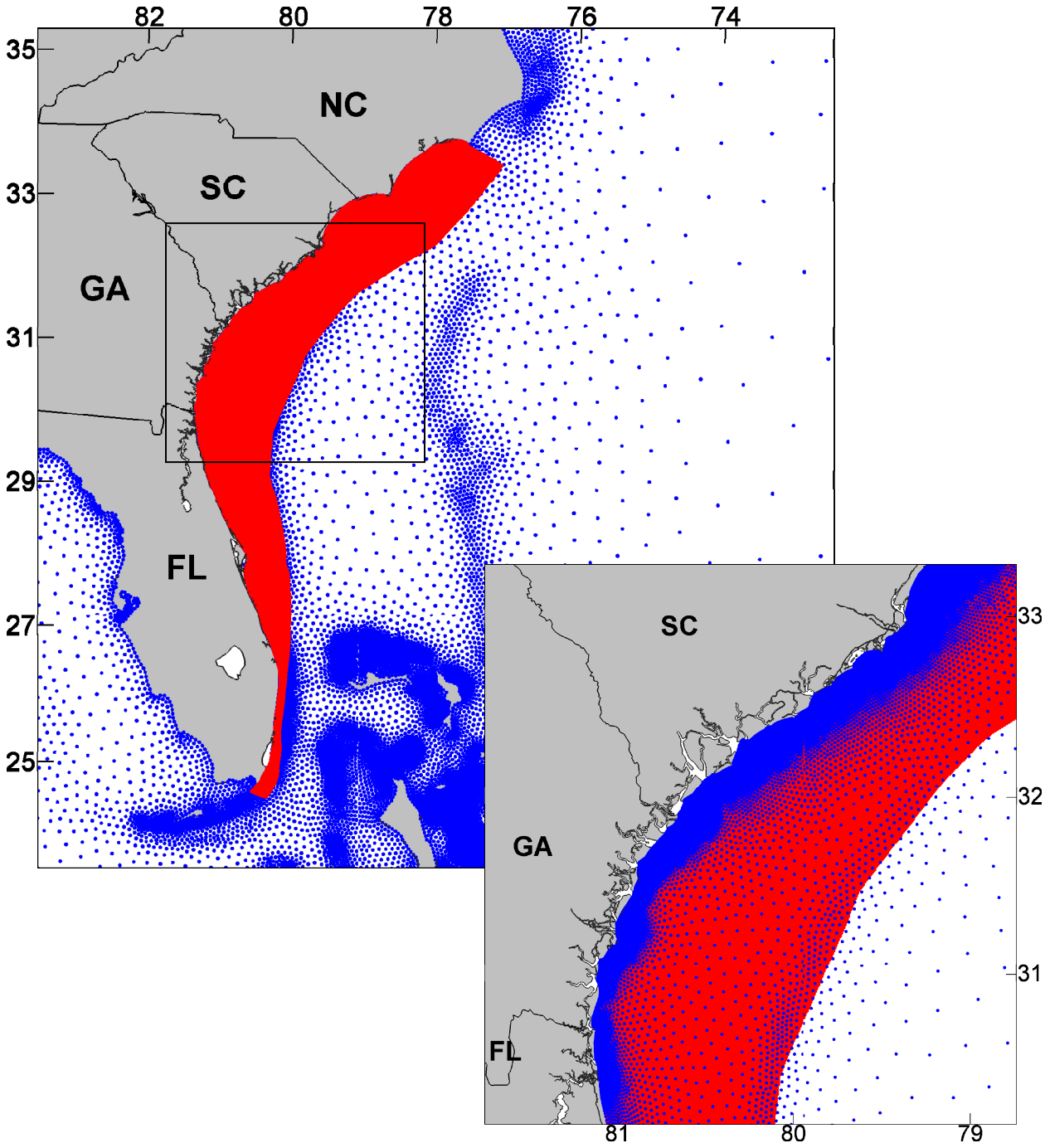

Figure 6.2. Bathymetric data for the shelf and ocean waters of the South Atlantic Bight: (red) Coastal Relief Model; and (blue) Western North Atlantic Tidal model domain. The Coastal Relief Model takes priority for areas that overlap. The inset follows from the box in the larger view.

6.3. Quality Assurance/Quality Control

The quality assurance/quality control procedure described herein has two parts: 1) reference each bathymetric dataset to the National American Vertical Datum of 1988 (NAVD88); and 2) merge the different bathymetric datasets into a single digital elevation model. NAVD88 is a terrain-based vertical datum that varies minimally over a large horizontal space. On the other hand, oceanographic datums can vary greatly over horizontal space. The implication is that the offset between NAVD88 and an oceanographic datum is spatially variant. Therefore, in order to transform from an oceanographic datum to NAVD88, it is necessary to apply an adjustment that varies spatially.

Data supplied by the St. Johns River Water Management District and from the Western North Atlantic Tidal model domain are already in NAVD88 and therefore require no adjustment. The National Ocean Service hydrographic surveys are referenced to mean low water (MLW) and thus undergo adjustment, as is also the case with the Coastal Relief Model gridded bathymetric data, which are referenced to mean sea level (MSL). The Center for Operational Oceanographic Products and Services (website http://tidesandcurrents.noaa.gov/ accessed on March 15, 2008) provides tidal benchmark information for over one thousand ocean and coastal sites: its geographic location is known along with established levels of terrain-based and oceanographic datums. Datum elevations are downloaded for a total of 1,502 tidal benchmark stations. Pre-processing removes any tidal benchmark station located outside of a roughly 100-km perimeter of the South Atlantic Bight, which reduces the overall dataset to 345 tidal benchmark stations.

For processing the National Ocean Service hydrographic surveys, any tidal benchmark station without measures for both MLW and NAVD88 is discarded. For the Coastal Relief

Model gridded bathymetric data, tidal benchmark stations without measures for both MSL and NAVD88 are discarded. This is done since such cases do not allow for the associated offset to be calculated. Afterward, the offsets at the tidal benchmark stations are assessed for anomalies. With the respect to processing the National Ocean Service hydrographic surveys, six tidal benchmark stations with abnormally large (or small) offset values (relative to their neighbors) are discarded from the overall dataset (Table 6.1). With the Coastal Relief Model gridded bathymetric data, six tidal benchmark stations are found to be anomalous (Table 6.2). In the end, a total of 243 and 249 tidal benchmark stations are used for processing the National Ocean Service hydrographic surveys (Figure 6.3) and Coastal Relief Model gridded bathymetric data (Figure 6.4), respectively.

With the tidal benchmark information properly compiled, a routine is devised in order to automate the datum adjustment procedure. Each bathymetric dataset (National Ocean Service hydrographic surveys and Coastal Relief Model gridded bathymetric data) undergoes this routine, which is two-step: 1) for each point of the bathymetric dataset, identify the three nearest tidal benchmark stations; and 2) compute the local offset using a reciprocal-distance-squared average of the offset values corresponding to the three nearest tidal benchmark stations. All points in the bathymetric dataset are adjusted in this manner.

The second step of the quality assurance/quality control procedure is to merge the different bathymetric datasets into a single digital elevation model (Figure 6.5). In areas of overlap, data are kept under the following priority: 1) St. Johns River Water Management District; 2) National Ocean Service; 3) Coastal Relief Model; and 4) Western North Atlantic Tidal model domain. Checks are performed to ensure smooth transitions occur where different datasets meet. Resolution is generally on the order of tens to hundreds of meters.

Table 6.1. Six tidal benchmark stations with abnormally large (or small) offset values relative to their neighbors are eliminated from the final dataset corresponding to the National Ocean Service hydrographic surveys.

°W	°N	Station[a]	Reason to eliminate[b]
–79.151667	33.608333	8661299	$\Delta = -0.5$ while local surrounding is at $\Delta = 0.0$
–81.121667	32.303333	8668701	$\Delta = -0.5$ while local surrounding is at $\Delta = 0.5$
–81.300000	29.916667	8720554	$\Delta = 2.5$ while local surrounding is at $\Delta = 1.0$
–81.681667	29.595000	8720767	$\Delta = 1.0$ while local surrounding is at $\Delta = 0.25$
–81.631667	29.643333	8720774	$\Delta = 1.75$ while local surrounding is at $\Delta = 0.25$
–81.675000	29.476667	8720832	$\Delta = 1.0$ while local surrounding is at $\Delta = 0.25$

[a] The National Ocean Service identifies each tidal benchmark station with a unique number.

[b] Offset values shown here in units of meters.

Table 6.2. Six tidal benchmark stations with abnormally large (or small) offset values relative to their neighbors are eliminated from the final dataset corresponding to the Coastal Relief Model gridded bathymetric data.

°W	°N	Station[a]	Reason to eliminate[b]
–79.151667	33.608333	8661299	$\Delta = -0.75$ while local surrounding is at $\Delta = 0.0$
–79.706667	32.856667	8664941	$\Delta = -0.5$ while local surrounding is at $\Delta = 0.0$
–81.121667	32.303333	8668701	$\Delta = -1.0$ while local surrounding is at $\Delta = 0.0$
–81.453333	30.416667	8720196	$\Delta = -0.25$ while local surrounding is at $\Delta = 0.25$
–81.300000	29.916667	8720554	$\Delta = 1.75$ while local surrounding is at $\Delta = 0.25$
–81.631667	29.643333	8720774	$\Delta = 1.5$ while local surrounding is at $\Delta = 0.5$

[a] The National Ocean Service identifies each tidal benchmark station with a unique number.

[b] Offset values shown here in units of meters.

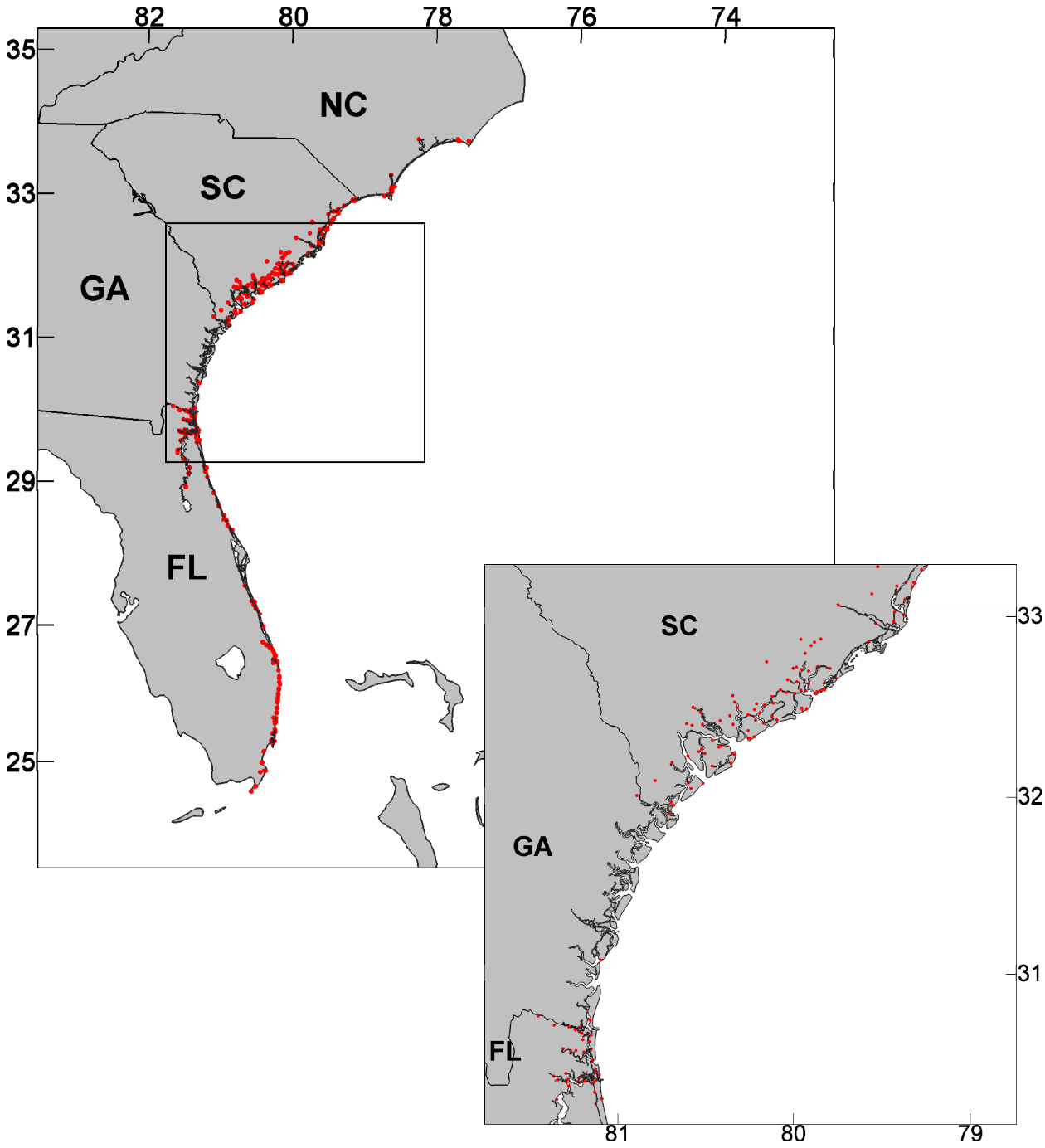

Figure 6.3. A total of 243 tidal benchmark stations are used for processing the National Ocean Service hydrographic surveys.

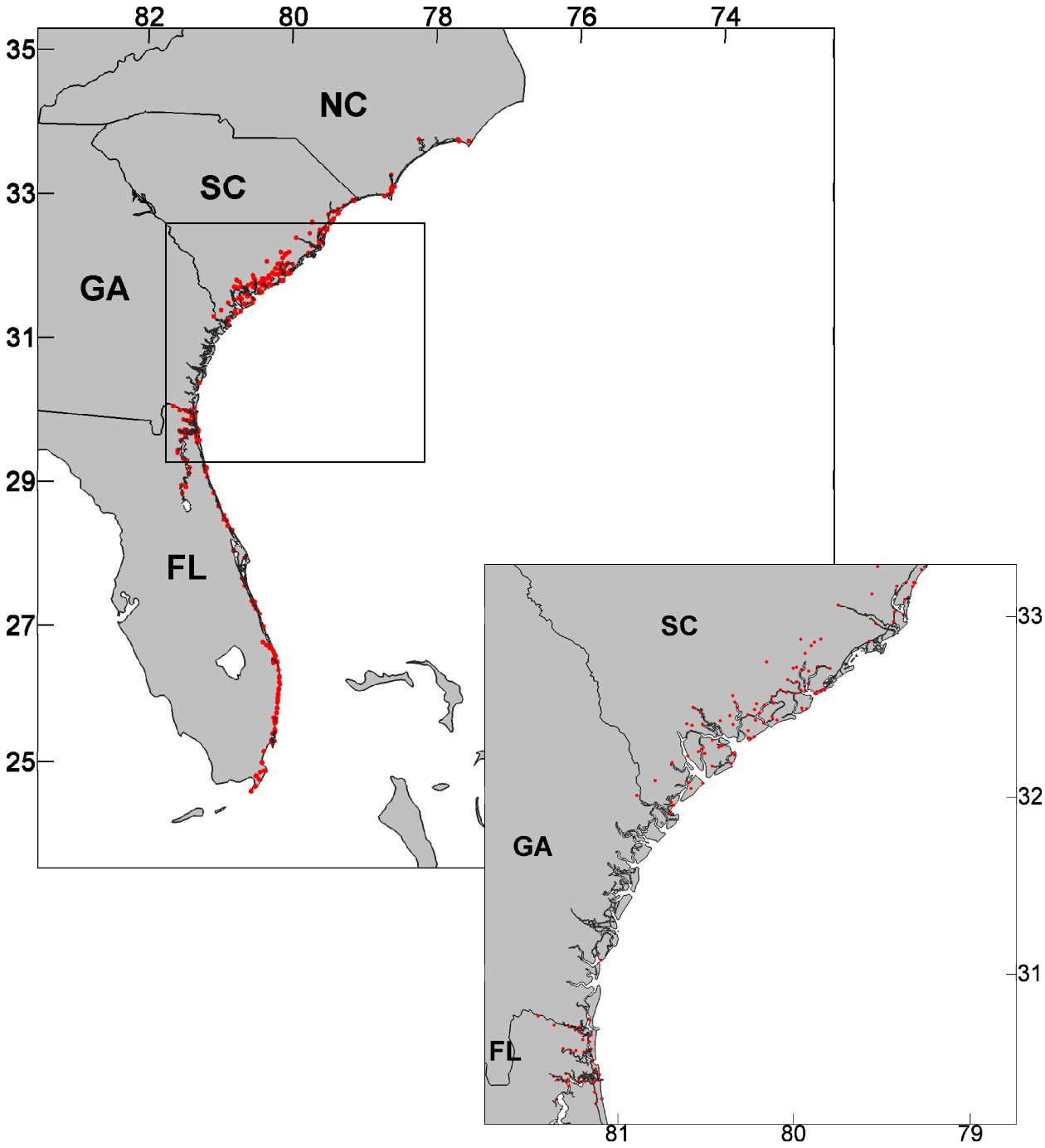

Figure 6.4. A total of 249 tidal benchmark stations are used for processing the Coastal Relief Model gridded bathymetric data.

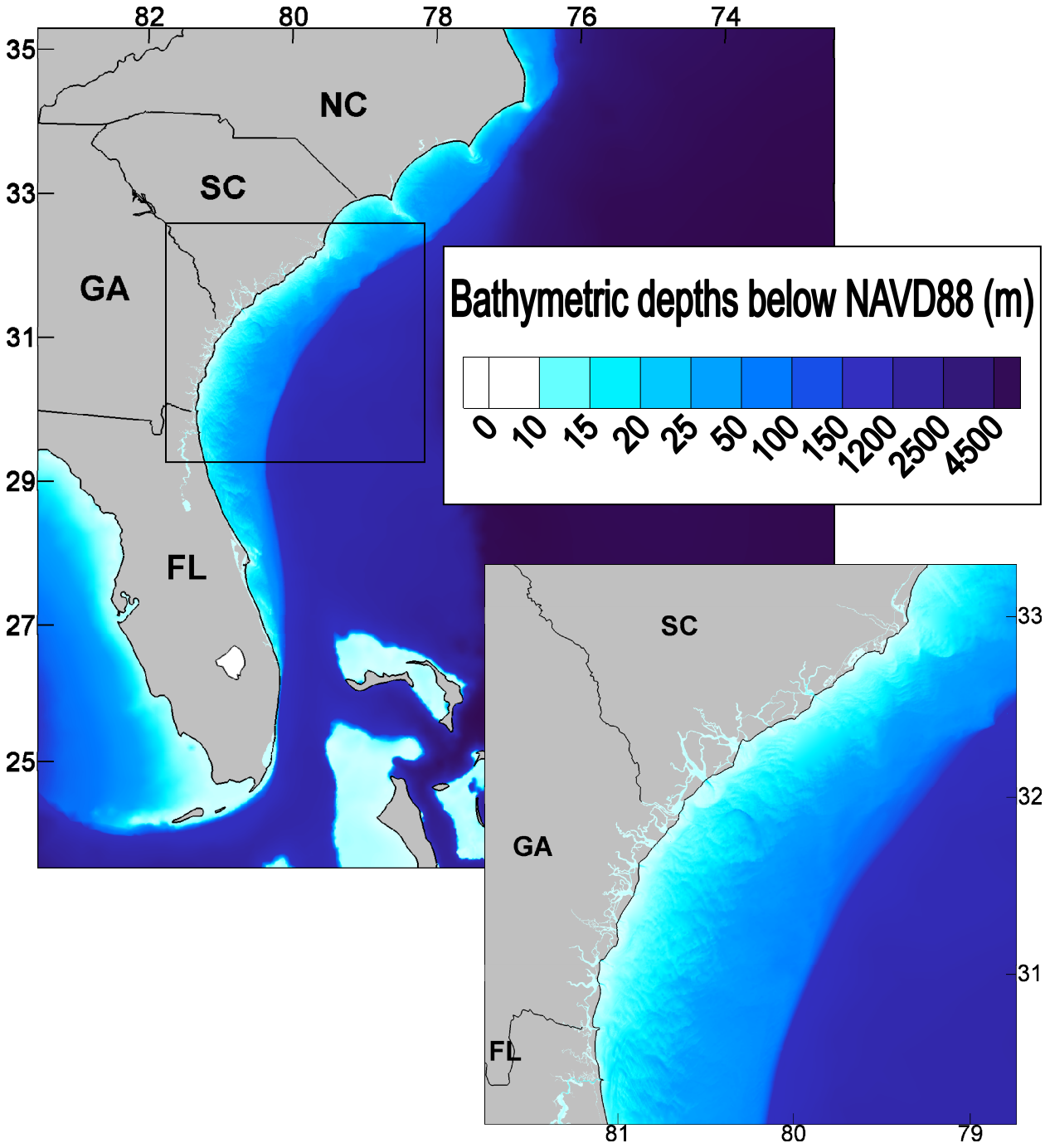

Figure 6.5. Bathymetry of the domain as represented in the digital elevation model. For neatness of the graphic, data outside the waterbody delineation (defined in the subsequent chapter) are clipped. The coastline and state boundaries are shown for reference. The inset follows from the box in the larger view.

CHAPTER 7. FINITE ELEMENT MESH DEVELOPMENT

The finite element meshes employed in this study are presented here in order of decreasing complexity. The first section describes the development of the comprehensive mesh, which includes all estuarine features of the South Atlantic Bight. The second section presents variants of the comprehensive mesh, which have select estuarine features removed from the domain.

7.1. Comprehensive Estuarine Representation

Recognize that scales vary greatly over the domain: the geometry in shallow water changes sharply over short distances whereas the geometry in deep water changes smoothly over long distances. This is also known *a priori* with regard to the tidal processes occurring in the domain: sharp changes in the shallows relative to smooth changes in the deep. Therefore, an unstructured meshing strategy is employed. This allows for the space to be discretized using variably sized elements: the general approach is to place more elements in the shallows where sharper changes occur over shorter distances.

All unstructured meshing is performed using the Surface Water Modeling System (Zundel, 2006). The first step in constructing the mesh is to digitize the boundaries. This involves two sub-steps done in the following chronologic order: 1) define the open boundary, the coastline and other mainland boundaries, islands, river banks, tidal creeks, and other waterway channels; and 2) define the inland extent of the intertidal zones. The open boundary is defined as an arc sweeping from Cape Lookout, North Carolina to the Florida Keys. This places the

boundary a far distance from the South Atlantic Bight estuaries: generally 750 km. The nearest the boundary comes to the estuaries is 250 km.

All waterbody definition results from the digitization of features interpreted from satellite imagery (Figure 5.1). This allows for accurate representation of the fully wetted system (Figure 7.1). Although, difficult to view in the graphic, a total of 64 inlets (Table 3.2) are described. The first inset highlights the river extent and complexity along the coasts of northeastern Florida, Georgia, and South Carolina. The arrow of the larger view points to the lower 175 km of the St. Johns River including Lake George. The second inset highlights the tidal creeks of the Lower St. Johns River. The insets also give an appreciable display of the Atlantic Intracoastal Waterway, viewable here as the inland channels running between the estuary waterbodies.

Definition of the intertidal zones results from the digitization of inland extent interpreted from NLCD 2001 raster maps (Figure 5.3). The two intertidal classes, 90 and 95 (Table 5.1), are used to delineate areas of "woody wetlands" and "emergent herbaceous wetlands," respectively. The inland extent of the intertidal zones defined by these two classes is shown in Figure 7.1.

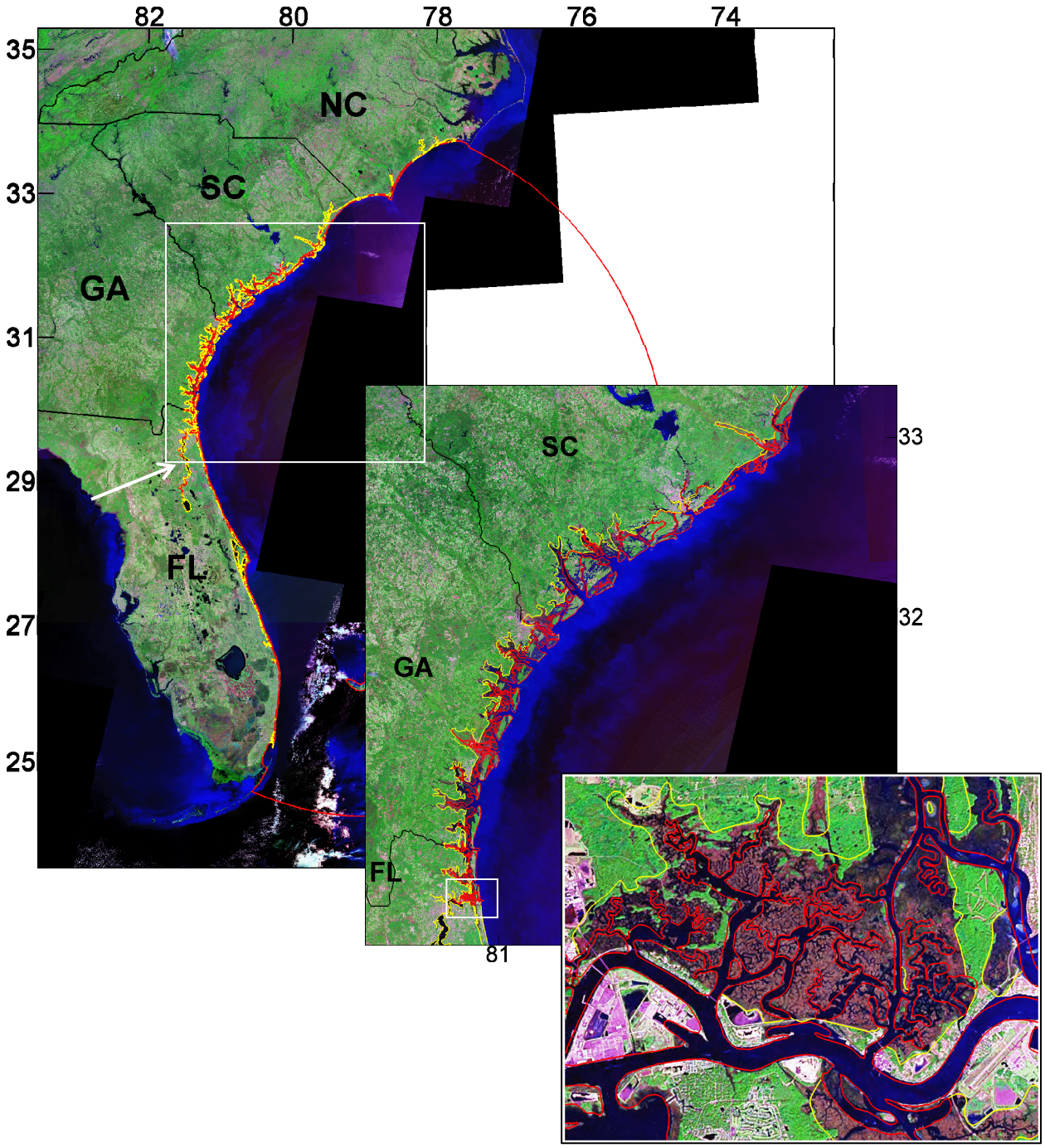

Figure 7.1. Outline of the estuary waterbodies (red) and intertidal zones (yellow) for the South Atlantic Bight. The background is satellite imagery (sourced from the National Aeronautics and Space Administration). The insets follow from the boxes in the larger views.

The interior is triangulated using a two-step manner similar to the boundary definition: 1) waterbodies; and 2) intertidal zones. Triangulation of the waterbodies follows these criteria: 1) no less than three elements (four nodes) span across any channel; and 2) the wavelength-to-element size ratio. The first requirement permits for proper representation of all channels including tidal creeks. For the second requirement, the ratio is based on the M8 tidal constituent (the eighth-diurnal overtide of the M2 tide):

$$\frac{\lambda_{\mathrm{M8}}}{\Delta x} = \frac{\sqrt{gh}}{\Delta x} T_{\mathrm{M8}} \quad \ldots\ldots\ldots\

that the mesh can capably account for the waveforms of the shorter wavelength nonlinear byproducts (e.g., the M8 overtide) wherever they may arise in the domain.

The digital elevation model is then interpolated to the mesh nodes using a linear interpolation scheme (Zundel, 2006). The mesh representation of the digital elevation model is shown in Figure 7.3. The mesh generally captures the features of the digital elevation model (Figure 6.5). The shelf and slope are accurately described, albeit there is slight smoothing on the shelf. The channelized inlet entrances are also represented. The cross-sectional representations of four tidal inlets (Ponce de Leon, Sebastian, Fort Pierce, and St. Lucie Inlets) and two inland channels (Haulover Canal and Dragons Point) in central Florida are quantified in Appendix C.

Triangulation of the intertidal zones extends from the waterbody boundary to the inland extent of the intertidal zones (Figure 7.4). Many islands are meshed over in the process as well. Mesh resolution of the intertidal zones is generally on the order of the resolution of the waterbody boundary: tens of meters. The intertidal zones occupy an appreciable surface area in the mesh: $3.6\times10^{3}\ \mathrm{km}^{2}$ compared to $4.3\times10^{3}\ \mathrm{km}^{2}$ for the waterbodies. This comprehensive mesh has 497,847 nodes and 927,165 elements. Bathymetric depths in the intertidal zones are assumed to be 1 foot (approximately 0.3 m) below NAVD88 (Figure 7.5). The exceptions to this are the intertidal zones of the Lower St. Johns River, which are described using data obtained from the United States Army Corps of Engineers.

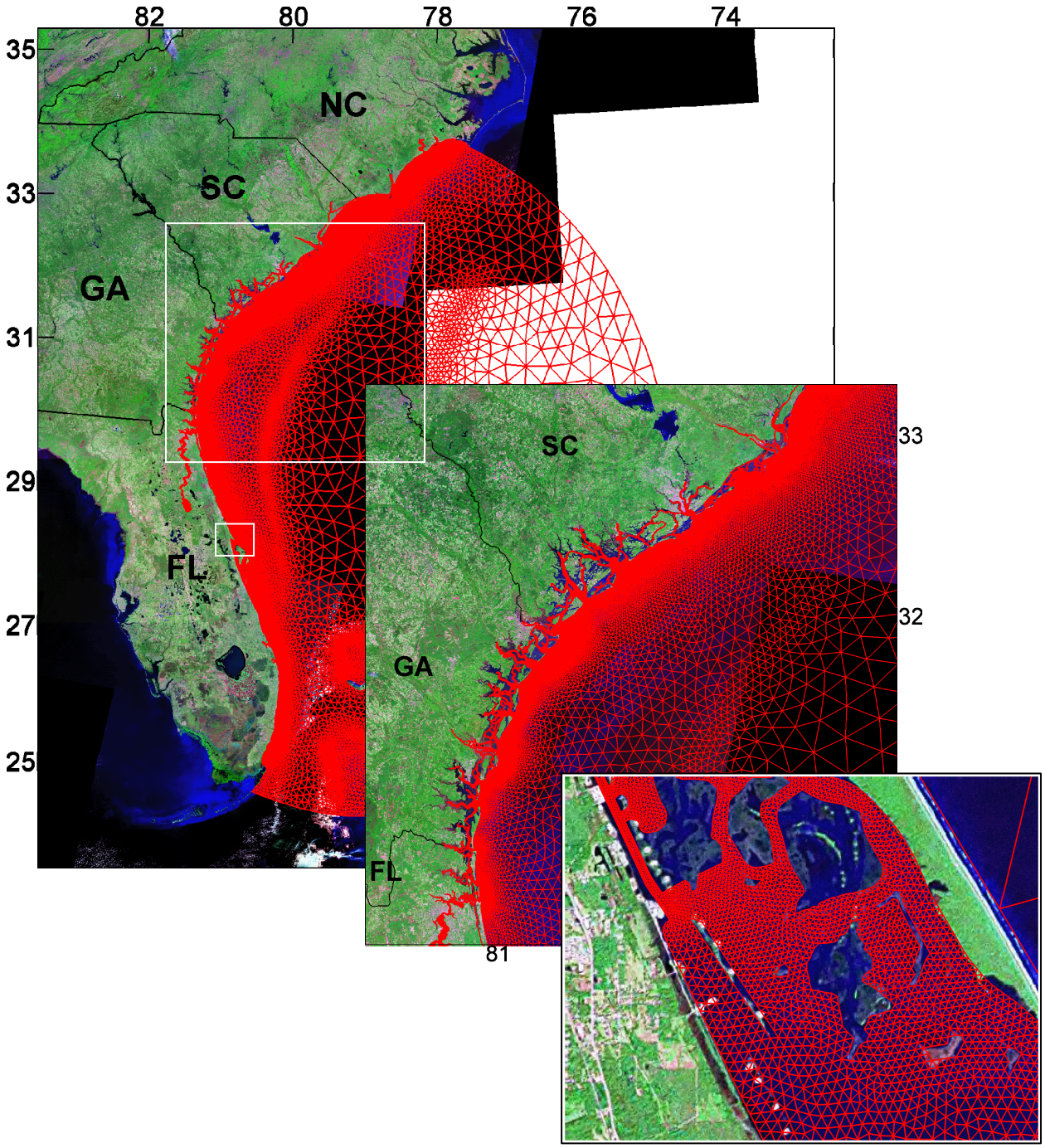

Figure 7.2. Triangulation of the estuary waterbodies for the South Atlantic Bight (a.k.a. the AICWW mesh). The background is satellite imagery (sourced from the National Aeronautics and Space Administration). The insets follow from the boxes in the larger views.

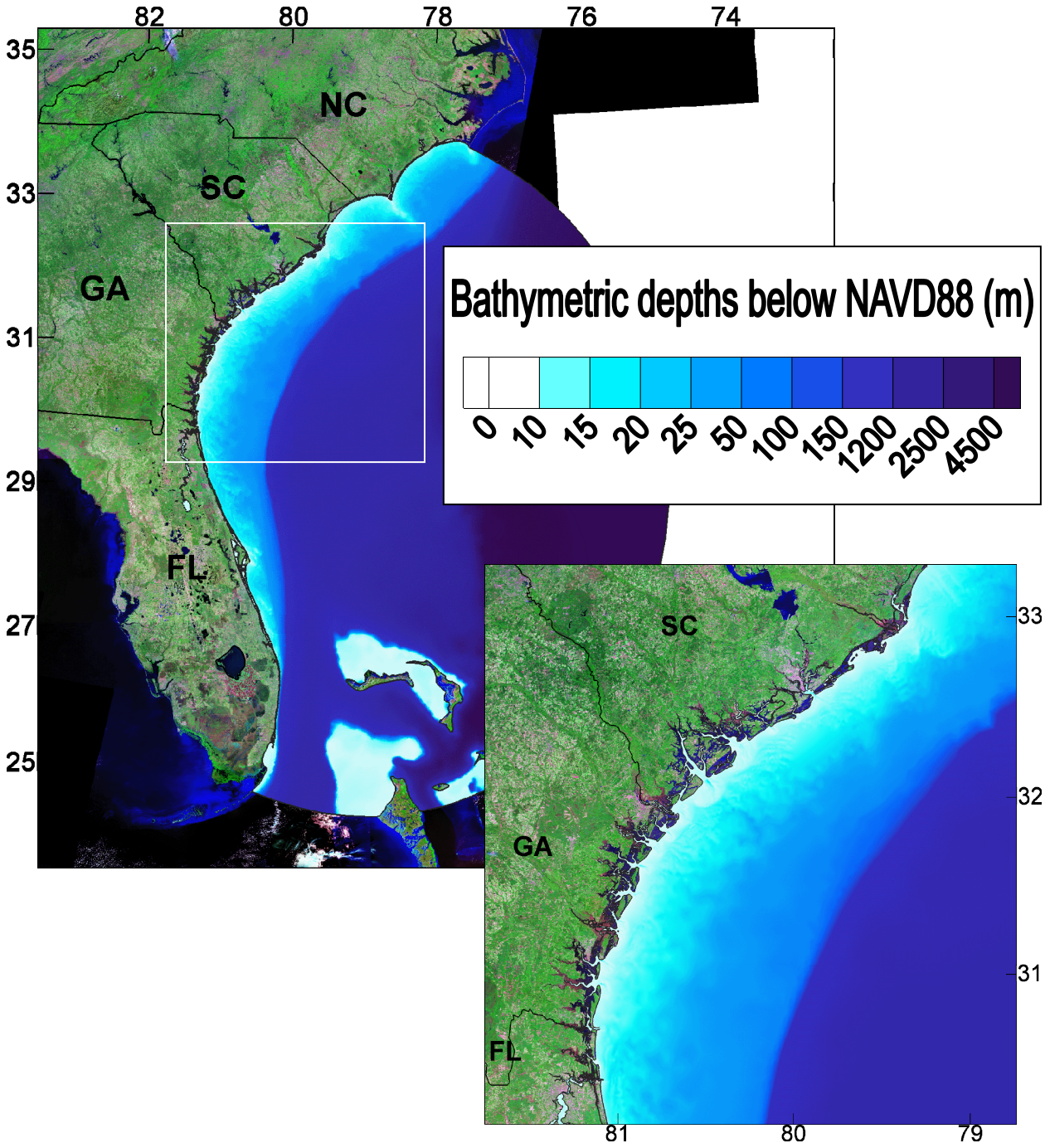

Figure 7.3. Mesh representation of the bathymetry for the South Atlantic Bight. The background is satellite imagery (sourced from the National Aeronautics and Space Administration). The inset follows from the box in the larger view.

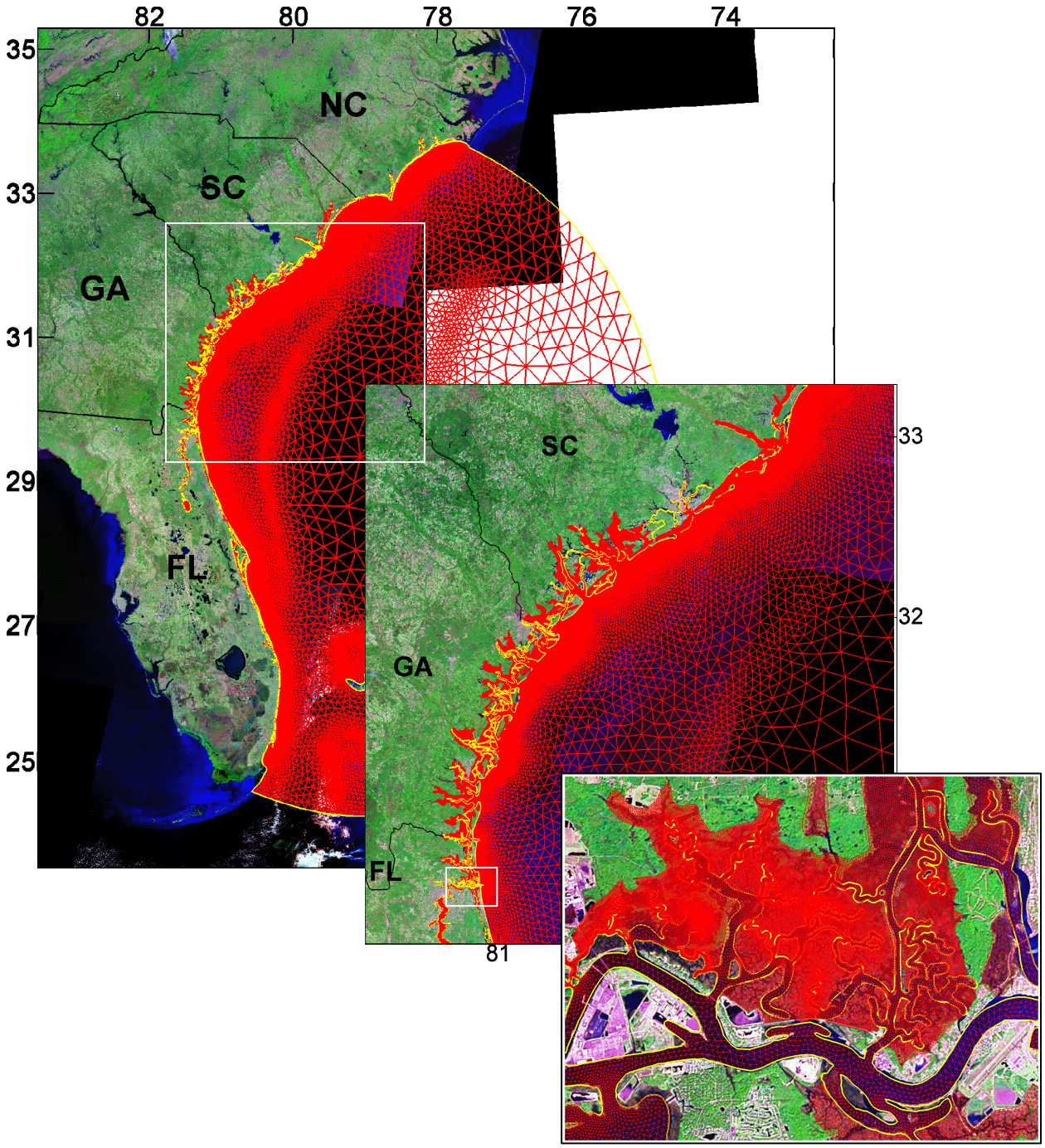

Figure 7.4. Triangulation of the intertidal zones and estuary waterbodies of the South Atlantic Bight (a.k.a. the MARSH mesh). The waterbody boundary is shown in yellow. The background is satellite imagery (sourced from the National Aeronautics and Space Administration). The insets follow from the boxes in the larger views.

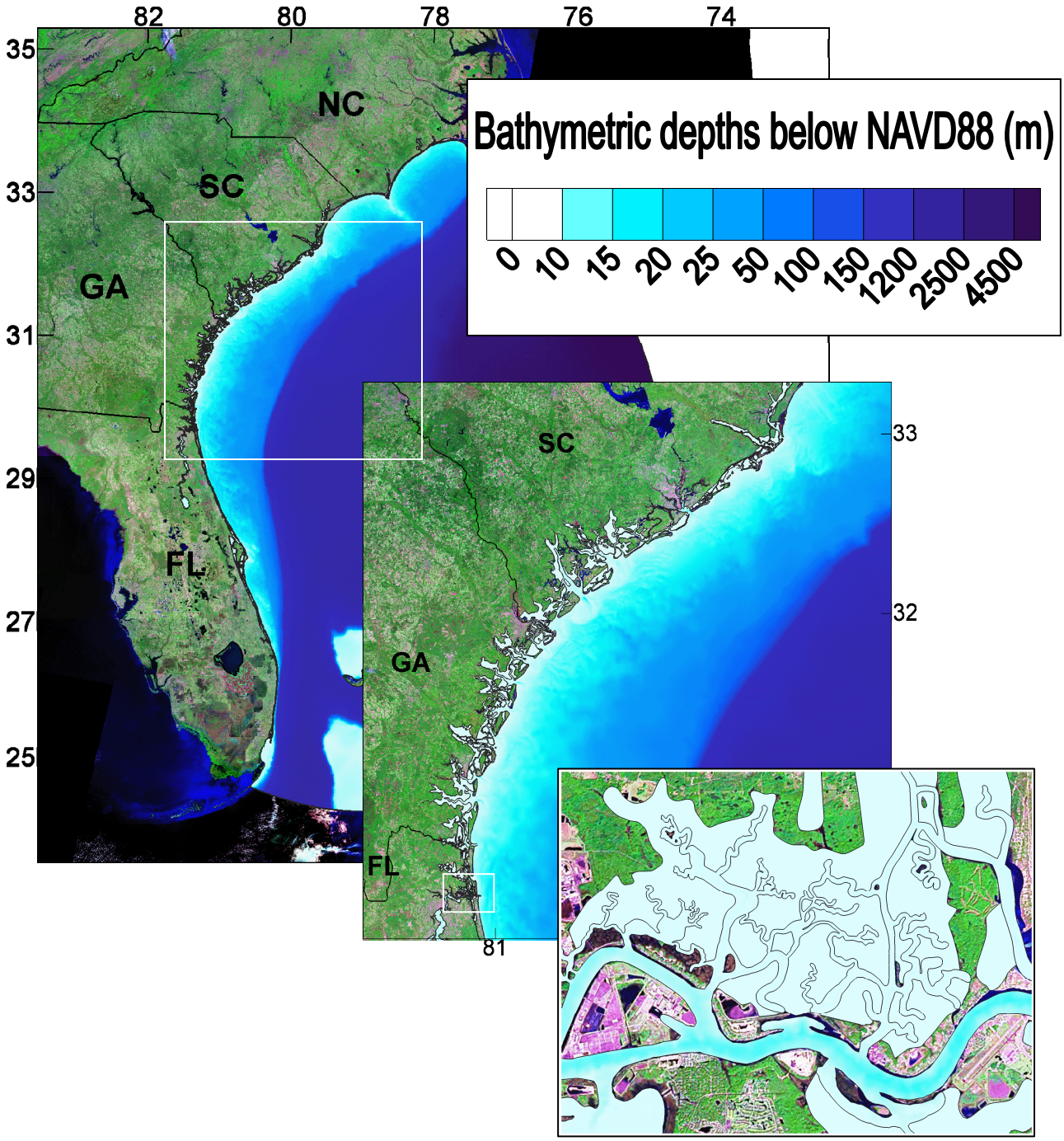

Figure 7.5. Model bathymetry of the intertidal zones and estuary waterbodies of the South Atlantic Bight. The background is satellite imagery (sourced from the National Aeronautics and Space Administration). The insets follow from the boxes in the larger views.

7.2. Mesh Variants

Three variants of the comprehensive mesh, herein referred to as MARSH, are developed by selectively removing estuarine features from the domain. Node placement is not changed in producing the mesh variants; only the removal of nodes takes place. The first mesh variant, herein referred to as AICWW, removes the intertidal zones (Figure 7.2). The second mesh variant, herein referred to as INLET, removes the Atlantic Intracoastal Waterway between adjacent estuary waterbodies (Figure 7.6). With this mesh variant, hydraulic connection between the estuary waterbodies is only through the tidal inlets. The INLET mesh consists of 230,062 nodes and 403,540 elements. The third mesh variant, herein referred to as COASTAL, removes all features landward of the tidal inlets (Figure 7.7). With this mesh variant, the coastline is not penetrated resulting in a geometry that is substantially distorted beyond the real case. The COASTAL mesh consists of 61,650 nodes and 119,324 elements.

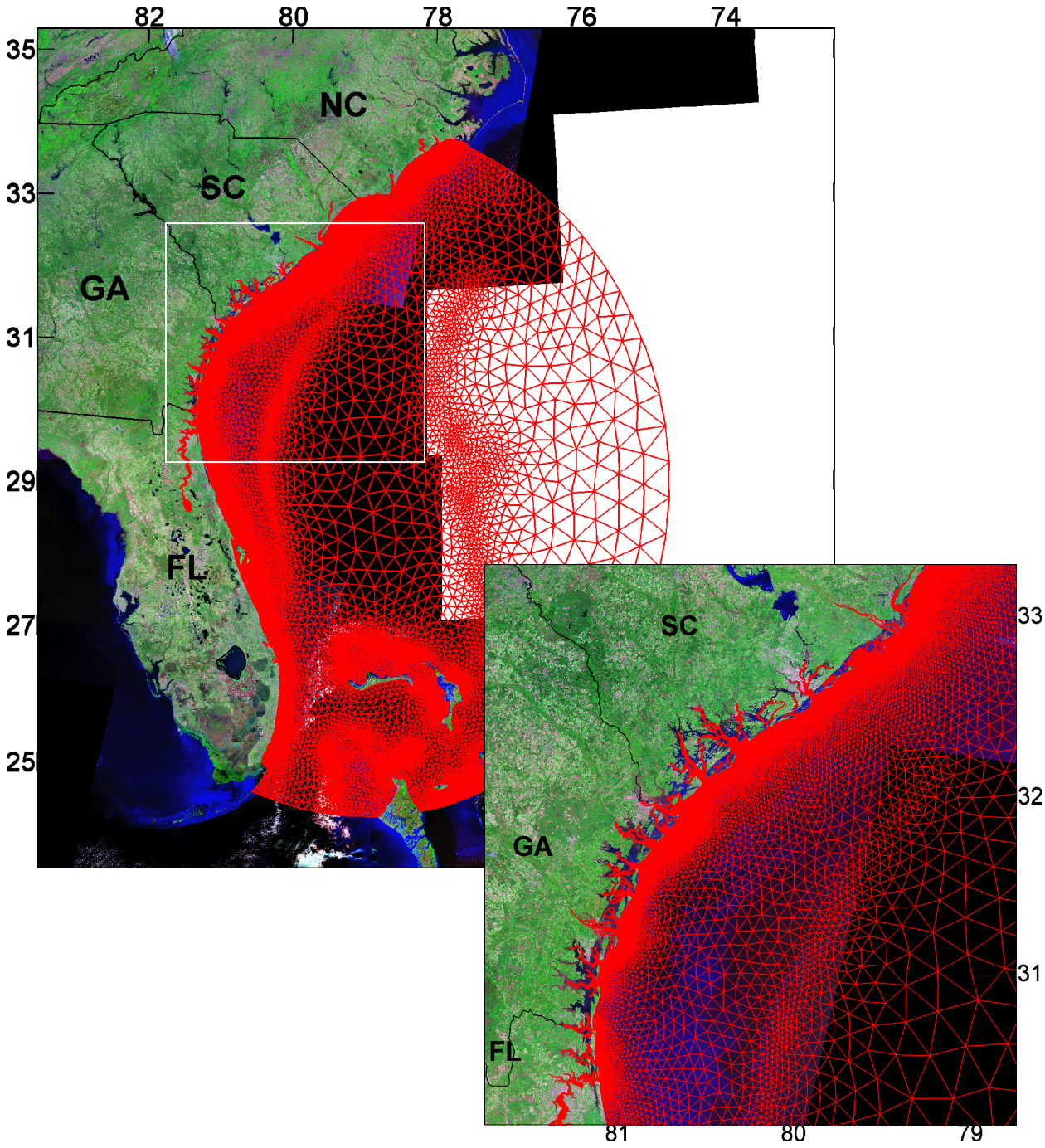

Figure 7.6. The INLET mesh is the comprehensive mesh with the intertidal zones and Atlantic Intracoastal Waterway removed. The background is satellite imagery (sourced from the National Aeronautics and Space Administration). The inset follows from the box in the larger view.

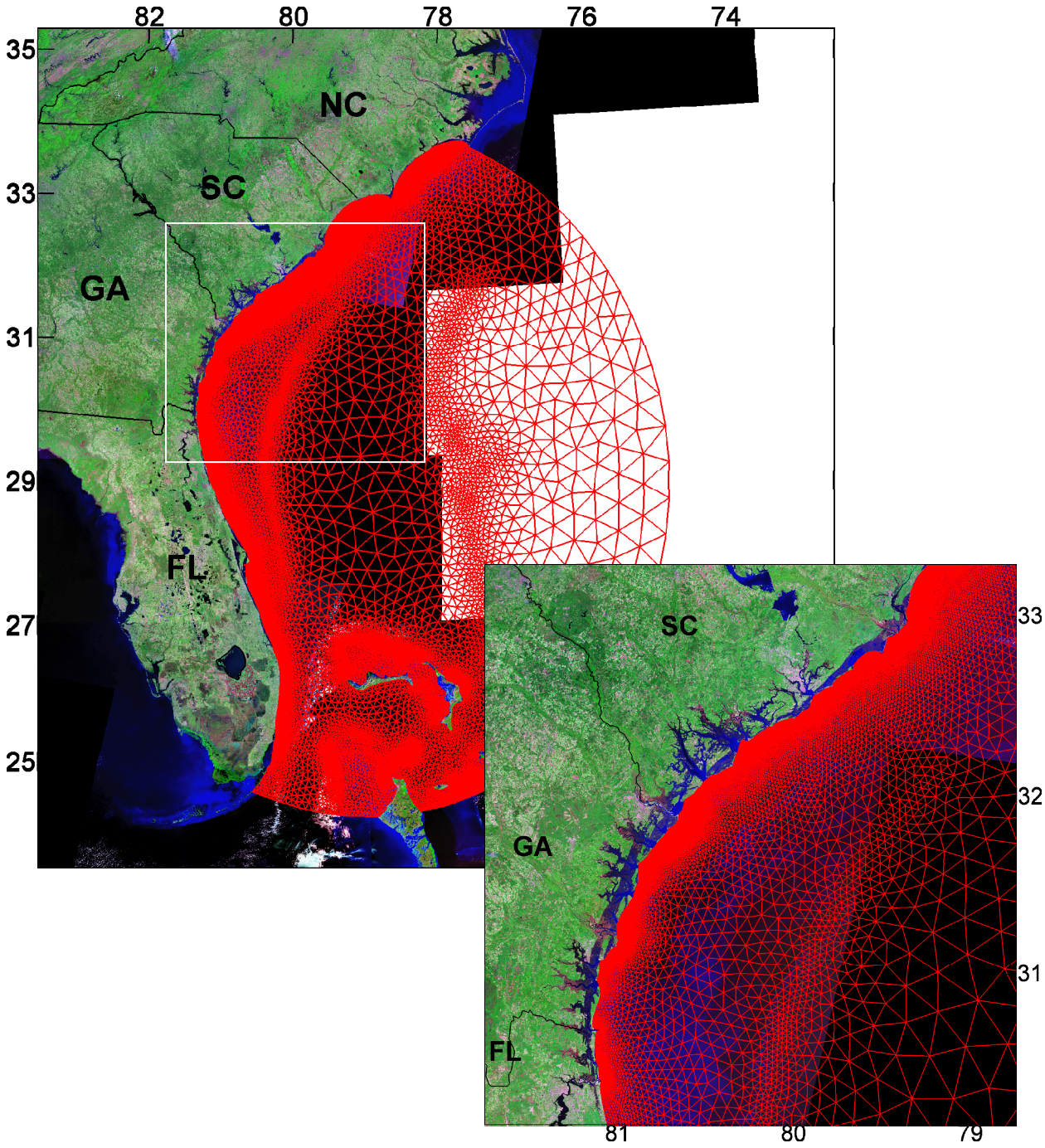

Figure 7.7. The COASTAL mesh is the comprehensive mesh with all estuarine features removed. The background is satellite imagery (sourced from the National Aeronautics and Space Administration). The inset follows from the box in the larger view.

CHAPTER 8. GOVERNING EQUATIONS AND DISCRETIZATION

ADCIRC-2DDI is the depth-integrated version of the hydrodynamic code ADCIRC and is governed by the shallow water equations (Luettich et al., 1992; Luettich and Westerink, 2006b). In their barotropic form, the shallow water equations are expressed in a spherical coordinate system as (Kolar et al., 1994a; Westerink et al., 2008):

$$\frac{\partial \zeta}{\partial t} + \frac{1}{R\cos\phi}\left[\frac{\partial UH}{\partial \lambda} + \frac{\partial \left(VH\cos\phi\right)}{\partial \phi}\right] = 0 \quad \ldots\ldots\ldots\ldots\ldots\ldots\ldots\ldots\ldots\ldots\ldots\ldots\ldots\ldots\ldots\ldots (8.1)$$

$$\underbrace{\frac{\partial U}{\partial t}}_{\text{Local acceleration}} + \underbrace{\frac{1}{R\cos\phi}U\frac{\partial U}{\partial \lambda}}_{\text{Advection}} + \underbrace{\frac{1}{R}V\frac{\partial U}{\partial \phi}}_{\text{Advection}} - \underbrace{\left(\frac{\tan\phi}{R}U + f\right)V}_{\text{Coriolis effects}} =$$

$$-\frac{1}{R\cos\phi}\frac{\partial}{\partial \lambda}\left[\underbrace{\frac{p_S}{\rho_0}}_{\text{Atmospheric pressure}} + g\left(\underbrace{\zeta}_{\text{Water-level pressure}} - \underbrace{\alpha\eta}_{\text{Local tide}}\right)\right] + \underbrace{\frac{1}{H}M_\lambda}_{\text{Diffusion}} + \underbrace{\frac{\tau_{S\lambda}}{\rho_0 H}}_{\text{Surface stress}} - \underbrace{\tau_* U}_{\text{Bottom stress}} \quad \ldots\ldots (8.2)$$

$$\underbrace{\frac{\partial V}{\partial t}}_{\text{Local acceleration}} + \underbrace{\frac{1}{R\cos\phi}U\frac{\partial V}{\partial \lambda}}_{\text{Advection}} + \underbrace{\frac{1}{R}V\frac{\partial V}{\partial \phi}}_{\text{Advection}} + \underbrace{\left(\frac{\tan\phi}{R}U + f\right)U}_{\text{Coriolis effects}} =$$

$$-\frac{1}{R}\frac{\partial}{\partial \phi}\left[\underbrace{\frac{p_S}{\rho_0}}_{\text{Atmospheric pressure}} + g\left(\underbrace{\zeta}_{\text{Water-level pressure}} - \underbrace{\alpha\eta}_{\text{Local tide}}\right)\right] + \underbrace{\frac{1}{H}M_\phi}_{\text{Diffusion}} + \underbrace{\frac{\tau_{S\phi}}{\rho_0 H}}_{\text{Surface stress}} - \underbrace{\tau_* V}_{\text{Bottom stress}} \quad \ldots\ldots\ldots (8.3)$$

where depth-integrated momentum dispersion in the longitudinal and latitudinal directions, respectively, is given by (Blumberg and Mellor, 1987; Kolar and Gray, 1990):

$$M_{\lambda,\phi} = \frac{E_{h_2}}{R^2}\left[\frac{1}{\cos^2\phi}\frac{\partial^2(U,V)H}{\partial\lambda^2} + \frac{\partial^2(U,V)H}{\partial\phi^2}\right] \quad \ldots\ldots\ldots\ldots\ldots\ldots\ldots\ldots\ldots\ldots\ldots\ldots\ldots\ldots\ldots\ldots (8.4)$$

and t = time; λ, ϕ = degrees longitude (east of Greenwich positive) and latitude (north of equator positive), respectively; U, V = depth-integrated velocity in the longitudinal (traversing meridians of longitude/east-west movement) and latitudinal (traversing parallels of latitude/north-south movement) directions, respectively; H = total height of the vertical water column, $h + \zeta$; h = bathymetric depth, relative to NAVD88; ζ = free surface elevation, relative to NAVD88; R = radius of the Earth; $f = 2\Omega\sin\phi =$ Coriolis parameter; Ω = angular speed of the Earth; p_S = atmospheric pressure at the free surface; ρ_0 = reference density of water; g = acceleration due to gravity; α = effective Earth elasticity factor (Schwiderski, 1980); E_{h_2} = horizontal eddy viscosity; $\tau_{S\lambda}$, $\tau_{S\phi}$ = applied free surface stress in the longitudinal and latitudinal directions, respectively; τ_* = quadratic bottom stress (details in the subsequent chapter); η = Newtonian equilibrium tide potential (Reid, 1990).

Finite element-based solutions to the shallow water equations in their primitive form are known to be susceptible to numerical noise (Gray, 1982). Therefore, the shallow water equations are reformulated into a Generalized Wave Continuity equation (Lynch and Gray, 1979). The Generalized Wave Continuity equation is derived by combining a time-differentiated form of the primitive continuity equation and a spatially differentiated form of the primitive, conservative momentum equations, and adding to this result, the primitive continuity equation

multiplied by a constant in time and space, τ_0, followed by a transformation of the advective terms into non-conservative form (Kolar et al., 1994b). The solution is implemented using a continuous Galerkin finite element method with Lagrange linear finite elements for spatial discretization and a three- and two-time-level implicit scheme for time stepping the Generalized Wave Continuity equation and primitive, non-conservative momentum equations, respectively (Luettich et al., 1992; Luettich and Westerink, 2006b).

CHAPTER 9. BOTTOM FRICTION PARAMETERIZATION

In hydrodynamic modeling, friction coefficients are commonly used to parameterize drag (Hsu et al., 1999). Drag refers to the hydraulic resistance occurring over the wetted perimeter of the flow. In the estuarine setting, hydraulic resistance generally accounts for roughness due to soil grain, bedform variations, and vegetation.

9.1. Overview of Approaches and Applications

Chow (1959) presents three parameters commonly used to represent hydraulic resistance: 1) Manning's roughness coefficient n; 2) Chezy's resistance factor C; and 3) the Darcy-Weisbach friction factor f. Manning's roughness is the most frequently used parameterization for the calculation of open channel flows:

$$Q = \frac{A}{n} R^{2/3} S_0^{1/2} \qquad (\text{metric units}) \ldots\ldots\ldots\ldots\ldots\ldots\ldots\ldots\ldots\ldots\ldots\ldots\ldots\ldots\ldots\ldots\ldots\ldots\ldots\ldots\ldots\ldots (9.1)$$

where S_0 relates to the bed slope and $R = A/P$ corresponds to the hydraulic radius of the flow with A being the cross-sectional area and P being the wetted perimeter. Manning's roughness coefficient depends primarily on material type and channel geometry: refer to Chow (1959) for a comprehensive tabulation. Barnes (1967) includes a cataloging of Manning's n values for typical rivers and creeks ranging from 0.024 to 0.075.

Arcement and Schneider (1989) provide guidance for selecting Manning's roughness coefficients for natural channels and floodplains. They present the Manning's n value for floodplains as being the composite effect of (Cowen, 1956):

$$n = (n_0 + n_1 + n_2 + n_3 + n_4)m \quad \ldots\ldots\ldots\

9.2. Quadratic Bottom Friction Formulation

Bottom stress in the shallow water equations (see Eqs. [8.2] and [8.3]) can be computed with a quadratic formulation with respect to the depth-integrated velocity:

$$\tau_* = \frac{C_f \sqrt{U^2 + V^2}}{H} \quad \ldots\ldots\ldots\

$$C_{f_{\min}} = C_{f_{\min}} \qquad (\text{user} - \text{specified constant}) \quad \ldots\ldots\ldots\

used by Mattocks et al. (2006). A slightly larger Manning's *n* value of 0.033 is assigned to "seagrass beds" (class 9110), which are distributed throughout the Indian River lagoon (Figure 5.4).

Larger Manning's *n* values are assigned to the intertidal zones: 0.100 for "woody wetlands" (class 90) and 0.050 for "emergent herbaceous wetlands" (class 95). Figure 9.1 shows the delineation of these two intertidal classes relative to "open water" (class 11) in terms of the assigned Manning's *n* values. "Woody wetlands" occupy roughly one-third of the overall intertidal surface area: $1.1\times10^{3}\,\mathrm{km}^{2}$ compared to $2.5\times10^{3}\,\mathrm{km}^{2}$ for "emergent herbaceous wetlands." The Manning's *n* values selected fall within the respective ranges for floodplains with and without brush given by Chow (1959). These values are in the respective ranges defined for "very large" and "large" amounts of vegetation by Arcement and Schneider (1989). These values are at or near those used by Mattocks et al. (2006). Figure 9.2 shows the spatial distribution of Manning's *n* values interpolated to the nodes of the MARSH mesh.

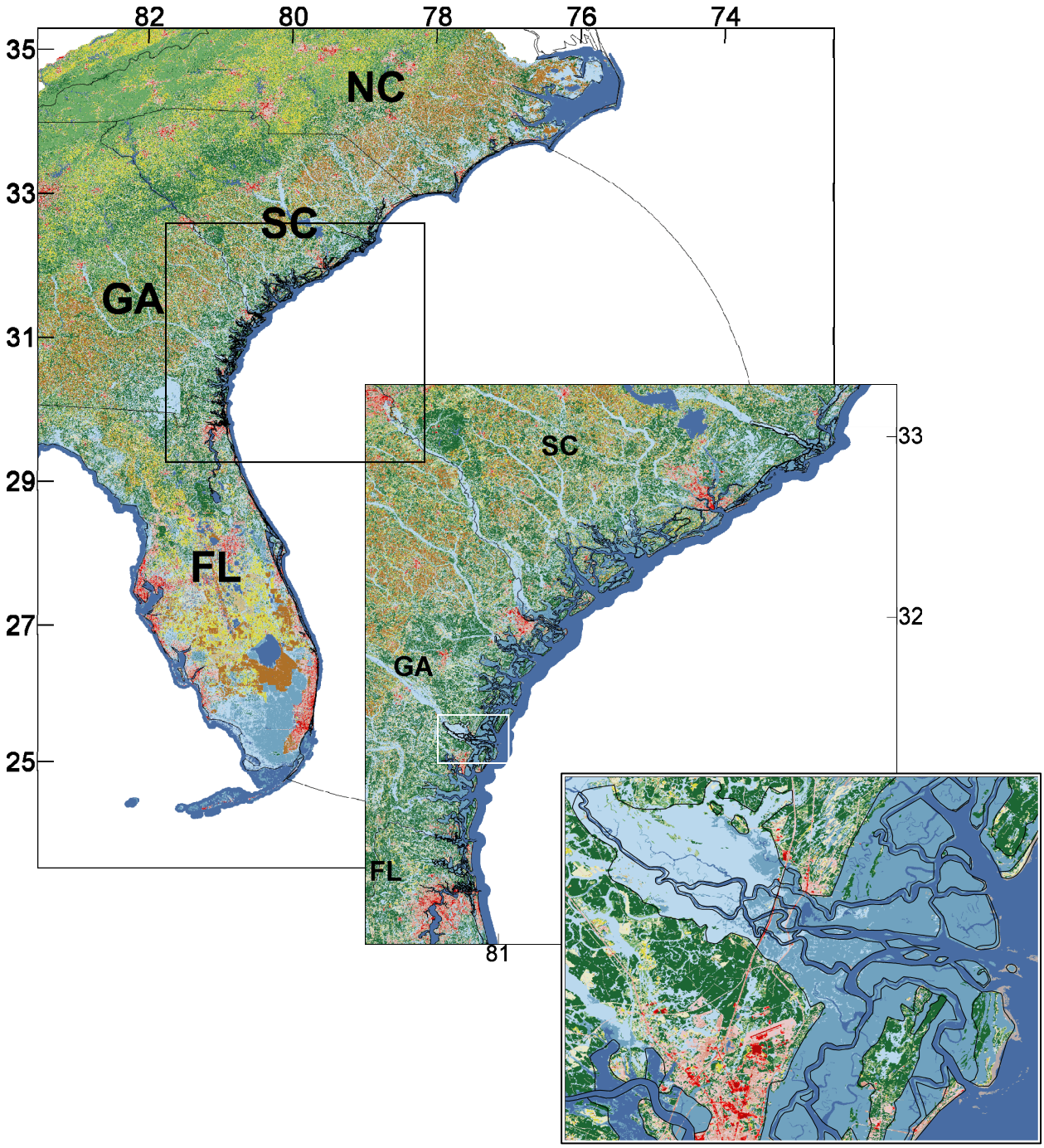

Figure 9.1. Assignment of Manning's *n* values for the estuary waterbodies (dark blue) and intertidal zones (medium blue for "emergent herbaceous wetlands" and light blue for "woody wetlands"). The background is a National LandCover Database 2001 raster map. The insets follow from the boxes in the larger views.

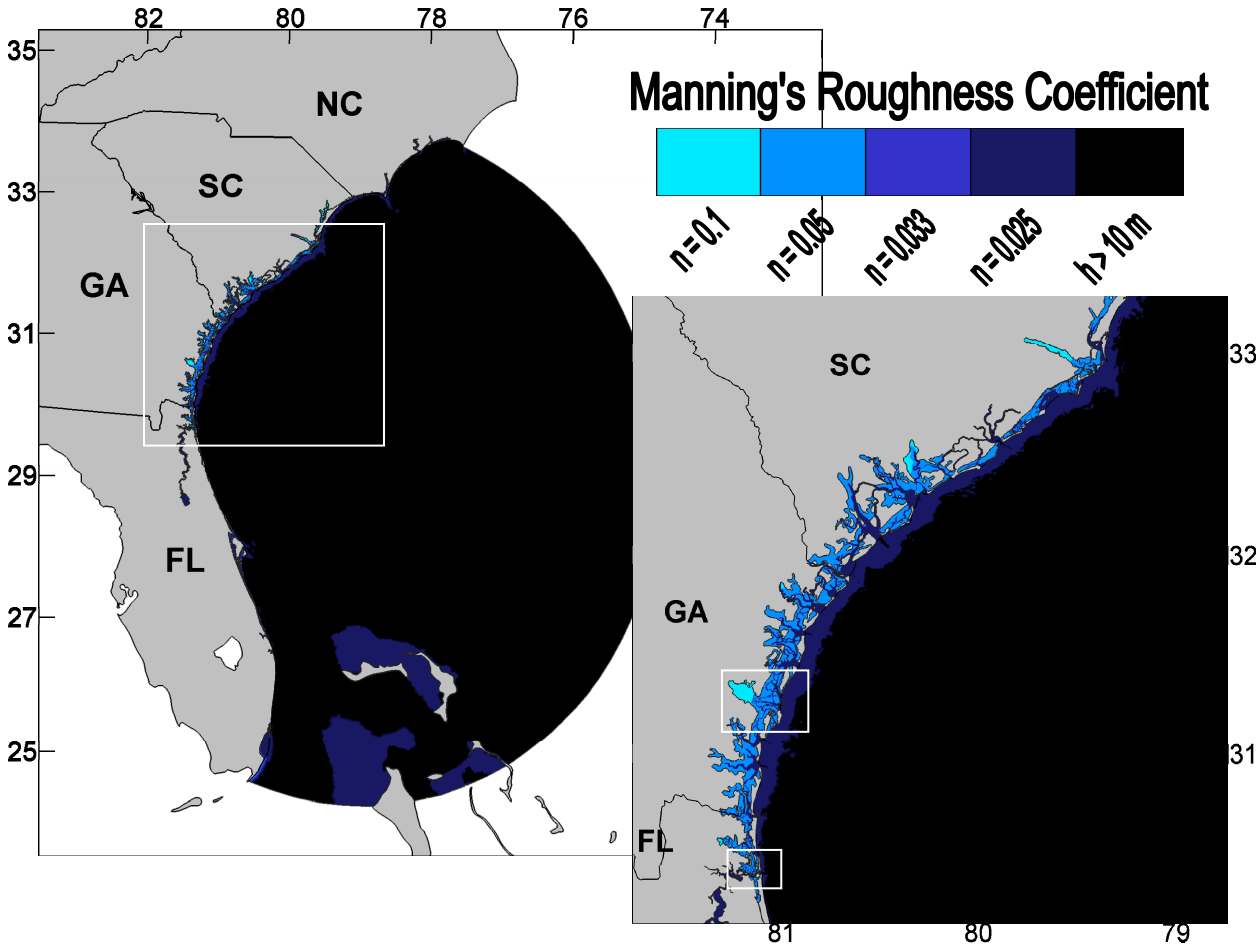

Figure 9.2. Spatial distribution of Manning's n values interpolated to the nodes of the MARSH mesh. Areas colored in black indicate where bathymetric depths are greater than the break depth $h > h_{break}$: such areas receive a constant value for the minimum bottom friction coefficient $C_{f_{\min}} = 0.0030$. Blue shades are for bathymetric depths less than the break depth $h < h_{break}$ and indicate the related values of the Manning's roughness coefficient n : such areas calculate the minimum bottom friction coefficient in terms of the bathymetric depth and Manning's n value (Eq. [9.6]). The insets corresponding to the boxes on the smaller view are shown on the following page.

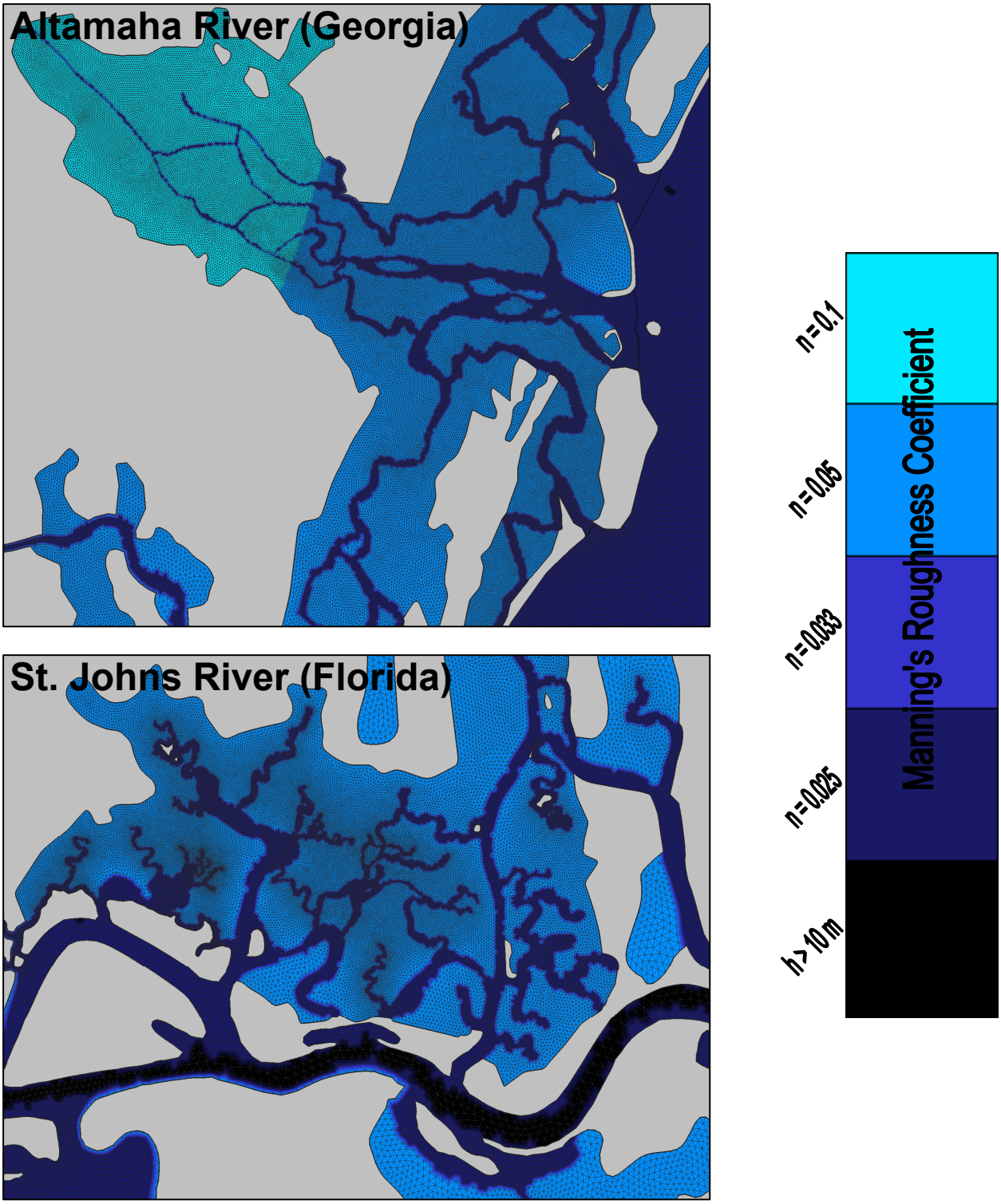

Figure 9.2. Continuation from the previous graphic: insets of the Altamaha (Georgia) and St. Johns Rivers (Florida) corresponding to the boxes in the smaller view.

Figure 9.3 shows the variation of the minimum bottom friction coefficient with bathymetric depth for the different Manning's *n* values used herein. The curve for "seagrass beds" (class 9110) is truncated after the 5-m depth: the maximum depth in the Indian River lagoon. "Seagrass beds" (class 9110) have larger friction coefficients relative to those for "open water" (class 11). The plot for the intertidal zones is truncated after the 2-m depth: equal to the extreme maximum tidal height in the region (Center for Operational Oceanographic Products and Services: website http://tidesandcurrents.noaa.gov/ accessed on March 15, 2008). The coefficients scale for the intertidal zones is an order of magnitude greater than that for the estuary waterbodies. The coefficients for "woody wetlands" (class 90) are four times larger than those for "emergent herbaceous wetlands" (class 90) due to the quadratic relationship $C_{f_{\min}} \propto n^2$ in Eq. (9.6): $\left(n_{90} = 0.100\right) = 2 \times \left(n_{95} = 0.050\right)$.

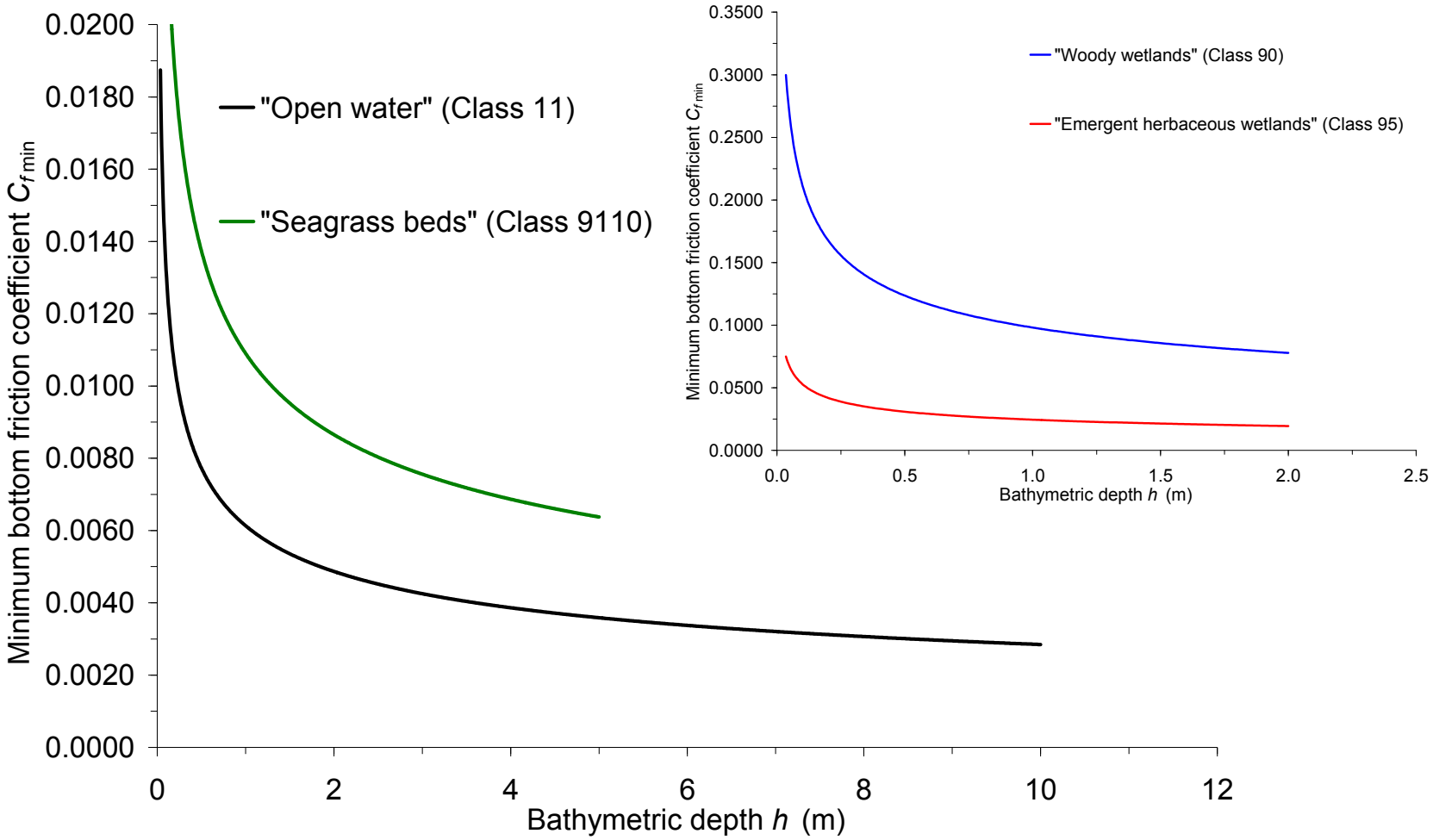

Figure 9.3. Variation of the minimum bottom friction coefficient with bathymetric depth for the different Manning's n values used herein. The larger view corresponds to "open water" (class 11) and "seagrass beds" (class 9110) and the inset corresponds to "woody wetlands" (class 90) and "emergent herbaceous wetlands" (class 95).

CHAPTER 10. BOUNDARY CONDITIONS AND MODEL SETTINGS

The open boundary is an arc that sweeps from Cape Lookout, North Carolina to the Florida Keys: generally situated in deep water. The exceptions to this are some shallow regions around the Bahamas. Boundary conditions in this study come from the Western North Atlantic Tidal model domain (Hagen et al., 2006) which resolves these shallow regions. The boundary condition consists of a water surface elevation constructed as the superposition of 7 astronomical tidal constituents (K_1, O_1, M_2, S_2, N_2, K_2, and Q_1). Zero-flux boundary conditions are imposed along all mainland and island boundaries.

ADCIRC is then set up to run as follows: simulations begin from a cold start and at the beginning of a tidal epoch; boundary forcings are ramped over the first 15 days of the run; 90 days of real time is simulated with a time step of 3 seconds; the last 45 days of the simulated water surface elevations are harmonically analyzed for 23 frequencies ranging from fortnightly to eighth-diurnal speeds; the advective terms (see Eqs. [8.2] and [8.3]) are enabled; the horizontal eddy viscosity coefficient (see Eq. [8.4]) is set to 5.0 m^2/s; wetting and drying is enabled with the minimum water column depth H_0 set to 0.035 m (i.e., computational nodes and the accompanying elements with water depths less than the prescribed minimum bathymetric depth are considered to be dry); the weighting parameter in the Generalized Wave Continuity equation, τ_0, is set to a value of –0.01 (Kolar et al., 1994b).

CHAPTER 11. MODEL VALIDATION

11.1. Gaging Stations and Data

Model performance is assessed at 103 gaging stations in the South Atlantic Bight (Figure 11.1). Table 11.1 partitions the gaging stations based on their geographical location: 1) 69 stations in the estuaries; 2) 28 coastal or shelf stations; and 3) six stations off the bight shelf. Estuary stations are those found landward of the uninterrupted coastline: the coastline that would be present in the absence of any tidal inlets. The estuary stations span the entire coastline of the South Atlantic Bight and reach as far inland as 150 km upstream in the Lower St. Johns River. Also included with the estuary stations are those located in the Atlantic Intracoastal Waterway. Coastal or shelf stations are seaward of the uninterrupted coastline but within the shelf break. The stations off the bight shelf are seaward of the break.

Table 11.2 reports water level amplitudes and phases for 33 of the overall 103 gaging stations in the South Atlantic Bight. These 33 stations provide full coverage for the South Atlantic Bight and are used to summarize tidal elevations in the geographical region. Data are presented for the M2, N2, S2, K1, O1, M4, M6, and M8 tidal constituents by the National Ocean Service, St. Johns River and South Florida Water Management Districts, Seim (2000), Blanton et al. (2004), and the International Hydrographic Organization (website http://www.iho.shom.fr/ accessed on March 14, 2005). The M2, N2, and S2 are the dominant semi-diurnal frequencies in the domain, the K1 and O1 are the dominant diurnal frequencies, and the M4, M6, and M8 are

the nonlinearly generated overtides of the M2 constituent. Such data are available for all 103 gaging stations and are used in the forthcoming validation process.

Foremost, the M2 tidal constituent dominates water levels in the South Atlantic Bight (Table 11.2). Throughout the domain, the M2 constituent accounts for roughly half of the overall tidal signal. M2 amplitude is greatest at station PUL located inside Tybee Roads Entrance (Georgia): 1.013 m. M2 amplitude decreases north and south: 0.783 m at station ChHr inside Charleston Harbor (South Carolina) and 0.662 m at station MAY inside Mayport Entrance (Florida), respectively. The northernmost and southernmost deep ocean stations exhibit this as well: 0.487 at station I422 and 0.402 m at station I355.

Cross-shelf amplification of the M2 tide is exemplified by the growth of its amplitude from 0.441 m at station I41 in the deep ocean to 0.760 m at station R5 on the shelf to 0.976 m at station SIM at the coast (Table 11.2). The two stations in Onslow Bay show slight amplification: 0.460 m at station OB63 to 0.550 m at station OB27. M2 amplification is less pronounced off Florida's southeastern coast where the shelf narrows: 0.405 m at station SPGB off the bight shelf to 0.419 m at station LWPr at the coast.

In shallow waters, nonlinear effects cause the M2 tide to disperse into higher harmonics: the M4, M6, and M8 overtides. Along the coast and inside the estuaries, the M4, M6, and M8 overtides contribute to the overall tidal signal (Table 11.2). Note that the M4, M6, and M8 overtides are not reported in deep waters because they are minimal there.

The shelf/coastal and offshelf stations exhibit equatorward phase propagation (Table 11.2). Cross-shelf phase propagation is variable in the latitudinal direction: the tides are in phase in the north (stations OB27 and OB63) and south (stations SPGB and LWPr) and the tides lag by

about one hour in the middle (stations I41, R5, and SIM). Phase delays are around four hours within the estuaries: stations SEB, FtP, LUC, and CGD.

Tidal velocity data are available for nine gaging stations in the South Atlantic Bight (Figure 11.1; Table 11.1): five are located on the shelf (R6, R2, GR, R5, and OB27), one near the coast (LB), and three in the Lower St. Johns River (MAY, FUL, and JAX). Tidal ellipse parameters (semi-major and semi-minor axes, inclination, and phase) are reported for the M2 and K1 tidal constituents at the six shelf/coastal stations (Table 11.3). Semi-major axes and phase angles are reported for the M2, N2, S2, K1, and O1 tidal constituents at the three estuary stations (Table 11.4). The data are tabulated adjacent to model results for purposes of assessing model performance (discussed later in this section).

Tidal velocities on the continental shelf are dominated by the M2 constituent. Peak M2 velocities on the shelf are between 25 and 30 cm/s (Table 11.3). Tidal ellipses are generally directed shoreward at 150° counterclockwise from due east and have eccentricities greater than ω/f:

$$\left(e_{\mathrm{M2}} = \left[\frac{u}{v} \right]_{\mathrm{M2}} \approx \left| \frac{0.300}{-0.100} \right| = 3.000 \right) > \left(\frac{\omega_{\mathrm{M2}}}{f} = \frac{1.41 \times 10^{-4}\ \mathrm{rad/s}}{7.29 \times 10^{-5}\ \mathrm{rad/s}} = 1.93 \right) \quad \ldots\ldots\ldots\ldots\ldots\ldots (11.1)$$

which is indicative of standing wave dynamics (refer to Appendix A). The negative values for the semi-minor axis indicate that the tides rotate clockwise (refer to Appendix B). The tidal ellipses narrow as the coast is approached: compare station LB to the others. M2 velocities are generally in phase and lag water levels by about three hours. Diurnal tides are an order of magnitude smaller than the semi-diurnal tides and exhibit less eccentricity.

Tidal velocities in the Lower St. Johns River are dominated by the M2 constituent. Peak M2 velocities in the Lower St. Johns River are 1 m/s at the mouth and decrease to 0.8 and 0.65 m/s at river kilometers 12 and 25: stations MAY, FUL, and JAX respectively (Table 11.4). The flow is strongly rectilinear and aligns itself along the channel axis. Thus, the velocities can be described by only the semi-major axis and phase. Relative to station MAY, M2 velocities peak one hour later at station FUL and two hours later at station JAX. Comparing Tables 11.3 and Tables 11.4, peak M2 velocities take about four hours to propagate from the shelf to the estuaries.

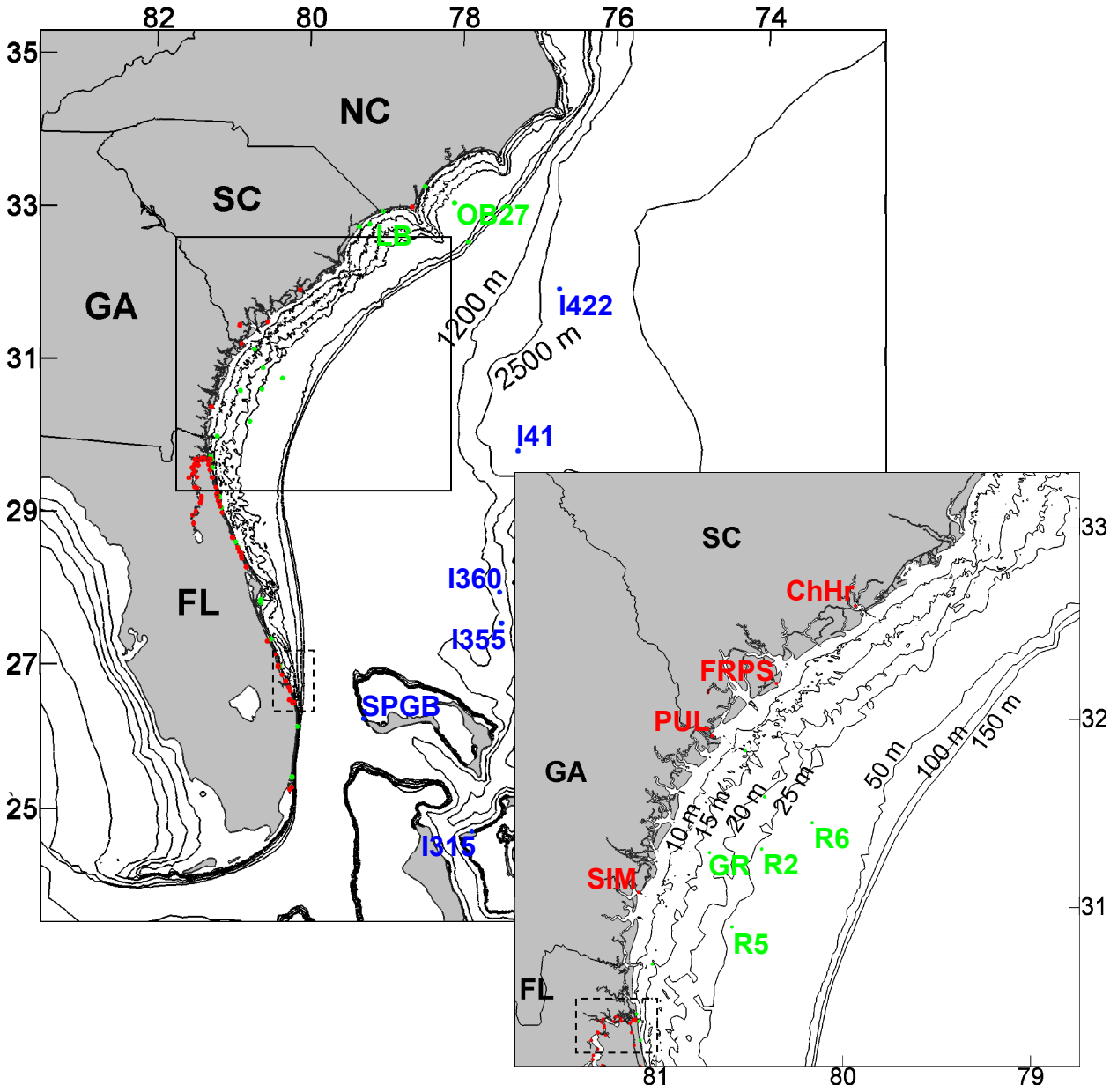

Figure 11.1. Model performance is assessed at 103 gaging stations in the South Atlantic Bight partitioned by their geographical location: estuary (red); shelf/coastal (green); and offshelf (blue). Tidal velocity data are provided for six stations on the shelf (green labels). Stations with labels are referenced in the text. Station information is included in Table 11.1. The inset follows from the solid box in the larger view. The insets corresponding to the dashed boxes are shown on the following pages.

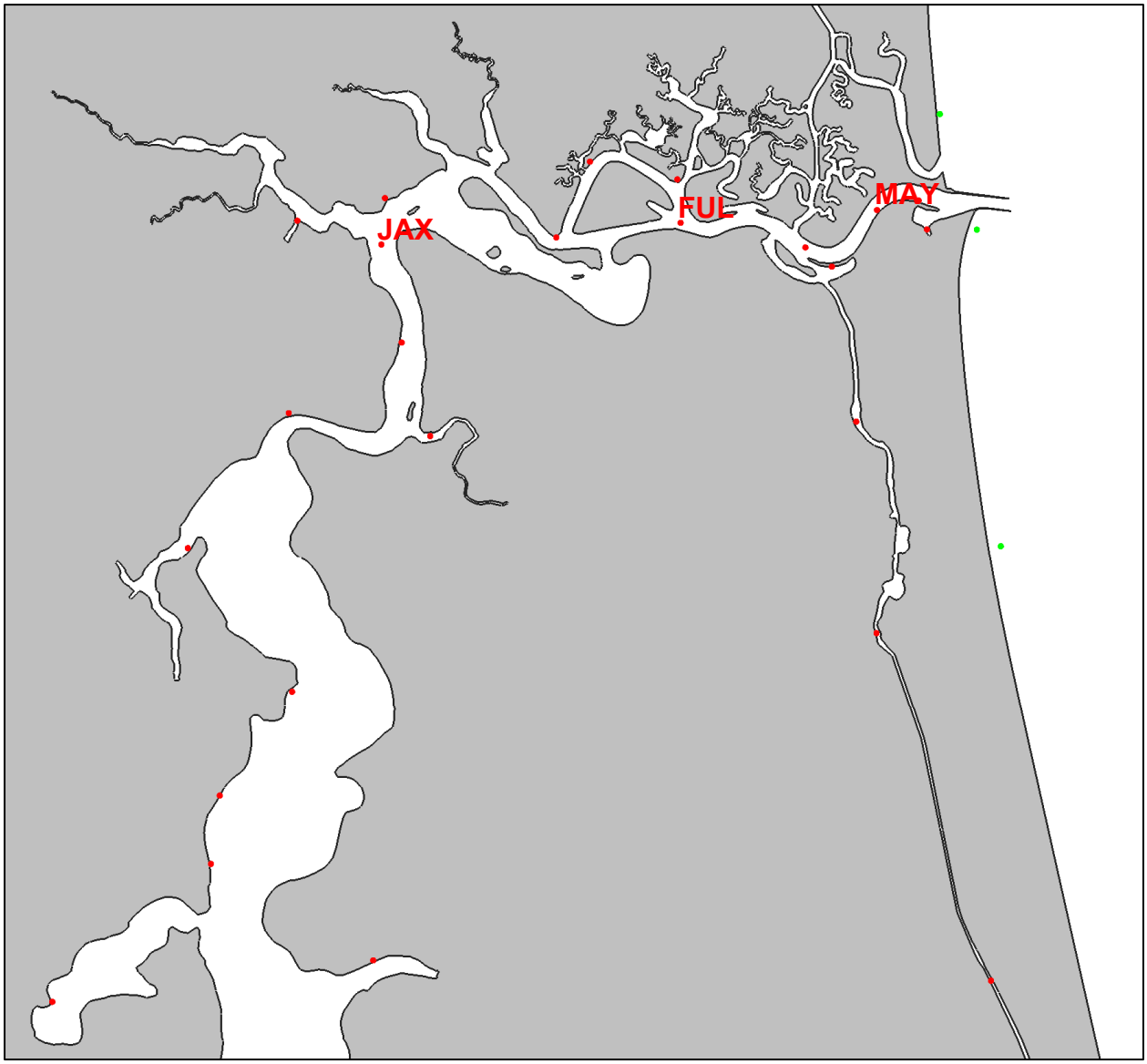

Figure 11.1. Continuation from the previous graphic: inset of the Lower St. Johns River and adjoining Atlantic Intracoastal Waterway corresponding to the dashed box in the smaller view. Tidal velocity data are provided for three stations in the estuaries (labeled). Station information is included in Table 11.1.

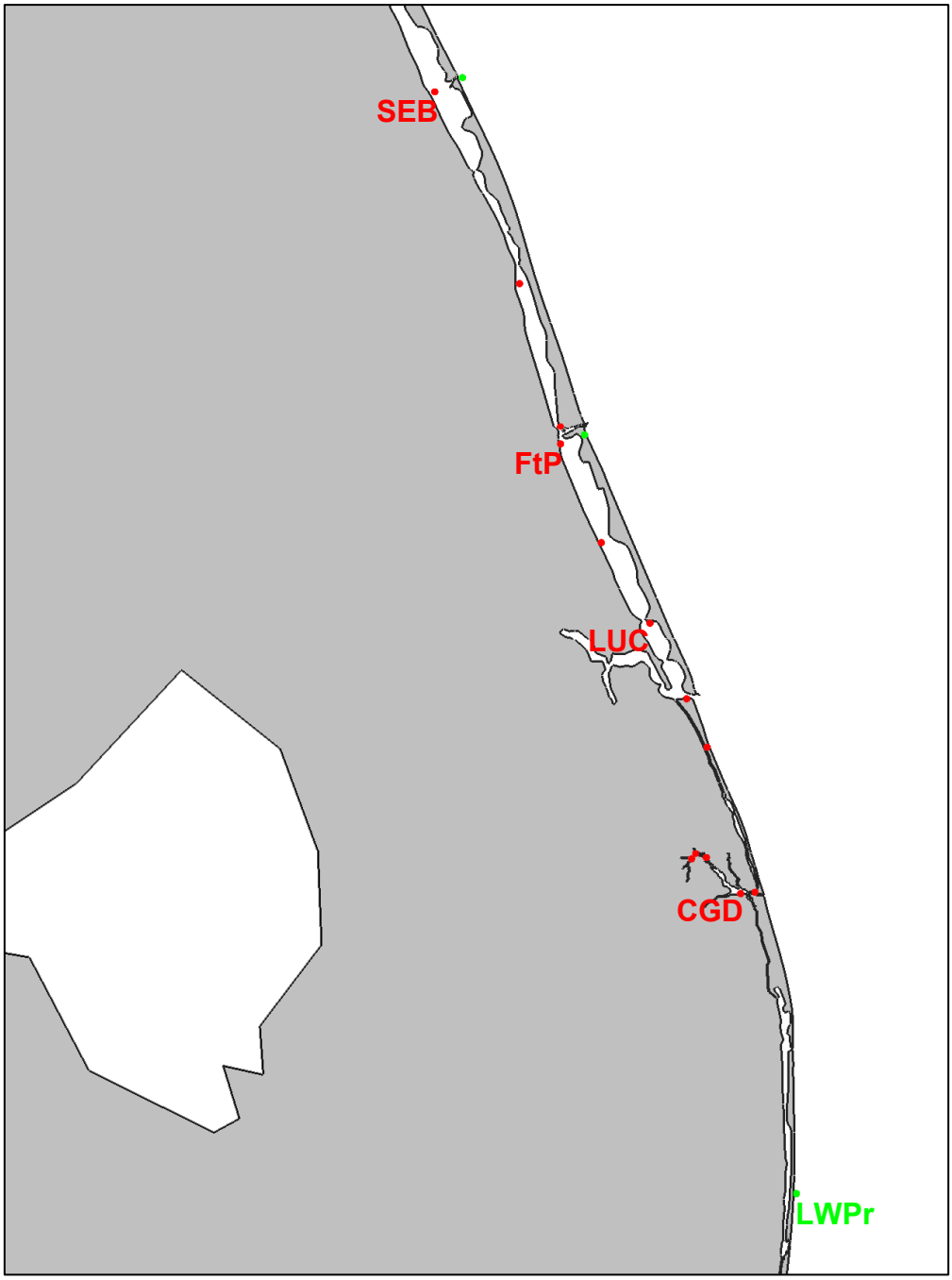

Figure 11.1. Continuation from the previous graphic: inset of the southern portion of the Indian River lagoon, the St. Lucie and Loxahatchee Rivers, and Lake Worth lagoon corresponding to the dashed box in the larger view. Stations with labels are referenced in the text. Station information is included in Table 11.1.

Table 11.1. Model performance is assessed at 103 gaging stations in the South Atlantic Bight partitioned by their geographical location: estuary; shelf/coastal; and offshelf. Tidal velocity data are provided for nine stations (shaded rows).

Name	Abbr[a]	Source[b]	°W	°N
Estuary (69 stations)[c]				
WWTD, Mayport Naval Station, FL	–	NOS	–81.413333	30.400000
Bar Pilots Dock, FL	–	NOS	–81.430000	30.396667
Dame Point, FL	–	NOS	–81.558333	30.386667
Mayport, FL	MAY	NOS	–81.431667	30.393333
Main Street Bridge, FL	–	NOS	–81.658333	30.320000
Longbranch, FL	–	NOS	–81.620000	30.360000
I-295 Bridge, West End, FL	–	NOS	–81.691667	30.191667
Red Bay Point, FL	–	NOS	–81.628333	29.978333
Racy Point, FL	–	NOS	–81.548333	29.801667
Buffalo Bluff, FL	–	NOS	–81.681667	29.595000
Palatka, FL	–	NOS	–81.631667	29.643333
Welaka, FL	–	NOS	–81.675000	29.476667
Clapboard Creek, FL	–	NOS	–81.510000	30.407000
Blount Island Bridge, FL	–	NOS	–81.545000	30.413000
St. Johns River, WWTP, FL	–	SJRWMD	–81.410000	30.390000
Jacksonville, Navy Fuel Depot, FL	JAX	NOS	–81.627000	30.400000
Moncrief Creek Entrance, FL	–	NOS	–81.662000	30.392000

Name	Abbr[a]	Source[b]	°W	°N
Fulton, St. Johns River, FL	FUL	NOS	–81.507000	30.390000
Phoenix Park, FL	–	NOS	–81.637000	30.383000
USACE Dredge Depot, FL	–	SJRWMD	–81.620000	30.350000
Jacksonville, Acosta Bridge, FL	–	NOS	–81.665000	30.325000
Little Pottsburg Creek, FL	–	NOS	–81.610000	30.310000
Ortega River Entrance, FL	–	NOS	–81.705000	30.278000
Piney Point, St. Johns River, FL	–	NOS	–81.663000	30.228000
Orange Park, St. Johns River, FL	–	NOS	–81.695000	30.168000
Doctors Lake, Peoria Point, FL	–	NOS	–81.758000	30.120000
Julington Creek, FL	–	NOS	–81.630000	30.135000
Green Cove Springs, St. Johns River, FL	–	NOS	–81.663000	29.990000
East Tocoi, St. Johns River, FL	–	NOS	–81.553000	29.858000
Palmetto Bluff, St. Johns River, FL	–	NOS	–81.562000	29.763000
Pablo Creek Entrance, FL	–	NOS	–81.448000	30.377000
Pablo Creek, FL	–	NOS	–81.438000	30.323000
Oak Landing, FL	–	SJRWMD	–81.420000	30.250000
Palm Valley, FL	–	SJRWMD	–81.380000	30.130000
Tolomata River, AIW, FL	–	SJRWMD	–81.320000	29.990000
Vilano Bridge, FL	–	SJRWMD	–81.300000	29.910000
St. Augustine, FL	–	NOS	–81.310000	29.892000

Name	Abbr[a]	Source[b]	°W	°N
CR312 Bridge, St. Augustine, FL	–	SJRWMD	–81.300000	29.860000
Anastasia Island, FL	–	NOS	–81.272000	29.793000
Crescent Beach, FL	–	SJRWMD	–81.250000	29.760000
Fort Matanzas, FL	FtMz	NOS	–81.238000	29.715000
Matanzas River Headwaters, FL	–	NOS	–81.210000	29.630000
Ormond Beach, FL	–	SJRWMD	–81.050000	29.280000
Port Orange, FL	–	SJRWMD	–80.970000	29.140000
Halifax River, Ponce Inlet, FL	–	NOS	–80.937000	29.082000
Ponce de Leon Inlet (South), FL	–	SJRWMD	–80.910000	29.060000
New Smyrna Beach, FL	–	SJRWMD	–80.910000	29.020000
Edgewater (FDEP 2005), FL	–	SJRWMD	–80.904000	28.993000
Oak Hill (FDEP 2005), FL	–	SJRWMD	–80.832000	28.866000
Sebastian River, Roseland, FL	SEB	SJRWMD	–80.500000	27.830000
Vero Bridge, FL	–	SJRWMD	–80.370000	27.630000
Fort Pierce Causeway, FL	–	SJRWMD	–80.320000	27.470000
Fort Pierce, FL	FtP	SJRWMD	–80.320000	27.450000
Ankona, Indian River Lagoon, FL	–	SJRWMD	–80.270000	27.340000
Jensen Beach, FL	–	SJRWMD	–80.210000	27.250000
South Point, St. Lucie Inlet, FL	LUC	SJRWMD	–80.165000	27.164000
Jupiter Island, AIW, FL	–	SJRWMD	–80.140000	27.110000

Name	Abbr[a]	Source[b]	°W	°N
Coast Guard Dock, FL	CGD	SFWMD	–80.081949	26.947236
Pompano Drive, FL	–	SFWMD	–80.099723	26.945833
Boy Scout Dock, FL	–	SFWMD	–80.141864	26.986286
Kitching Creek, FL	–	SFWMD	–80.155060	26.991015
River Mile 9.1, FL	–	SFWMD	–80.160221	26.984851
428 South Port, NC	–	IHO	–78.016660	33.915000
8665530 Charleston, Cooper River Entrance, SC	ChHr	NOS	–79.925000	32.781670
8668498 Hunting Island Pier, Fripps Inlet, SC	FRPS	NOS	–80.465000	32.340000
8670870 Fort Pulaski, Savannah River, GA	PUL	NOS	–80.901670	32.033330
8677344 St. Simons Lighthouse, St. Simons Island, GA	SIM	NOS	–81.396670	31.131670
8723178 Miami Beach, Government Cut, FL	–	NOS	–80.130000	25.763330
8723214 Virginia Key, Biscayne Bay, FL	BIS	NOS	–80.161670	25.731670
Shelf/coastal (28 stations)[d]				
St. Mary's River, Cut 2, FL	StM	SJRWMD	–81.302000	30.717000
Little Talbot Island, FL	–	NOS	–81.405000	30.430000
Navy Degaussing, FL	–	SJRWMD	–81.390000	30.390000
Jacksonville Pier, FL	–	SJRWMD	–81.380000	30.280000
St. Augustine Beach, Atlantic Ocean, FL	StA	NOS	–81.263000	29.857000
Matanzas Inlet, FL	–	SJRWMD	–81.220000	29.700000
Daytona Beach, Atlantic Ocean, FL	–	NOS	–81.000000	29.220000

Name	Abbr[a]	Source[b]	°W	°N
Daytona Beach Shores, FL	–	NOS	–80.963000	29.147000
Cocoa Beach, Atlantic Ocean, FL	–	SJRWMD	–80.600000	28.368000
Sebastian Inlet, FL	–	SJRWMD	–80.440000	27.860000
Fort Pierce Inlet, FL	–	SJRWMD	–80.290000	27.460000
8658163 Wrightsville Beach, NC	–	NOS	–77.795000	34.210000
8659897 Sunset Beach Pier, Atlantic Ocean, NC	–	NOS	–78.506670	33.865000
8661070 Springmaid Pier, Atlantic Ocean, SC	SmPr	NOS	–78.918330	33.655000
8721604 Trident Pier, Port Canaveral, FL	TPr	NOS	–80.593330	28.415000
8721608 Canaveral Harbor Entrance, FL	–	NOS	–80.601670	28.408330
8722670 Lake Worth Pier, Atlantic Ocean, FL	LWPr	NOS	–80.033330	26.611670
8723080 Haulover Pier, North Miami Beach, FL	–	NOS	–80.120000	25.903330
8723170 Miami Beach, City Pier, FL	–	NOS	–80.131670	25.768330
Permanent tower installation R6	R6	S00	–80.230000	31.530000
Permanent tower installation R2	R2	S00	–80.570000	31.380000
Temporary tower deployment Gray's Reef	GR	S00	–80.920000	31.360000
Temporary tower deployment R5	R5	S00	–80.770000	30.930000
Long Bay	LB	B04	–78.740000	33.690000
Onslow Bay at the 27-m isobath	OB27	B04	–77.300000	33.950000
Onslow Bay at the 63-m isobath	OB63	B04	–77.100000	33.400000
Savannah Navigational Light Tower	SNLT	B04	–80.680000	31.950000

Name	Abbr[a]	Source[b]	°W	°N
Tower D87	D87	B04	–80.550000	31.680000
Offshelf (6 stations)[e]				
422 Atlantic Ocean	I422	IHO	–75.616660	32.683330
41 Atlantic Ocean	I41	IHO	–76.416660	30.433330
360 Atlantic Ocean	I360	IHO	–76.800000	28.450000
355 Atlantic Ocean	I355	IHO	–76.783330	28.016660
9710441 Settlement Point, Grand Bahamas, Bahamas	SPGB	NOS	–78.996670	26.710000
315 Nassau, Bahamas	I315	IHO	–77.350000	25.083330

[a] Abbr stands for the station abbreviations used herein.

[b] Six sources provide tidal constituent data: National Ocean Service (NOS); St. Johns River Water Management District (SJRWMD); South Florida Water Management District (SFWMD); Seim (2000) (S00); Blanton et al. (2004) (B04); and International Hydrographic Organization (IHO) (website http://www.iho.shom.fr/ accessed on March 14, 2005).

[c] Estuary stations are landward of the uninterrupted coastline: the coastline that would be present in the absence of any tidal inlets.

[d] Shelf/coastal stations are seaward of the uninterrupted coastline but within the shelf break.

[e] Offshelf stations are seaward of the break.

Table 11.2. Water level amplitudes A (m) and phases ϕ (°) for 33 of the overall 103 gaging stations in the South Atlantic Bight (see Figure 11.1 and Table 11.1).

Station	M2		N2		S2		K1		O1		M4[a]		M6[a]		M8[a]	
	A	ϕ	A	ϕ	A	ϕ	A	ϕ	A	ϕ	A	ϕ	A	ϕ	A	ϕ
Estuary/tidal inlet (13 stations)[b]																
ChHr	0.783	10.4	0.172	354.9	0.119	36.1	0.105	199.7	0.079	203.4	0.033	209.6	0.006	135.3	0.000	0.0
FRPS	0.883	9.6	0.205	356.3	0.152	33.3	0.106	198.9	0.078	202.4	0.029	210.1	0.011	22.1	0.004	111.3
PUL	1.013	17.9	0.219	2.2	0.158	45.8	0.110	200.7	0.079	206.5	0.042	248.1	0.006	60.4	0.000	0.0
SIM	0.976	23.4	0.226	8.1	0.160	51.1	0.107	201.2	0.076	208.0	0.027	303.6	0.007	192.5	0.000	0.0
MAY	0.662	28.1	0.149	10.1	0.111	51.5	0.082	203.9	0.060	212.2	0.024	170.5	0.010	212.2	0.000	0.0
FUL	0.565	253.5	0.104	244.3	0.095	276.0	0.060	147.3	0.041	164.6	0.006	261.3	0.013	170.7	0.001	181.8
JAX	0.405	278.4	0.072	268.4	0.050	288.0	0.060	171.3	0.041	156.7	0.013	125.6	0.025	266.4	0.001	142.3
FtMz	0.554	259.5	0.109	226.5	0.105	290.8	0.070	140.2	0.072	152.0	0.032	24.2	0.021	57.3	0.000	0.0
SEB	0.045	286.2	0.009	265.4	0.004	313.4	0.011	181.8	0.011	187.2	0.005	133.6	0.002	227.3	0.000	261.7
FtP	0.207	256.7	0.048	236.3	0.028	275.2	0.049	166.1	0.040	180.2	0.010	295.9	0.005	123.9	0.000	185.3
LUC	0.288	239.0	0.063	224.6	0.035	255.4	0.060	159.0	0.045	170.3	0.014	238.7	0.009	109.4	0.001	254.4
CGD	0.318	248.7	0.069	233.4	0.046	274.3	0.060	161.2	0.049	172.3	0.003	40.8	0.005	26.1	0.001	30.2
BIS	0.298	41.0	0.066	21.5	0.052	71.3	0.031	263.2	0.028	288.4	0.007	69.5	0.011	169.4	0.000	0.0
Continental shelf (14 stations)[c]																
R6	0.680	1.5	0.170	339.7	0.130	28.0	0.100	190.9	0.070	198.0	–	–	–	–	–	–

Station	M2		N2		S2		K1		O1		M4[a]		M6[a]		M8[a]	
	A	ϕ	*A*	ϕ	*A*	ϕ	*A*	ϕ	*A*	ϕ	*A*	ϕ	*A*	ϕ	*A*	ϕ
R2	0.760	7.2	0.180	345.2	0.130	29.0	0.100	193.6	0.080	199.7	–	–	–	–	–	–
GR	0.880	9.5	0.190	344.9	0.150	29.1	0.110	189.2	0.070	199.4	–	–	–	–	–	–
R5	0.760	8.0	0.170	341.7	0.130	26.8	0.110	190.2	0.070	196.3	–	–	–	–	–	–
LB	0.730	358.6	0.150	344.0	0.120	15.0	0.120	186.8	0.070	199.5	–	–	–	–	–	–
OB27	0.550	353.3	0.140	335.8	0.100	17.0	0.090	184.1	0.070	189.3	–	–	–	–	–	–
OB63	0.460	352.6	0.120	320.4	0.070	27.6	0.090	201.1	0.070	188.4	–	–	–	–	–	–
SNLT	0.890	6.3	0.200	2.4	0.200	19.3	0.100	195.3	0.070	194.9	–	–	–	–	–	–
D87	0.830	4.9	0.160	341.1	0.180	13.0	0.100	193.3	0.070	196.7	–	–	–	–	–	–
SmPr	0.741	357.6	0.178	338.4	0.126	18.6	0.100	188.8	0.073	192.9	0.006	262.8	0.003	317.7	0.000	0.0
StM	0.850	231.3	0.187	211.8	0.132	247.5	0.103	117.6	0.076	135.7	0.009	61.5	0.004	52.3	0.001	114.3
StA	0.662	229.4	0.163	212.7	0.112	245.7	0.101	121.8	0.073	132.7	0.013	119.0	0.006	6.7	0.004	98.8
TPr	0.514	222.3	0.122	203.2	0.080	237.0	0.099	124.7	0.076	136.8	0.004	203.3	0.008	232.4	0.002	148.7
LWPr	0.419	13.4	0.098	354.1	0.072	38.2	0.059	219.6	0.046	235.7	0.000	0.0	0.000	0.0	0.000	0.0
Offshelf (6 stations)[d]																
I422	0.487	353.0	0.113	328.0	0.087	26.0	0.103	184.0	0.080	190.0	0.000	0.0	0.000	0.0	0.000	0.0
I41	0.441	358.0	0.108	336.0	0.083	23.0	0.097	190.0	0.074	194.0	0.000	0.0	0.000	0.0	0.000	0.0
I360	0.411	2.0	0.101	344.0	0.071	32.0	0.091	195.0	0.069	196.0	0.000	0.0	0.000	0.0	0.000	0.0
I355	0.402	9.0	0.096	352.0	0.070	41.0	0.089	196.0	0.071	202.0	0.000	0.0	0.000	0.0	0.000	0.0
SPGB	0.405	10.6	0.093	349.8	0.070	36.6	0.067	197.1	0.046	199.2	0.000	0.0	0.000	0.0	0.000	0.0

Station	M2		N2		S2		K1		O1		M4[a]		M6[a]		M8[a]	
	A	ϕ	A	ϕ	A	ϕ	A	ϕ	A	ϕ	A	ϕ	A	ϕ	A	ϕ
I315	0.379	7.7	0.092	345.7	0.064	31.7	0.087	197.3	0.065	201.3	0.000	0.0	0.000	0.0	0.000	0.0

[a] Seim (2000) (S00) and Blanton et al. (2004) (B04) do not report for the M4, M6, and M8 overtides.

[b] Estuary stations are landward of the uninterrupted coastline: the coastline that would be present in the absence of any tidal inlets.

[c] Shelf/coastal stations are seaward of the uninterrupted coastline but within the shelf break.

[d] Offshelf stations are seaward of the break.

Table 11.3. Tidal ellipse parameters for the M2 and K1 tidal constituents at the six shelf/coastal stations R6, R2, GR, R5, LB, and OB27 in the South Atlantic Bight (see Figure 11.1 and Table 11.1). OBS stands for observation; M, A, I, and C stand for the MARSH, AICWW, INLET, and COASTAL mesh results, respectively.

Station	Semi-major axis (m/s)					Semi-minor axis (m/s)					Inclination (CCW from east)					Phase (GMT)				
	OBS	M	A	I	C	OBS	M	A	I	C	OBS	M	A	I	C	OBS	M	A	I	C
M2 (semi-diurnal) frequency																				
R6	0.289	0.298	0.313	0.312	0.258	–0.105	–0.095	–0.098	–0.098	–0.091	149.2	155.7	155.6	155.6	156.7	278.5	273.3	271.6	271.0	266.3
R2	0.312	0.307	0.326	0.325	0.266	–0.105	–0.088	–0.091	–0.090	–0.081	146.5	155.6	155.3	155.4	157.0	287.0	279.0	277.2	276.5	270.8
GR	0.249	0.249	0.271	0.269	0.213	–0.067	–0.048	–0.050	–0.049	–0.036	148.5	157.2	156.2	156.2	158.8	285.6	284.7	281.6	280.7	273.0
R5	0.297	0.292	0.310	0.310	0.258	–0.092	–0.079	–0.081	–0.080	–0.073	144.5	155.5	155.1	155.2	156.6	289.6	285.2	283.6	283.0	277.7
LB	0.071	0.070	0.069	0.069	0.068	0.014	0.014	0.013	0.013	0.015	138.2	139.8	139.6	140.0	139.0	272.6	267.7	267.2	267.2	267.0
OB27	0.116	0.139	0.139	0.137	0.136	–0.058	–0.066	–0.066	–0.066	–0.065	119.0	139.7	139.6	139.9	139.7	261.4	254.9	254.8	254.4	254.3
K1 (diurnal) frequency																				
R6	0.022	0.020	0.020	0.020	0.018	–0.010	–0.011	–0.011	–0.010	–0.010	121.5	144.3	143.7	143.9	146.1	115.8	114.6	110.3	109.9	106.4
R2	0.020	0.016	0.016	0.016	0.014	–0.013	–0.007	–0.006	–0.006	–0.005	26.0	148.7	147.4	147.8	151.3	235.8	118.6	111.3	110.6	105.3
GR	0.020	0.016	0.016	0.016	0.014	–0.013	–0.007	–0.006	–0.006	–0.005	26.0	148.7	147.4	147.8	151.3	235.8	118.6	111.3	110.6	105.3
R5	0.012	0.020	0.020	0.020	0.018	–0.004	–0.010	–0.010	–0.010	–0.009	175.1	146.6	146.6	146.7	148.3	96.4	120.1	115.4	115.0	111.9
LB	0.009	0.006	0.006	0.006	0.006	0.003	0.002	0.002	0.002	0.002	162.4	145.6	145.1	146.1	147.6	124.0	105.1	105.0	105.5	106.7
OB27	0.011	0.013	0.013	0.012	0.012	–0.007	–0.008	–0.008	–0.008	–0.008	70.7	116.5	116.6	116.8	117.3	132.3	100.4	100.4	100.1	99.5

Table 11.4. Semi-major axes and phase angles for the M2, N2, S2, K1, and O1 tidal constituents at the three estuary stations MAY, FUL, and JAX in the Lower St. Johns River (see Figure 11.1 and Table 11.1). OBS stands for observation; M, A, I, and C stand for the MARSH, AICWW, INLET, and COASTAL mesh results, respectively. Note the COASTAL mesh cannot produce a result at the estuary stations.

Constituent	Semi-major axis (m/s)					Phase (GMT)				
	OBS	M	A	I	C	OBS	M	A	I	C
M2 (semi-diurnal) frequency										
MAY	1.017	1.019	0.961	0.954	–	12.0	14.0	0.4	0.3	–
FUL	0.797	0.797	0.898	0.905	–	34.0	22.9	16.1	15.0	–
JAX	0.653	0.610	0.718	0.722	–	76.7	60.5	57.3	56.2	–
N2 (semi-diurnal) frequency										
MAY	0.213	0.192	0.170	0.169	–	23.7	23.1	10.8	10.6	–
FUL	0.130	0.141	0.160	0.162	–	53.0	34.8	29.1	28.1	–
JAX	0.097	0.105	0.122	0.123	–	100.3	72.1	69.8	68.9	–
S2 (semi-diurnal) frequency										
MAY	0.137	0.223	0.197	0.195	–	345.0	1.1	346.5	346.0	–
FUL	0.093	0.165	0.182	0.183	–	17.0	32.4	23.2	22.9	–
JAX	0.067	0.120	0.137	0.138	–	65.7	69.6	65.8	64.5	–

Constituent	Semi-major axis (m/s)					Phase (GMT)				
	OBS	M	A	I	C	OBS	M	A	I	C
K1 (diurnal) frequency										
MAY	0.130	0.112	0.090	0.090	–	141.7	198.8	188.9	189.5	–
FUL	0.080	0.086	0.086	0.087	–	206.7	200.2	196.5	196.0	–
JAX	0.067	0.068	0.071	0.071	–	231.7	219.9	220.1	219.6	–
O1 (diurnal) frequency										
MAY	0.097	0.079	0.067	0.068	–	179.7	204.6	198.9	199.6	–
FUL	0.053	0.062	0.061	0.061	–	211.7	206.1	206.7	206.3	–
JAX	0.050	0.045	0.045	0.045	–	234.0	225.7	229.2	228.9	–

11.2. Performance on Water Levels

Model/data comparisons are based on computed tides to observed tides. Tides are compared either by tidal constituents or by resynthesized tidal signals:

$$\zeta(t) = \sum_{N} A_n \cos(\omega_n t - \phi_n) \quad \ldots\ldots\ldots\

the stations: estuary; shelf/coastal; and offshelf. Error is minimal off the bight shelf and greatest in the estuaries. This is more evident when assessing in terms of the normalized RMS error. The normalizing factor used is the region-averaged M2 tidal amplitude. Tidal amplitudes are generally smaller in the estuaries, which in turn increases the error on a relative basis.

Off the bight shelf, the MARSH, AICWW, INLET, and COASTAL meshes perform virtually the same. In the estuaries and on the shelf and coast, mesh performance differs: the MARSH mesh outperforms all other mesh variants. Recall that the model results are uncalibrated. None of the models were calibrated so as to keep the effects of the different mesh representations isolated in the forthcoming analysis. The fact that the greatest differences between the solutions is at the estuary stations is intuitive. However, combining this with the fact that the solutions at the shelf/coastal stations are similarly sensitive and the solutions at the offshelf stations are unaffected supports the hypothesis that the estuarine features influence nearshore and shelf circulation.

Table 11.5. Root mean square (RMS) errors based on water level performance at the 103 gaging stations in the South Atlantic Bight. The errors are presented according to the geographical partitioning of the stations: estuary; shelf/coastal; and deep ocean. Note the COASTAL mesh cannot produce a result within the estuaries. The second error column is the RMS error normalized by the region-averaged M2 tidal amplitude.

Mesh	RMS (cm)	RMS (%)
Estuary (69 stations)[a]		
MARSH	9.2	6.2
AICWW	10.8	7.2
INLET	11.7	7.9
COASTAL	–	–
Shelf/coastal (28 stations)[b]		
MARSH	5.1	3.4
AICWW	6.1	4.0
INLET	6.1	4.0
COASTAL	7.4	4.8
Deep ocean (6 stations)[c]		
MARSH	4.3	2.5
AICWW	4.3	2.5
INLET	4.3	2.5
COASTAL	4.3	2.5

[a] Estuary stations are landward of the uninterrupted coastline: the coastline that would be present in the absence of any tidal inlets.

[b] Shelf/coastal stations are seaward of the uninterrupted coastline but within the shelf break.

[c] Deep ocean stations are seaward of the shelf break.

11.3. Performance on Tidal Velocities

Computed tidal velocities are decomposed into tidal ellipse parameters for comparison to those diagnosed from observations. Table 11.3 reports the semi-major and semi-minor axes, inclination, and phase for the M2 and K1 tidal constituents at the six shelf/coastal stations. There is good agreement overall between the model solutions and the observations; however, there are trends with respect to the performance of the various meshes. First, the COASTAL mesh far underpredicts the observed shelf velocities: by 10 – 20% on the M2 semi-major axis. The AICWW and INLET meshes have near identical performance but overpredict M2 velocities by about 5 – 10%. Also noted is the slightly better performance of the AICWW mesh relative to the INLET mesh. The MARSH mesh best replicates the observed shelf velocities: within 5% on the M2 semi-major axis. The MARSH mesh also produces the best solution in terms of phase: on average within 5° on the M2 tide.

The four stations located off Georgia's coast (R6, R2, GR, and R5) exhibit the most variability with respect to the different model solutions. Figure 11.2 displays M2 tidal ellipses diagnosed from the MARSH, AICWW, and COASTAL solutions relative to observations at these four shelf stations. Tidal ellipses are generally directed shoreward across bathymetric contours. The ellipses have an eccentricity equal to about three: the semi-major axes are about three times the semi-minor axes. Velocity phase corresponds to the velocity at time $t = 0$. All velocity phases are directed along-shelf poleward.

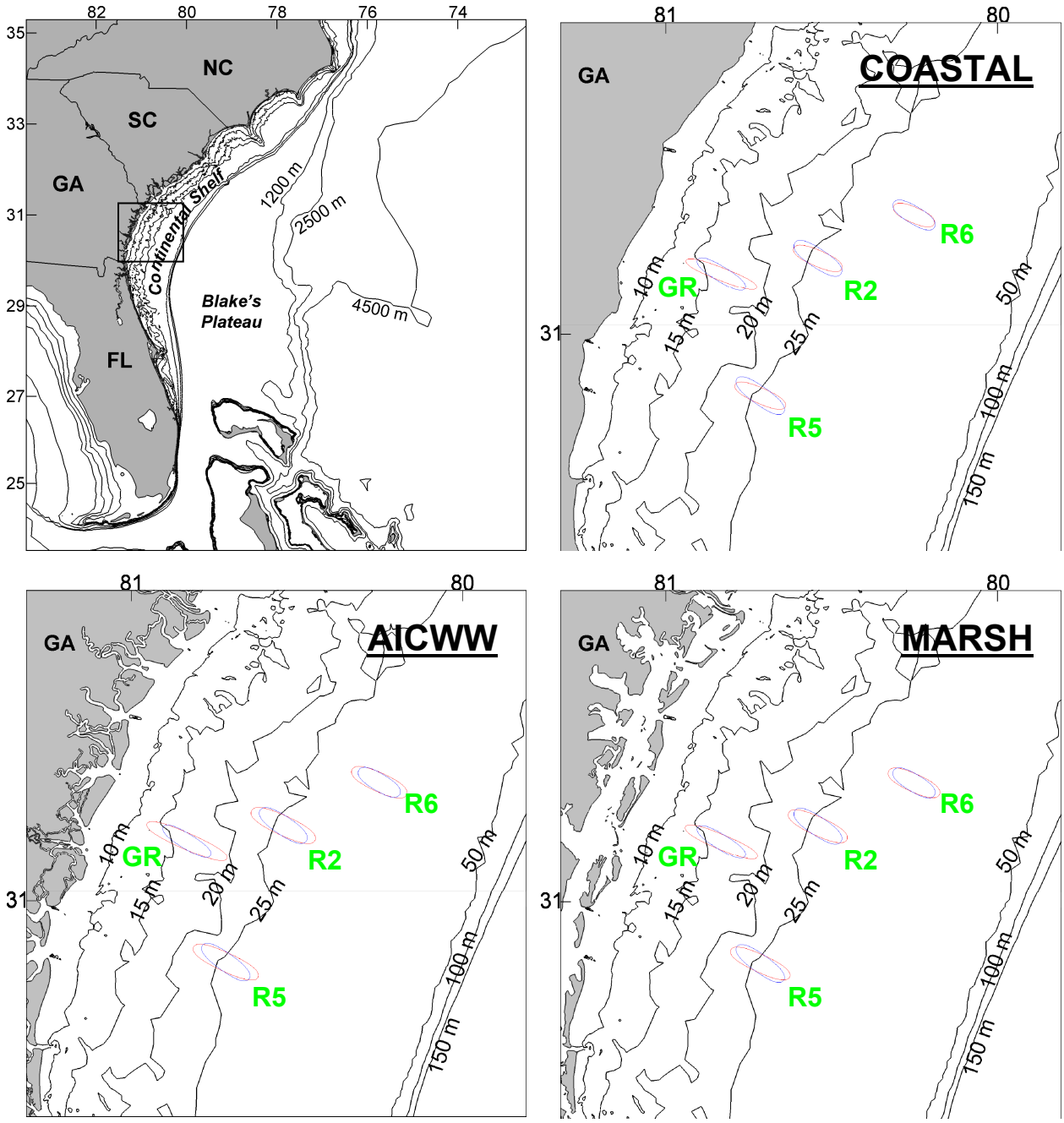

Figure 11.2. M2 tidal ellipses diagnosed from the COASTAL, AICWW, and MARSH solutions (red) relative to observations (blue) at the four shelf stations R6, R2, GR, and R5 (see Figure 11.1 and Table 11.1).

The COASTAL ellipses are narrower than the observations and are oriented slightly counterclockwise (Figure 11.2). The AICWW ellipses show improvement in terms of their shape and orientation: they are more circular and at inclinations closer with the observations. The MARSH ellipses also capture this improvement in addition to best replicating the overall size. The graphical features to the tidal ellipses are quantified in Table 11.3: size and shape are dictated by the semi-major and semi-minor axes; orientation by inclination; and velocity phase. At these four shelf stations, the MARSH mesh produces the best solution of all meshes in terms of the semi-major axis and phase. These two ellipse parameters are important to shelf tidal dynamics as they relate to the speed of the cross-shelf velocity and the timing of the peak velocity, respectively. In addition, these two parameters show the most sensitivity between the different mesh applications: the implication is that the geometric representation of the estuaries plays a substantial role in accurately capturing peak velocity and its timing.

The three estuary stations show interesting trends with regard to the different mesh results (Table 11.4). In order of increasing mesh performance: INLET; AICWW; and MARSH. At station MAY, the M2 semi-major axis is increased by 1% by the addition of the Atlantic Intracoastal Waterway (AICWW versus INLET) and is increased by 15% by the addition of the Atlantic Intracoastal Waterway and intertidal zones (MARSH versus AICWW). The opposite occurs with stations FUL and JAX: the M2 semi-major axis is decreased by 1% by the addition of the Atlantic Intracoastal Waterway (AICWW versus INLET) and is decreased by 12 – 15% by the addition of the Atlantic Intracoastal Waterway and intertidal zones (MARSH versus AICWW). Phasing is best with the MARSH mesh: timing is improved against the AICWW and INLET meshes by 30, 10, and 6 minutes at stations MAY, FUL, and JAX, respectively. The waterway and intertidal features influence the downstream station differently than they influence

the two upstream stations: circulation is enhanced in the downstream and reduced in the upstream.

11.4. Cross-sectional Flows

Cross-sectional flows were measured over an M2 tidal cycle at three cross sections in the downstream region of the Lower St. Johns River (Figure 11.3): 1) Clapboard Creek; 2) the north entrance to the Atlantic Intracoastal Waterway; and 3) the south entrance to the Atlantic Intracoastal Waterway. The observations are of full cross-sectional flow: tides, inflows, meteorology, baroclinic effects, and other influences make up the observed data. Comparing model output to such observations should take into account that the model output represents tides only.

Figure 11.4 displays plots of observed and simulated flow for the three cross sections. The MARSH solution is shown to outperform the AICWW solution. The trend is greater flow volume with the MARSH solution. The cross sections are located near the intertidal zones, which explains the additional conveyance produced by the MARSH mesh. Furthermore, the larger flows produced by the MARSH mesh matches the trend observed with tidal velocities at station MAY (located also in the downstream region): increased velocities with the MARSH mesh (Table 11.4).

The MARSH mesh describes about 60 km^2 of intertidal zones locally: roughly the intertidal region shown in the graphic of Figure 11.3. At high tide, the local intertidal zone holds 0.052 km^3 of storage. The river channel and tidal creeks of the lower 15 km of the Lower St. Johns River hold about 0.164 km^3 of water during low tide. Locally, the intertidal zones provide

an appreciable capacity with respect to tidal storage which acts to substantially redistribute water in the downstream region of the Lower St. Johns River. Only the MARSH mesh is able to account for the hydrodynamic interaction between the river channels and intertidal zones.

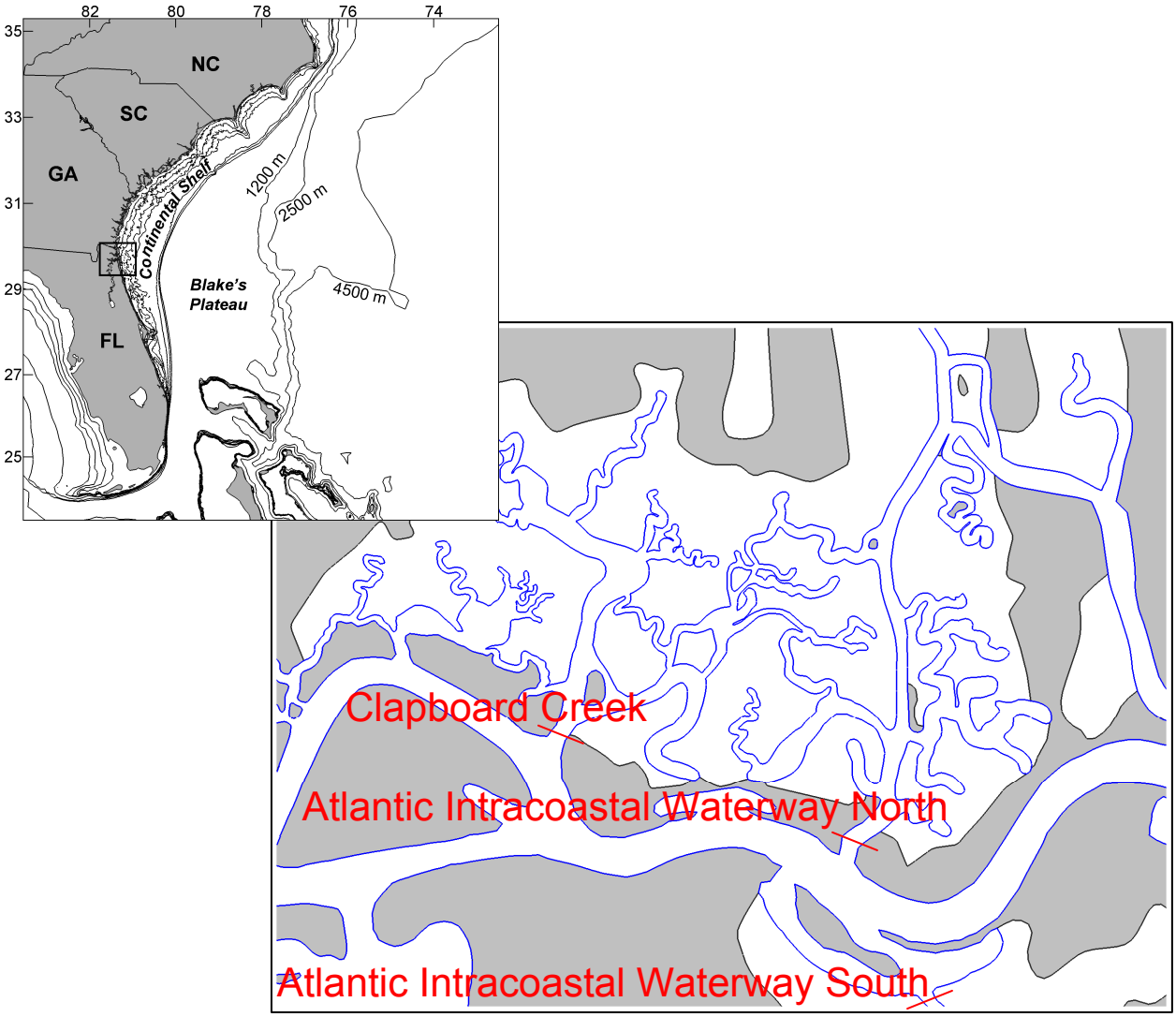

Figure 11.3. Three cross sections in the Lower St. Johns River where flow was measured over an M2 tidal cycle: 1) Clapboard Creek; 2) the north entrance to the Atlantic Intracoastal Waterway; and 3) the south entrance to the Atlantic Intracoastal Waterway. The black outline is the boundary of the MARSH mesh and the blue outline is the boundary of the AICWW mesh.

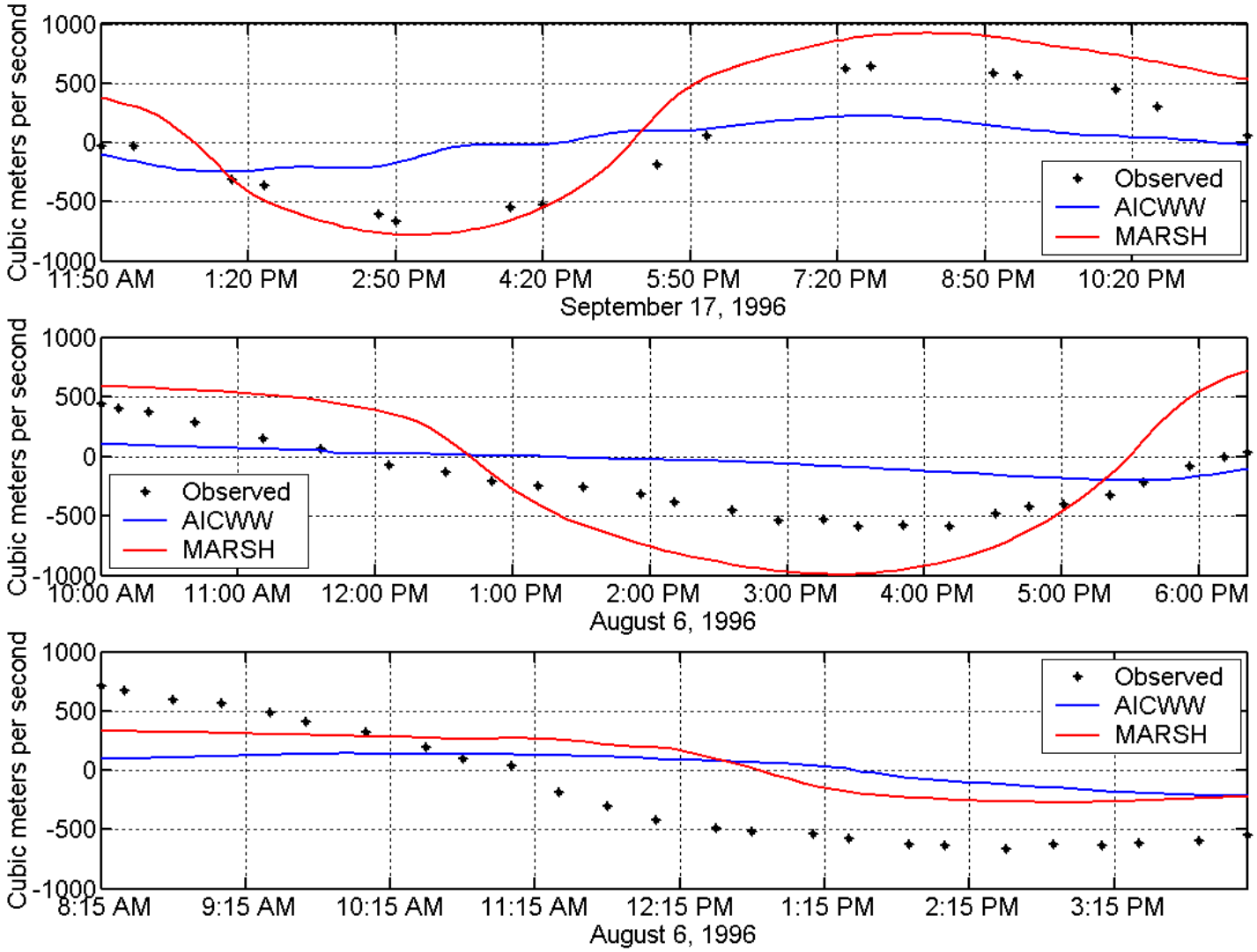

Figure 11.4. Plots of observed and simulated flow for the three cross sections in the Lower St. Johns River: Clapboard Creek and the north and south entrances to the Atlantic Intracoastal Waterway.

11.5. Summary and Discussion

This chapter validated the models distinguished by four alternate meshes (COASTAL, INLET, AICWW, and MARSH) in terms of simulating tidal hydrodynamics in the South Atlantic Bight. The MARSH mesh was shown to best replicate observed tides in the domain. Second in performance was the AICWW mesh. The improvement gained in the AICWW and MARSH solutions is attributed directly to including the estuarine details in each of the meshes. Velocities were shown to be far more sensitive than water levels with respect to the inclusion of the estuaries in the mesh.

Off the bight shelf, all four meshes performed virtually the same. Elsewhere, there were differences in the water level and velocity solutions. RMS errors between simulated and observed tidal elevations were greater with: 1) closer proximity to the coast; and 2) less estuarine definition in the mesh. Adding the estuary waterbodies led to increased velocities on the shelf: by over 20% on the M2 constituent. The estuary waterbodies alone in the mesh, however, led to an overprediction in the M2 shelf velocity. Incorporating the intertidal zones led to a less substantial increase in the velocity and the best replication of the shelf observations.

Local solutions are dependent on the extent and comprehensiveness of the intertidal zones described in the estuaries as shown in the final section on cross-sectional flows. While the local impacts are intuitive, the level of variability in the solutions over the shelf is interesting and warrants further analysis, which will be explored in the following chapter. While the estuaries are marginal features with regard to the volume of the entire South Atlantic Bight, this chapter has demonstrated them to be physically relevant in the overall hydrodynamics.

CHAPTER 12. ANALYSIS

12.1. Water Levels and Velocities

This section analyzes the water level and velocity solutions from the COASTAL, AICWW, and MARSH mesh applications with respect to where and why there exist differences in the simulated hydrodynamics. Since the INLET and AICWW solutions are so similar, it is decided to limit the analysis to AICWW solutions. AICWW is selected since the domain representation is more complete and because the solution outperforms (albeit only slightly) that of INLET. Further discussion regarding the AICWW versus INLET solutions is given in the next section.

The general notion here is to use the discrete results from the different model representations of the domain in order to better understand the continuum physics of the system. The AICWW solution will be compared to the COASTAL solution for the purpose of isolating the effect of incorporating the inlets and estuary waterbodies into the mesh. The major components to consider in this comparison will be: 1) the increased shallow water environment caused by the inlets and estuary waterbodies; 2) the variable width of the bight shelf; and 3) the stronger oceanic tide in the north of the domain relative to the south. The MARSH solution will be compared to the AICWW solution for the purpose of isolating the effect of incorporating the intertidal zones. The major component to consider in this comparison will be the intertidal zones.

Comparisons in this section are based on relative differences between the different solutions: the reader is referred to the previous chapter for absolute values of the solutions. The discussion precedes the related graphics which are split into two categories: 1) Figures 12.1

through 12.8 present global contour plots of solution differences; and 2) Figure 12.9 presents a cross-shelf transect and three along-shelf arcs for the South Atlantic Bight and Figures 12.10 through 12.14 present the solution differences interpolated to the transect and arcs. The global contour plots are meant to provide a domain-wide view into the solution differences and the transect and arcs are used to hone in on the cross-shelf and along-shelf variations in the solutions.

Figures 12.1 and 12.2 display contours of water level amplitude ratios: AICWW divided by COASTAL; and MARSH divided by AICWW, respectively. For both comparisons, the amplitude ratio is equal to one in the deep ocean and in the latitudinal extremes of the bight shelf. This implies that water level amplitudes in the deep ocean and in the latitudinal extremes of the domain are unaffected by the estuaries. Emanating from the Georgia/South Carolina border is an amplification effect (ratios greater than one) over the adjacent shelf (AICWW vs. COASTAL). In the MARSH to AICWW comparison, the opposite occurs: water level amplitudes are attenuated (ratios less than one) along the northeastern Florida, Georgia, and southern South Carolina coasts. This implies that the inlets and estuary waterbodies amplify tidal elevations on the shelf and at the coast whereas the intertidal zones act to attenuate them.

Figures 12.3 and 12.4 display contours of water level phase differences: AICWW minus COASTAL; and MARSH minus AICWW, respectively. As was the case with amplitudes, water level phases in the deep ocean and in the latitudinal extremes of the bight shelf are unaffected by the estuaries. Water level phases are delayed by the inlets and estuary waterbodies by as much as 7° (AICWW vs. COASTAL) and by the intertidal zones by as much as 1° (MARSH vs. AICWW). The water level phase difference exhibits similar spatial character as the amplitude ratio: estuarine influence over the shelf increases with closer proximity to the estuaries and is greater where the shelf is wider (off Georgia's coast and into Florida and South Carolina).

Figures 12.5 and 12.6 display contours of semi-major axis ratios: AICWW divided by COASTAL; and MARSH divided by AICWW, respectively. The following trends with velocities are the same as with water levels: 1) the deep ocean and the latitudinal extremes of the bight shelf are not influenced by the estuaries; 2) the effect of the inlets and estuary waterbodies is to amplify the shelf tides and the effect of the intertidal zones is to attenuate them; 3) the inlets and estuary waterbodies in addition to the intertidal zones cause a phase lag in the shelf tide; and 4) the estuarine influence is greater closer to the estuaries and where the shelf is wider. There is one major difference: velocities are far more sensitive than water levels with respect to being influenced by the estuaries. Semi-major axes are greater by as much as 50% between the AICWW and COASTAL solutions. Semi-major axes are less by as much as 10% between the MARSH and AICWW solutions. This follows what was observed in the model validation where incorporating the inlets and estuary waterbodies alone into the mesh caused for an overprediction of the shelf velocity and incorporating the intertidal zones caused for a less substantial increase leading to a better fit with observations. Furthermore, the spatial extent of the estuarine influence on shelf velocities is expanded outward relative to that seen with the elevation analysis.

Figures 12.7 and 12.8 display contours of velocity phase differences: AICWW minus COASTAL; and MARSH minus AICWW, respectively. Velocity phases are delayed by up to 9° by the inlets and estuary waterbodies (AICWW vs. COASTAL) and by up to 4° by the intertidal zones (MARSH vs. AICWW). Phase lags are spread out but generally follow the above trends.

The solution ratios and differences are interpolated to a cross-shelf transect and three along-shelf arcs defined in the South Atlantic Bight (Figure 12.9). The cross-shelf transect extends from the Georgia/South Carolina border to the 150-m isobath. The transect is positioned over the widest part of the bight shelf: 135 km. The three along-shelf arcs follow the 10-, 25-,

and 50-m isobaths from the southernmost limit of the bight shelf to its northernmost limit in the model domain: a distance of 1400 km. Points are spaced on the transect and arcs every 1 km.

Figure 12.10 displays solution ratios and differences interpolated to the cross-shelf transect. The first observation is that there is greater solution variability with closer proximity to the coast. This is the case for all solution measures. At the shelf break, the estuarine influence is relatively minor. Over the shelf width, the estuarine influence grows to a maximum at the coast. The second observation is that there is far greater sensitivity in the velocity solution relative to elevations: as much as five times the effect.

Figures 12.11 through 12.14 display solution ratios and differences interpolated to the along-shelf arcs. The top panel in each figure is given a blue textured box to indicate the portion of coastline $700\,\text{km} \le x \le 1000\,\text{km}$ that contains the "central" inlets (see Table 3.2, Figure 3.2, and related text). Recall that the "central" inlets are wider (3 km average width versus 600 m for the "north and south" inlets) and denser (spaced on average every 15 km versus 25 km for the "north and south" inlets) along this stretch of coast. The bottom panel in each figure is given a green textured box to indicate the portion of coastline $500\,\text{km} \le x \le 1100\,\text{km}$ that contains the intertidal zones. On the top panel of each figure there is also a double-pointed bolded arrow. The hash mark over the arrow at $x = 725\,\text{km}$ indicates where the shelf width is 125 km. North of this the shelf is consistently wider than 125 km. South of this the shelf gradually narrows to its minimum width off Florida's southeastern coast. Some of the figures contain smaller arrows that are labeled according to the nearly inlet or bay entrance.

In Figures 12.11 through 12.14, the following common themes are observed: 1) greater solution variability with closer proximity to the coast for all solution measures; and 2) upwards of five times the sensitivity with velocities relative to elevations. There is also correlation

between the along-shelf solution variability and the spatial character of the physical system. Water level amplitudes (Figure 12.11) and semi-major axes (Figure 12.13) are analyzed first. Water level phases (Figure 12.12) and velocity phases (Figure 12.14) are analyzed second.

Water levels and velocities are amplified mostly in the region where the coastal inlets are most densely clustered: $700\,\text{km} \le x \le 1000\,\text{km}$ (Figures 12.11 and 12.13, top). There is little to no amplification south of $x = 700\,\text{km}$: outside of the region of dense inlets and where the shelf is narrow. The labeled arrows indicate local effects where an inlet or bay entrance is causing direct influence. Local effects are noticeable all along the coast including outside the intertidal zone region: $x < 500\,\text{km}$ and $x > 1100\,\text{km}$. Note that inlets and bay entrances without surrounding marshes impact locally just as those with surrounding marshes. The consistent amplification north of $x = 700\,\text{km}$ is explained in terms of the wider shelf and greater oceanic tides in the northern part of the region. Water levels and velocities are attenuated mostly in the region of the intertidal zones: $500\,\text{km} \le x \le 1100\,\text{km}$ (Figures 12.11 and 12.13, bottom). Outside of the intertidal zone region there is little to no attenuation: $x < 500\,\text{km}$ and $x > 1100\,\text{km}$. The marsh region is the main attenuation factor and local effects are not noticeable in this comparison.

Phase lags caused by the inlets and estuary waterbodies (AICWW vs. COASTAL) and the intertidal zones (MARSH vs. AICWW) are more spread out than the water level and semi-major axis ratios but generally follow the above trends (Figures 12.12 and 12.14). It also needs to be noted that the phase lags overall are not that substantial (on the order of degrees) when compared to the ratios of water level amplitudes (on the order of percentage points) and semi-major axes (on the order of tens of percentage points), which is the purpose for not placing as much emphasis here on phase as was on magnitudes.

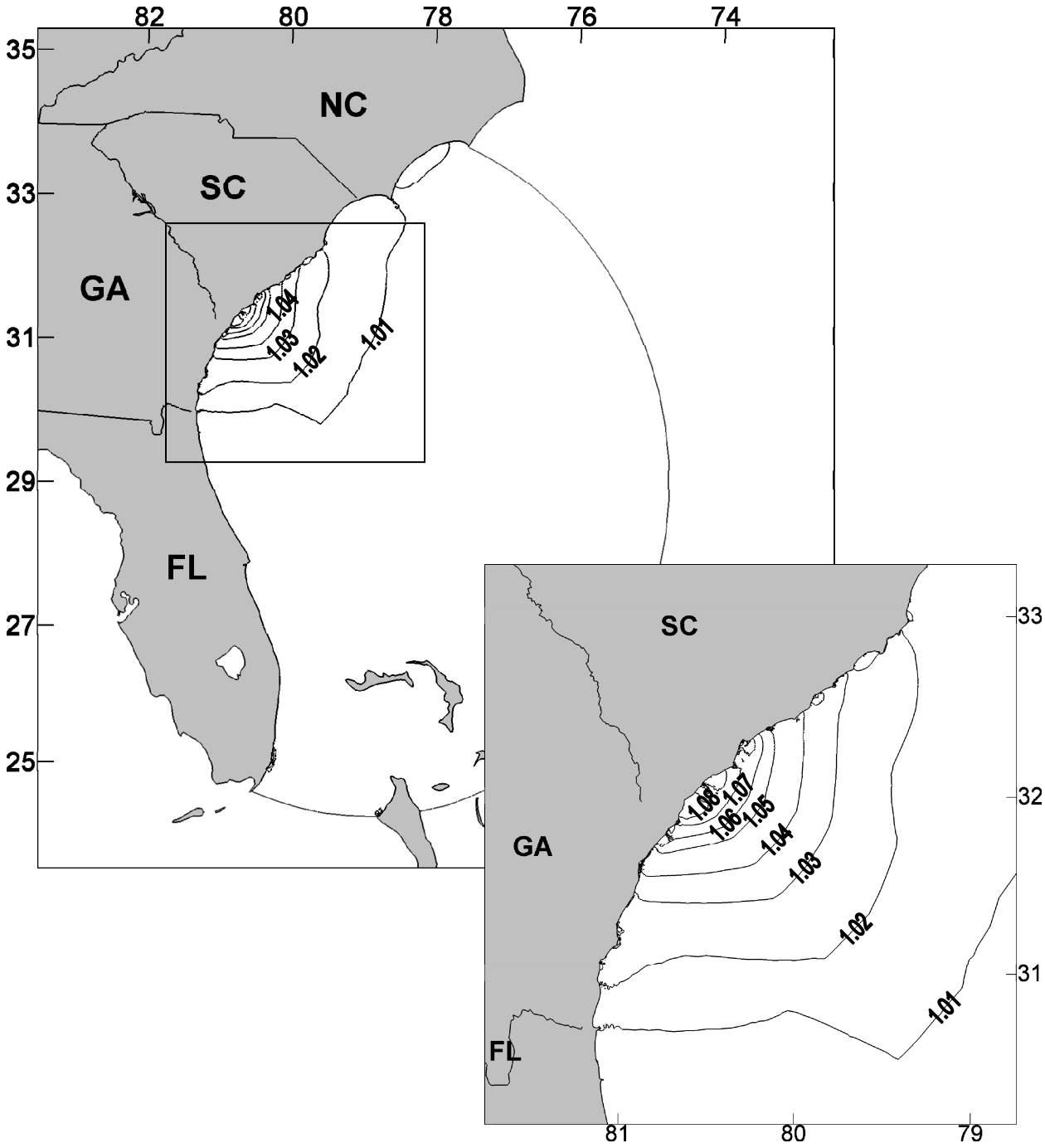

Figure 12.1. Contours of water level amplitude ratios: AICWW divided by COASTAL. The inset follows from the box in the larger view.

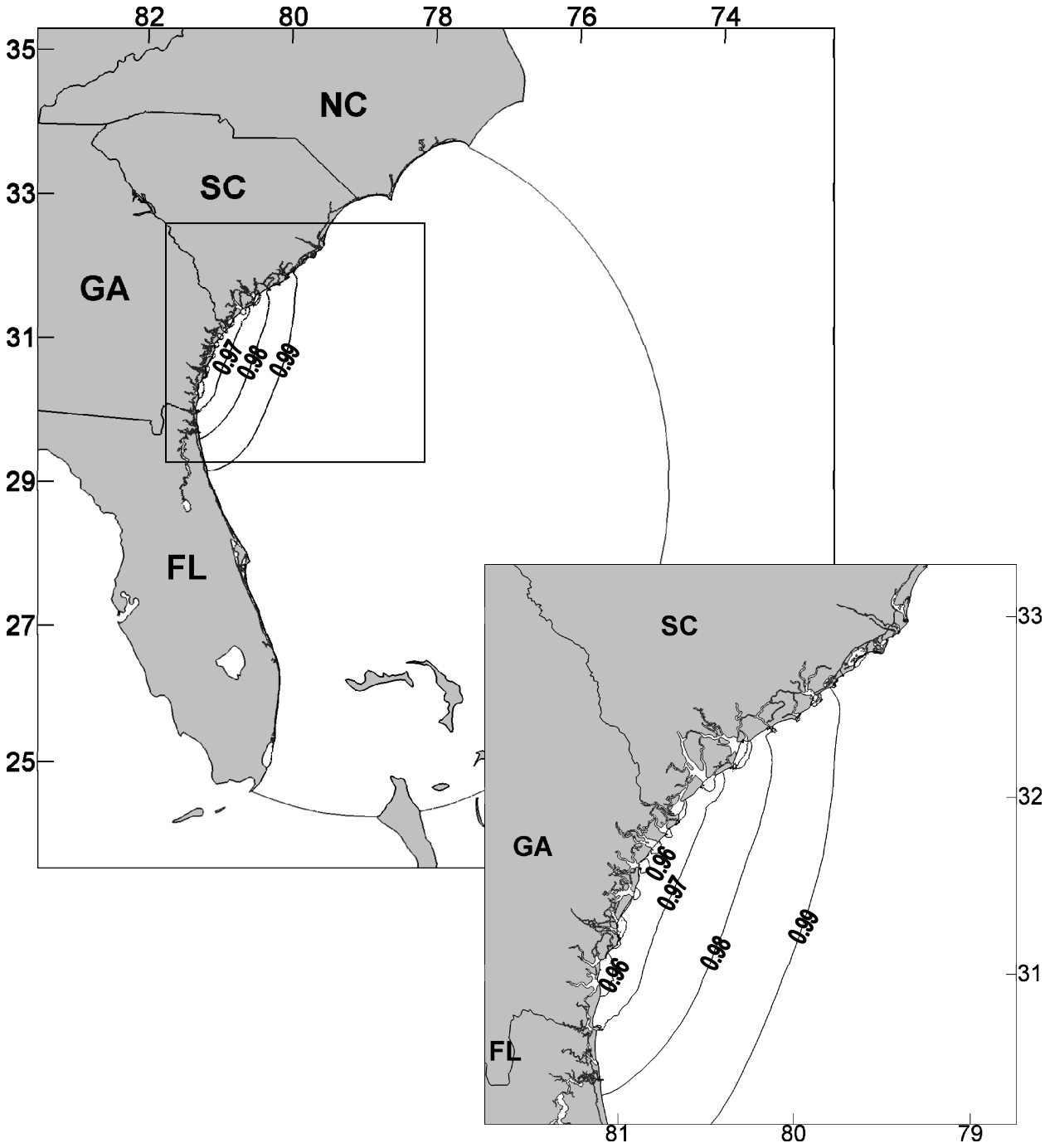

Figure 12.2. Contours of water level amplitude ratios: MARSH divided by AICWW. The inset follows from the box in the larger view.

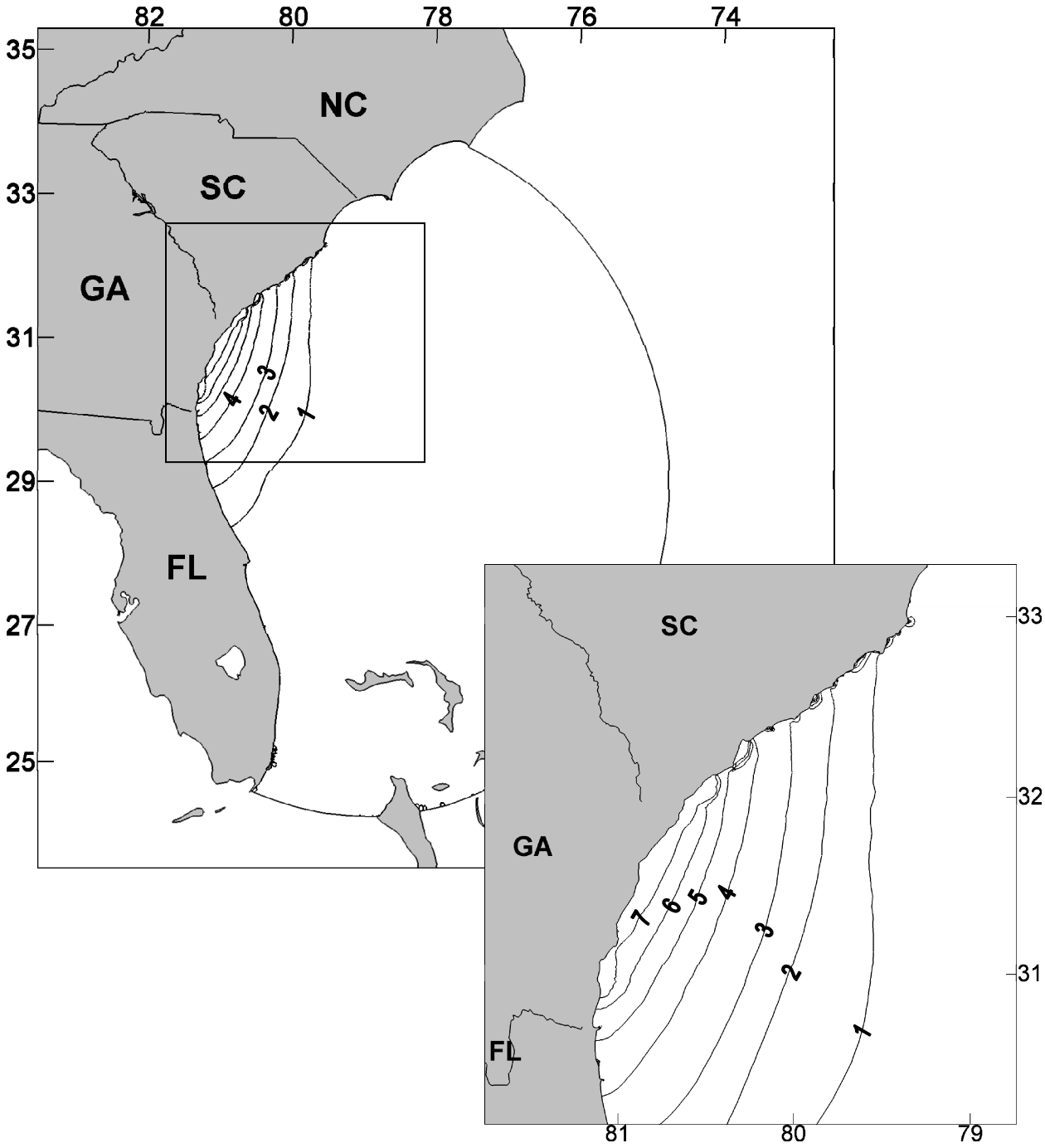

Figure 12.3. Contours of water level phase differences (°): AICWW minus COASTAL. The inset follows from the box in the larger view.

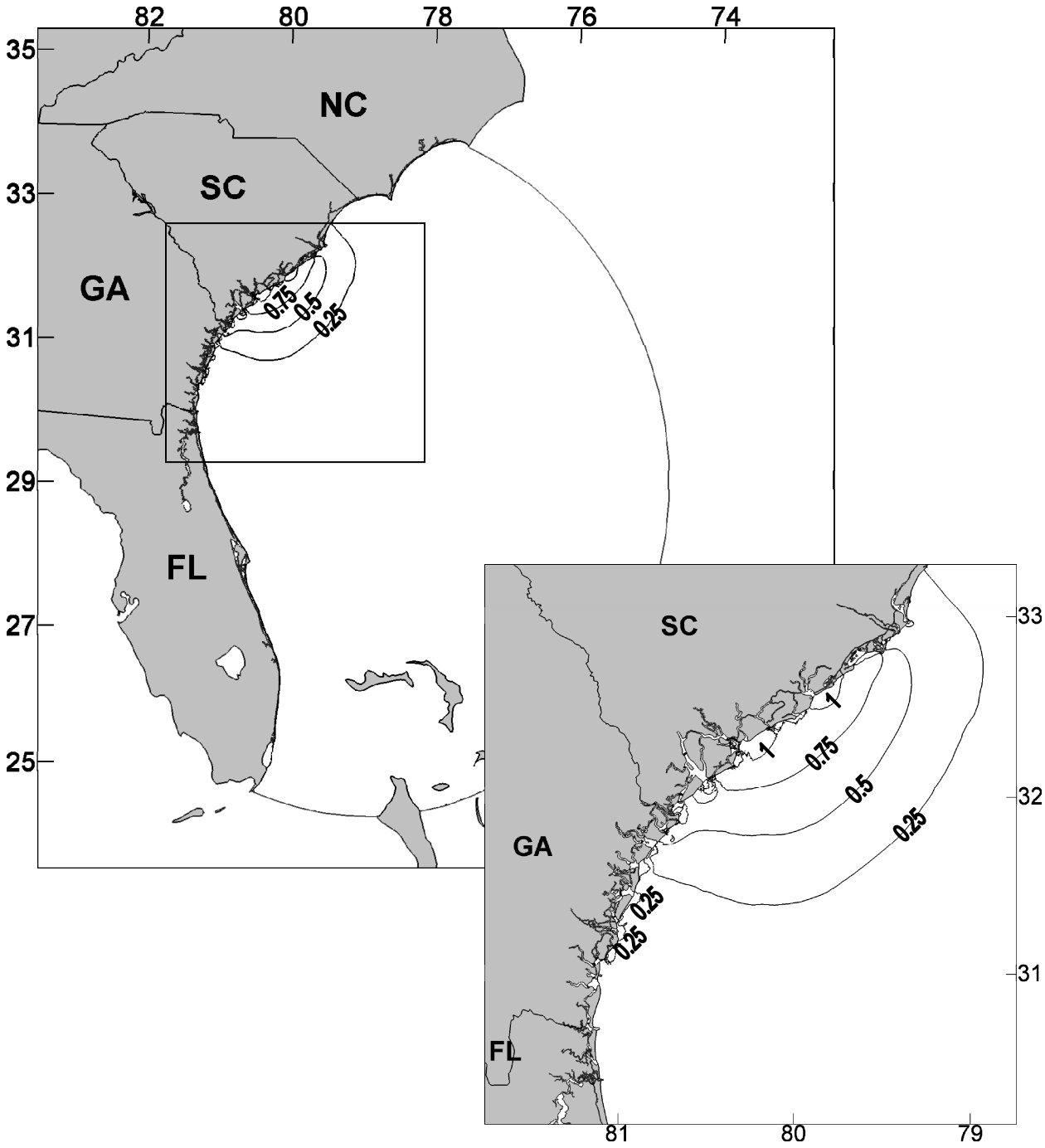

Figure 12.4. Contours of water level phase differences (°): MARSH minus AICWW. The inset follows from the box in the larger view.

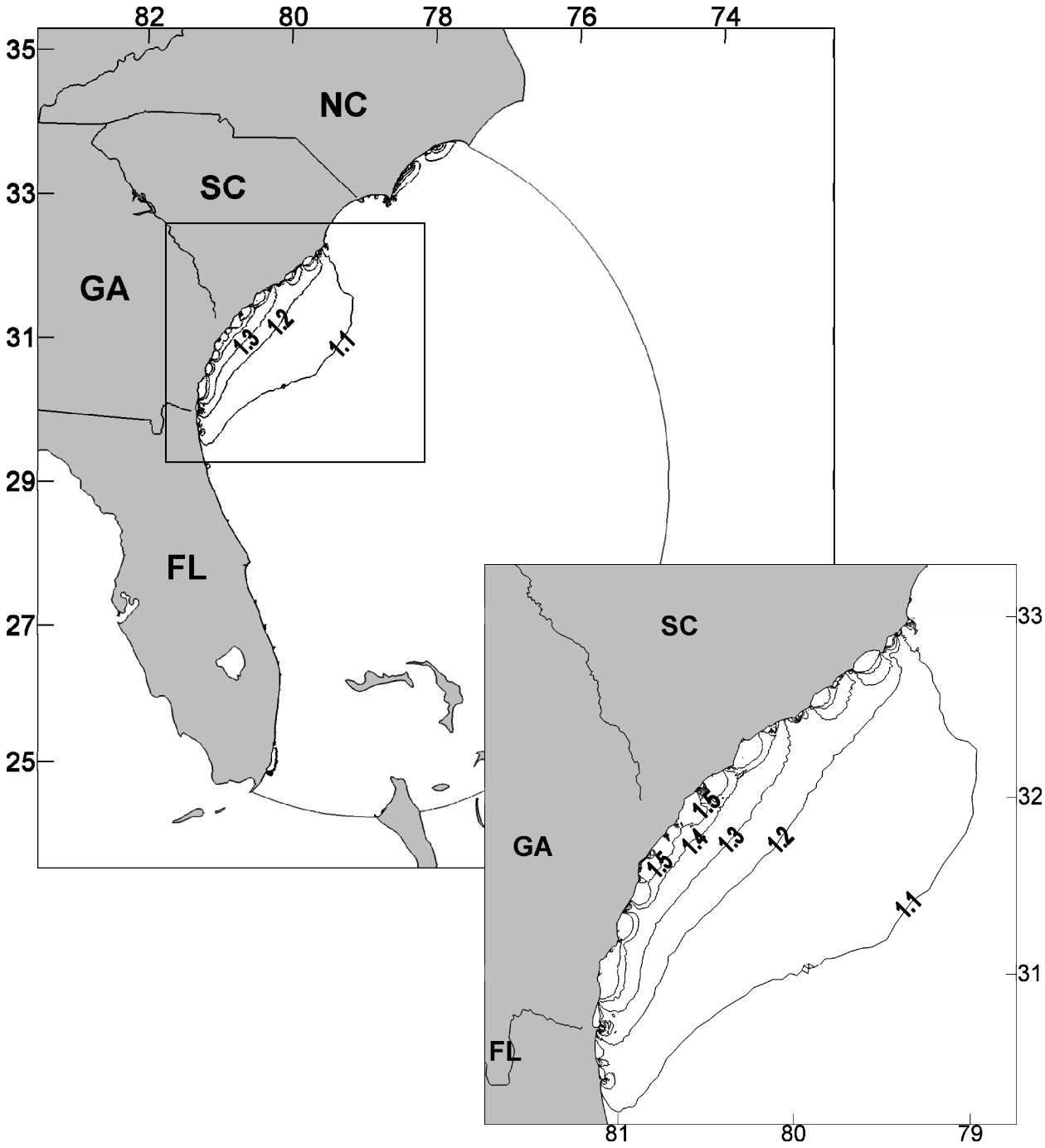

Figure 12.5. Contours of semi-major axis ratios: AICWW divided by COASTAL. The inset follows from the box in the larger view.

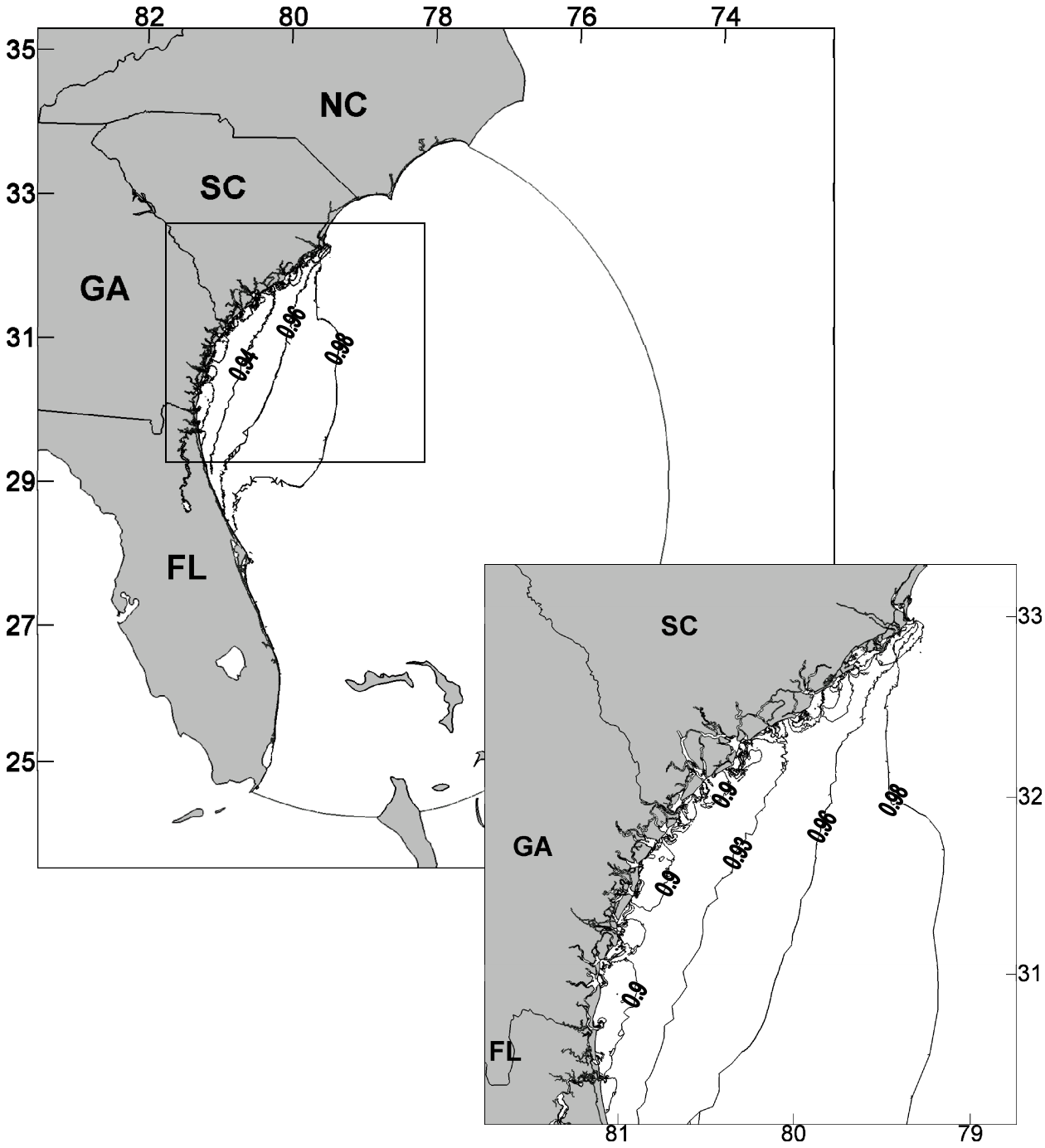

Figure 12.6. Contours of semi-major axis ratios: MARSH divided by AICWW. The inset follows from the box in the larger view.

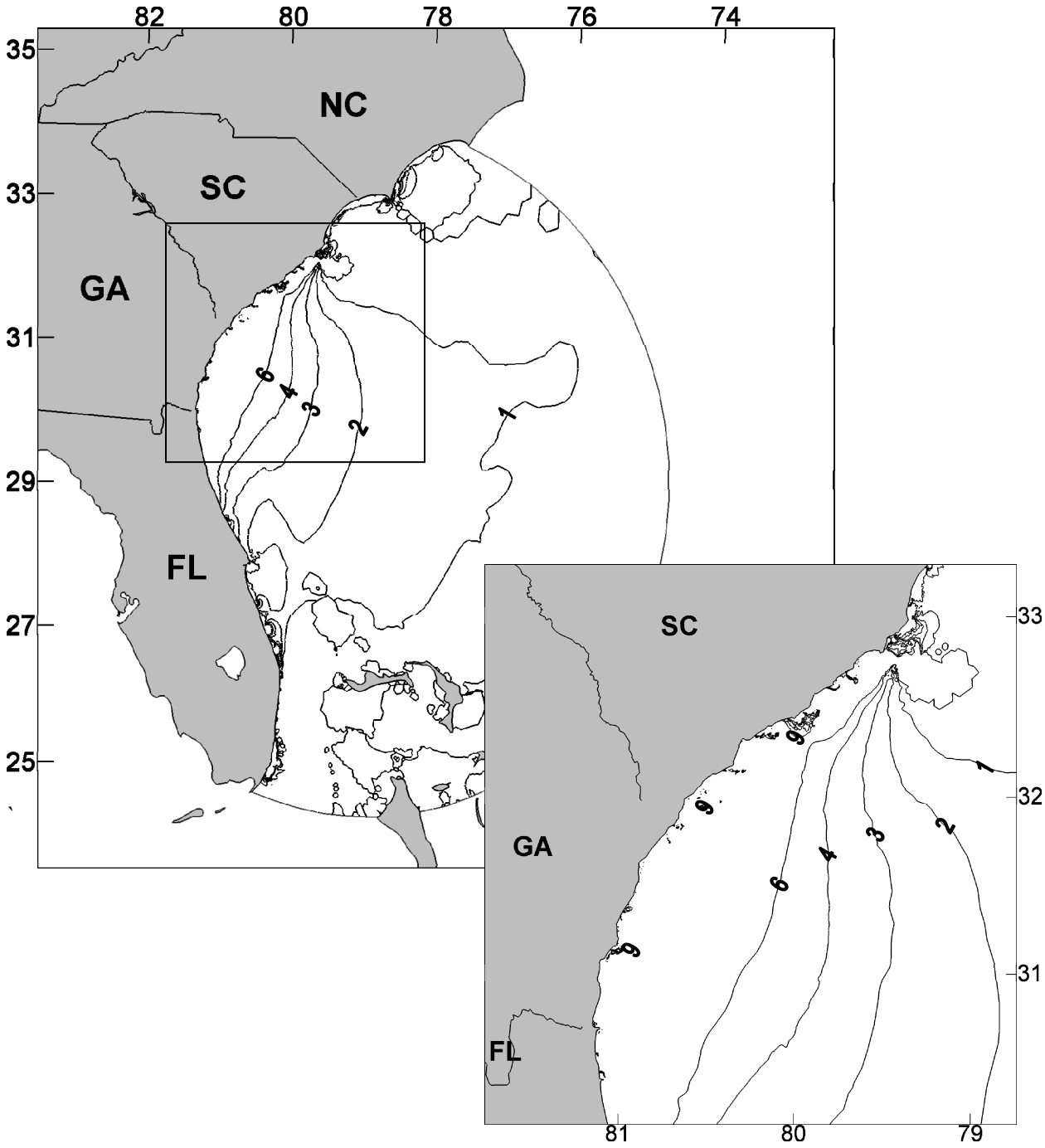

Figure 12.7. Contours of velocity phase differences (°): AICWW minus COASTAL. The inset follows from the box in the larger view.

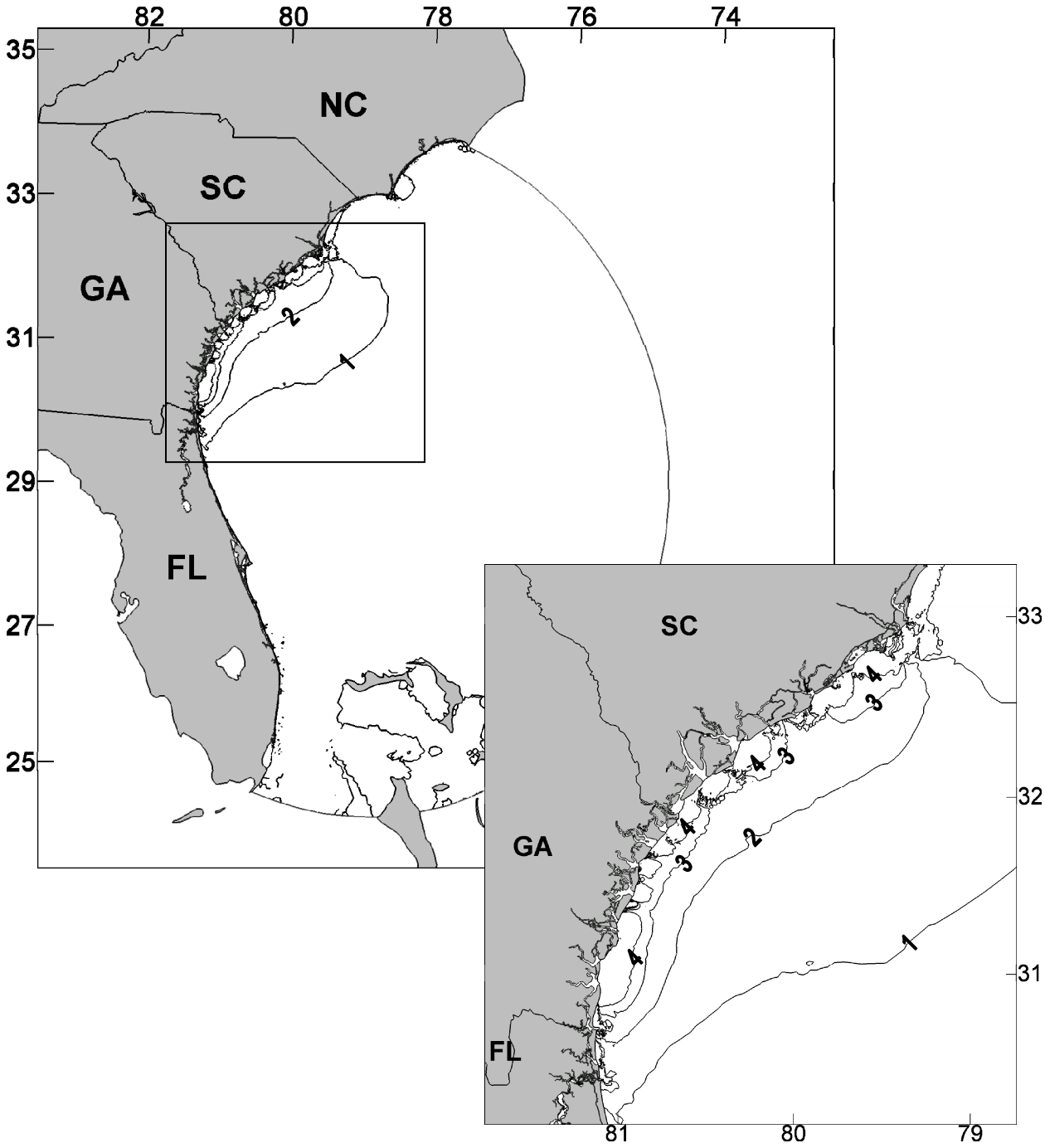

Figure 12.8. Contours of velocity phase differences (°): MARSH minus AICWW. The inset follows from the box in the larger view.

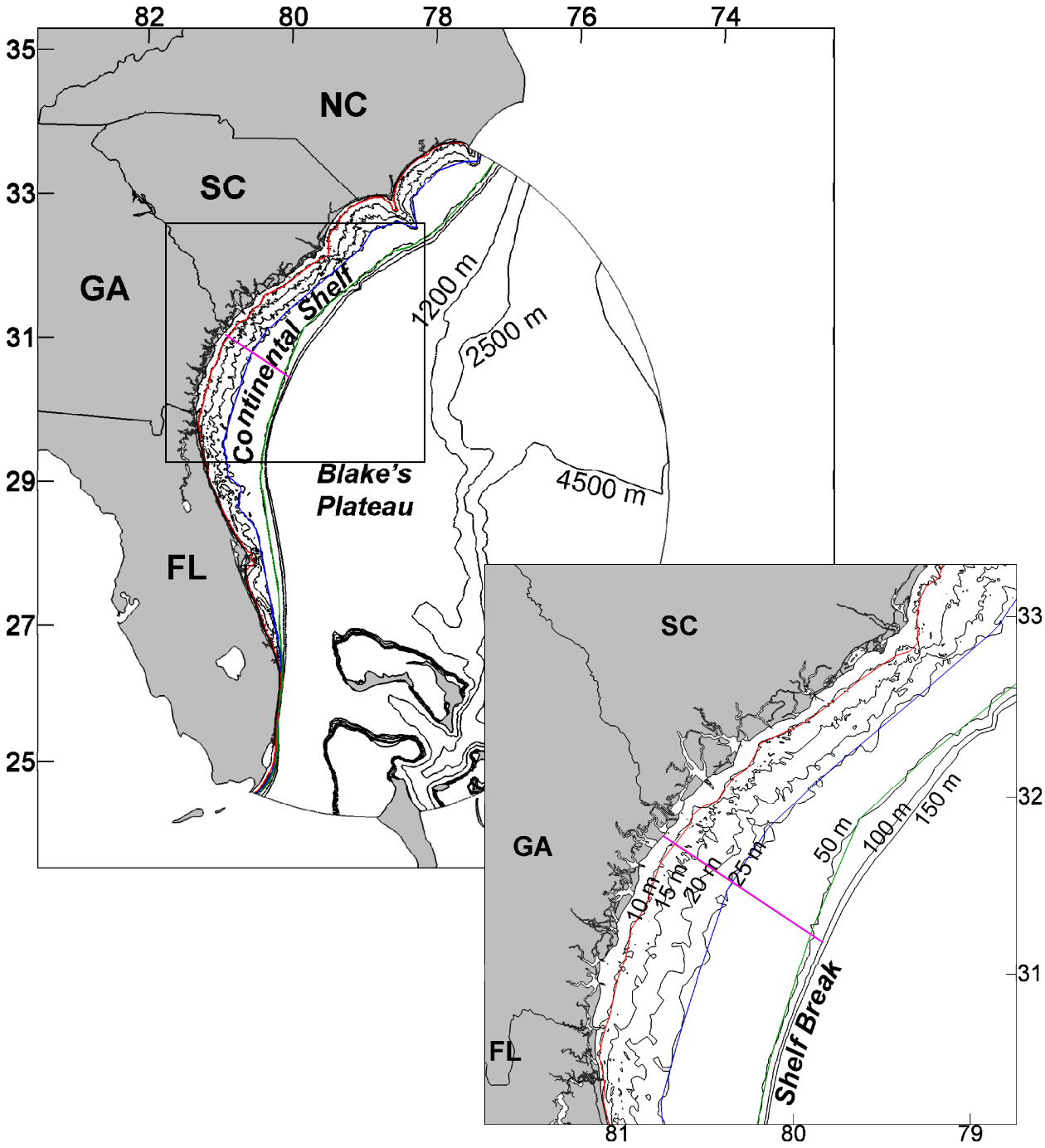

Figure 12.9. The solution ratios and differences are interpolated to 4 transects on the shelf: one cross-shelf from the Georgia/South Carolina border to the 150-m isobath (pink) and three along-shelf at the 10-, 25-, and 50-m isobaths (red, blue, and green, respectively). The inset follows from the box in the larger view.

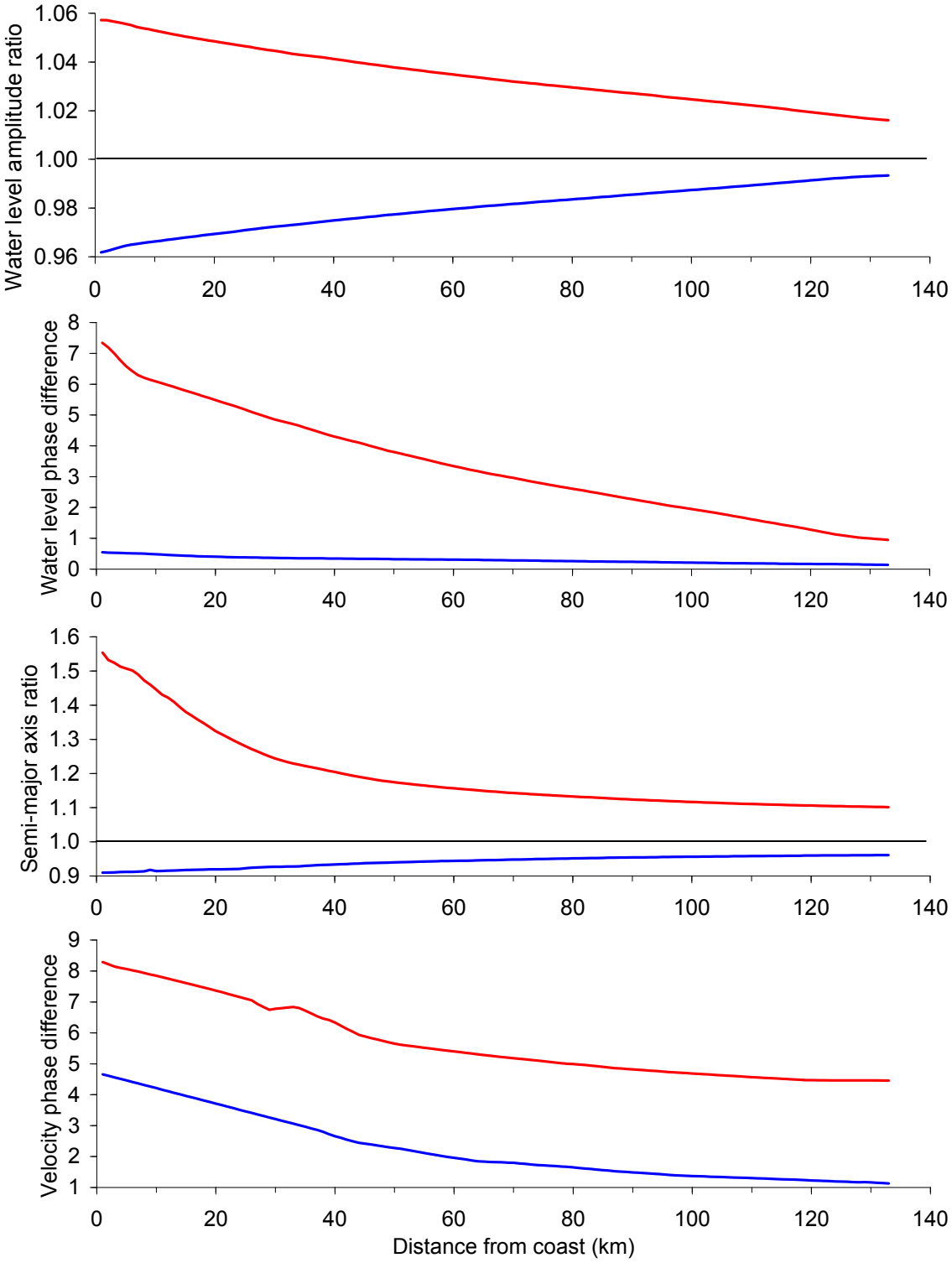

Figure 12.10. Solution ratios and differences interpolated to the cross-shelf transect: AICWW to COASTAL comparisons (red) and MARSH to AICWW comparisons (blue).

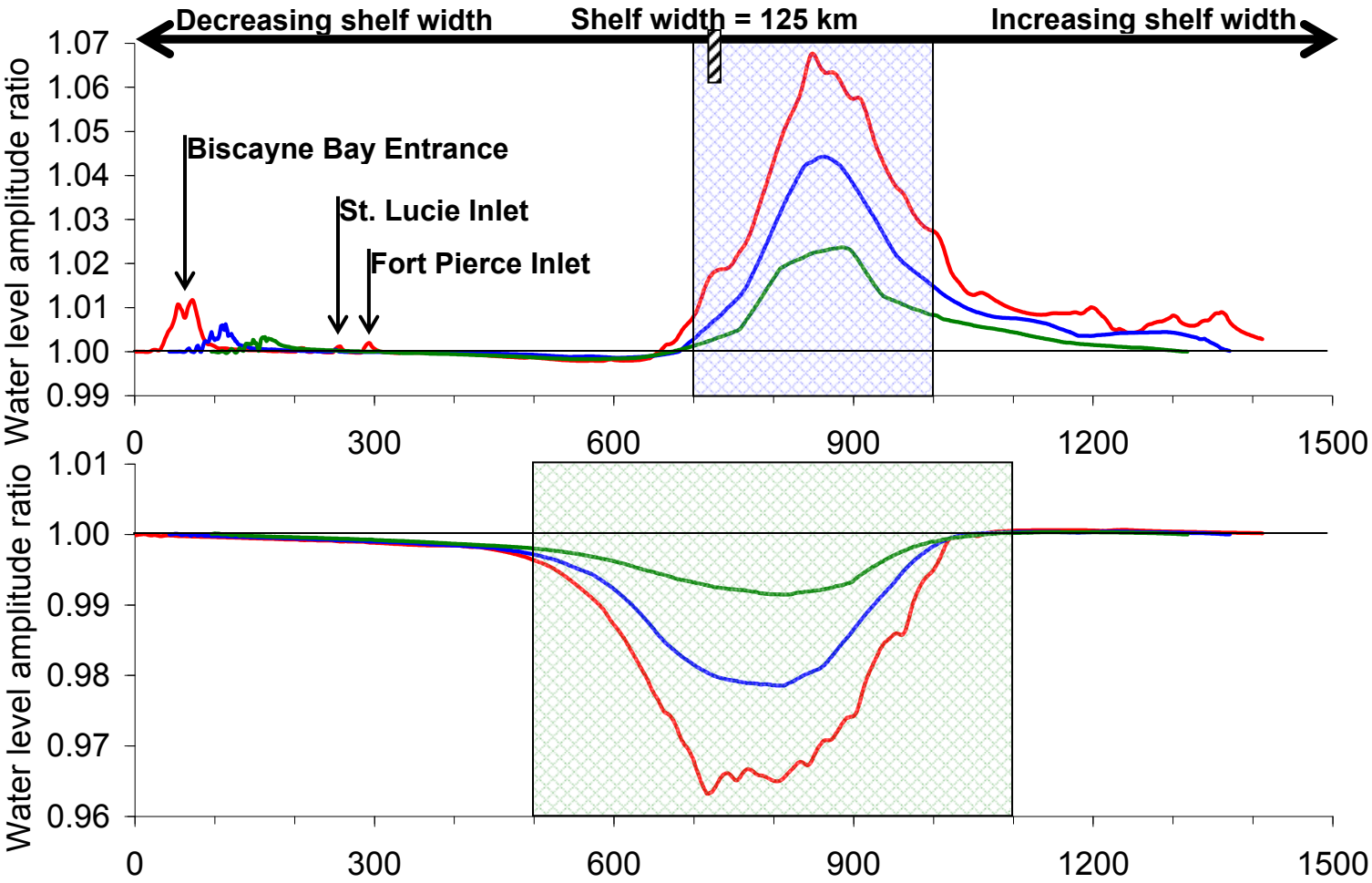

Figure 12.11. Water level amplitude ratios interpolated to the along-shelf transects at the 10-, 25-, and 50-m isobaths: red, blue, and green, respectively. AICWW to COASTAL (top) and MARSH to AICWW (bottom). The blue textured box indicates the portion of coastline $700\,\text{km} \le x \le 1000\,\text{km}$ where the coastal inlets are most densely clustered. The green textured box indicates the region of the intertidal zones: $500\,\text{km} \le x \le 1100\,\text{km}$.

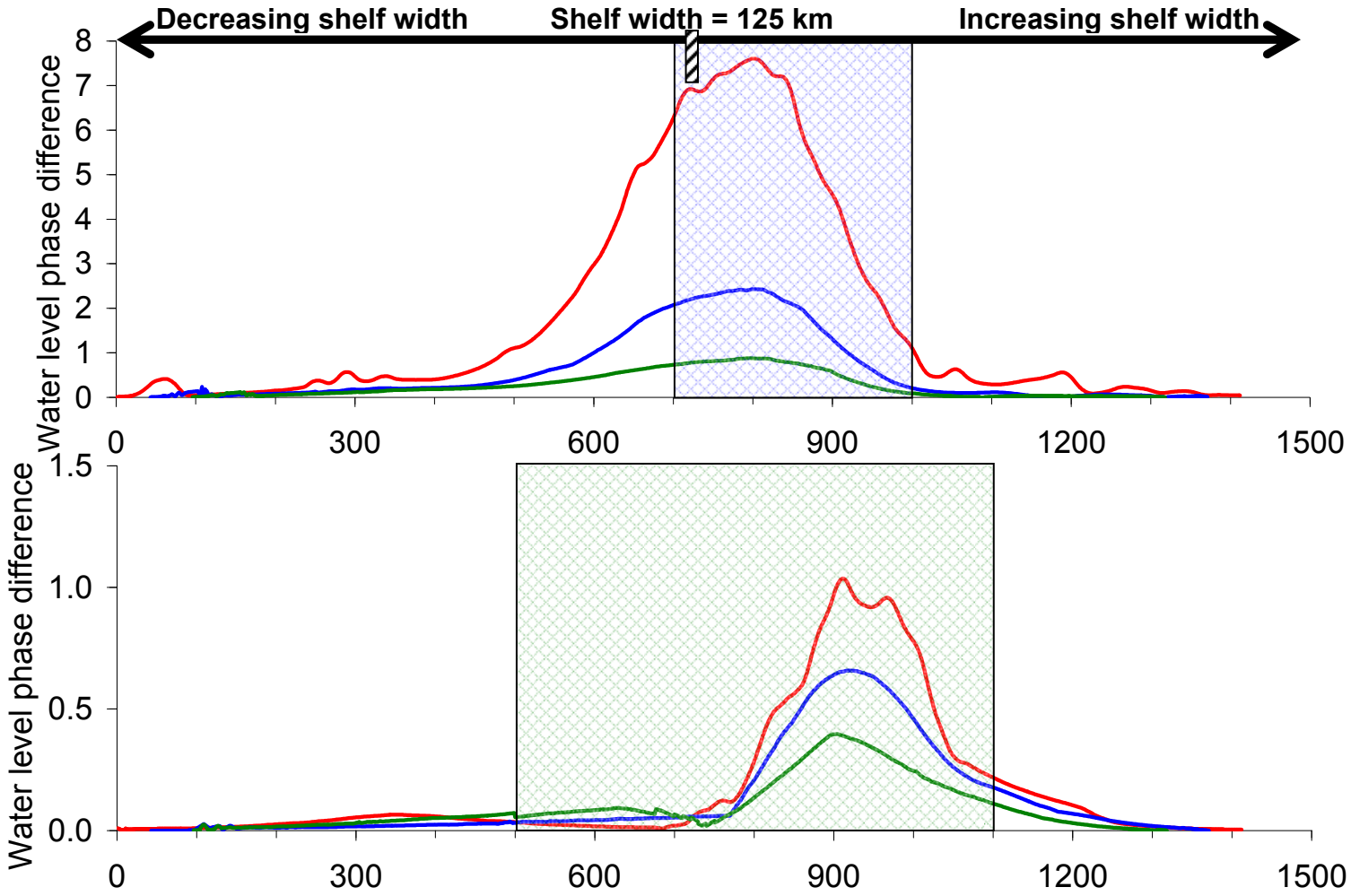

Figure 12.12. Water level phase differences interpolated to the along-shelf transects at the 10-, 25-, and 50-m isobaths: red, blue, and green, respectively. AICWW to COASTAL (top) and MARSH to AICWW (bottom). The blue textured box indicates the portion of coastline $700\,\text{km} \le x \le 1000\,\text{km}$ where the coastal inlets are most densely clustered. The green textured box indicates the region of the intertidal zones: $500\,\text{km} \le x \le 1100\,\text{km}$.

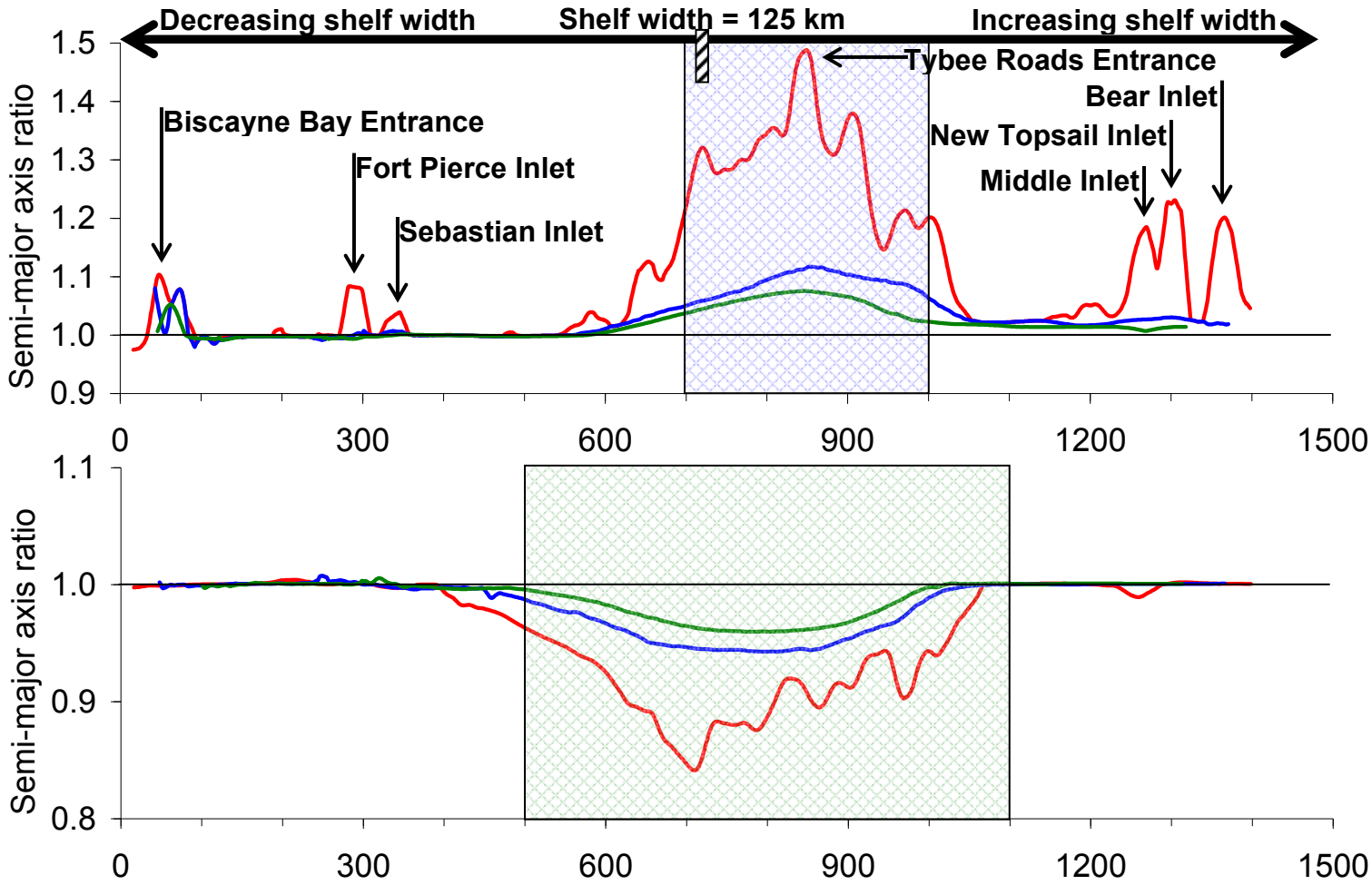

Figure 12.13. Semi-major axis amplitude ratios interpolated to the along-shelf transects at the 10-, 25-, and 50-m isobaths: red, blue, and green, respectively. AICWW to COASTAL (top) and MARSH to AICWW (bottom). The blue textured box indicates the portion of coastline $700\,\text{km} \le x \le 1000\,\text{km}$ where the coastal inlets are most densely clustered. The green textured box indicates the region of the intertidal zones: $500\,\text{km} \le x \le 1100\,\text{km}$.

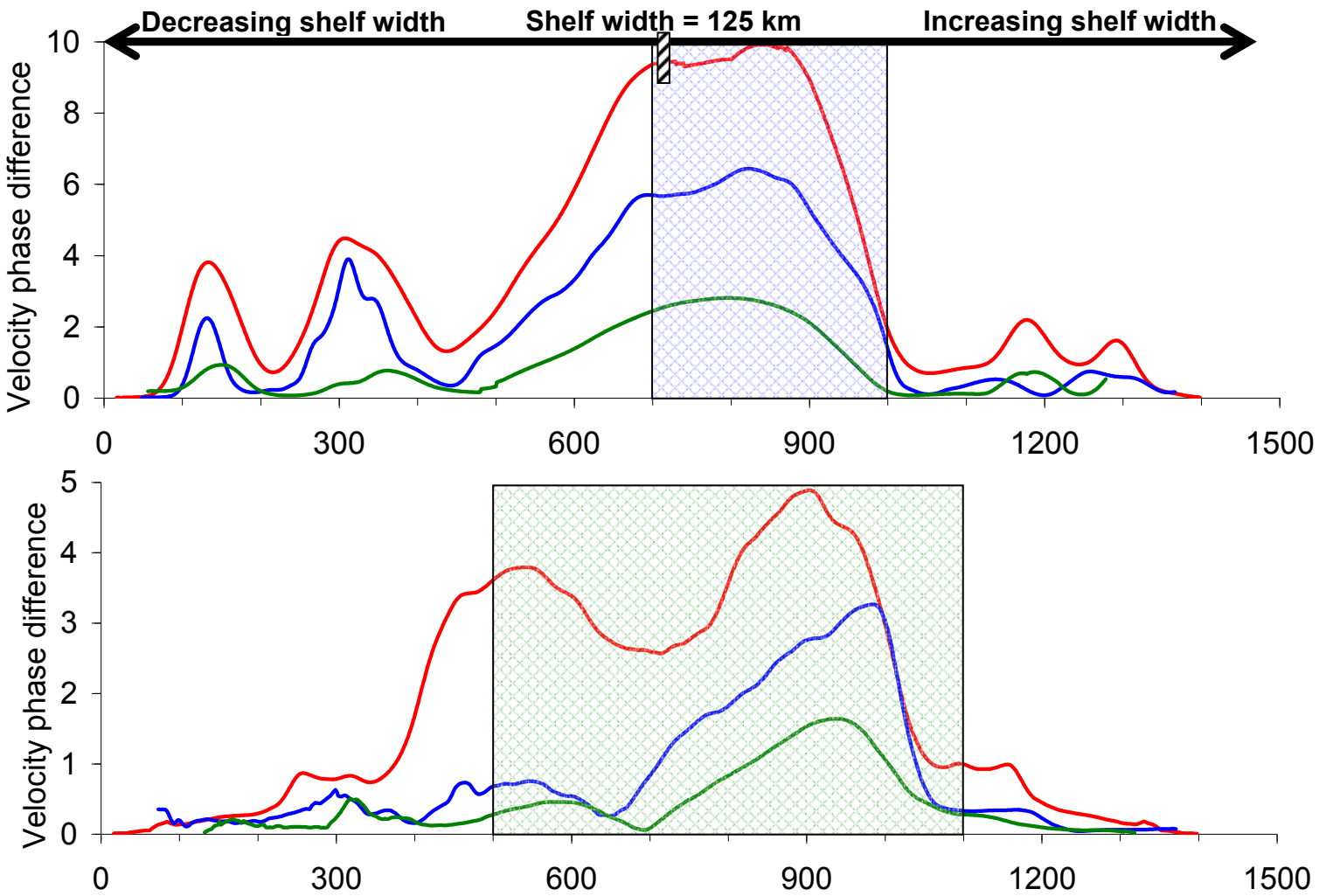

Figure 12.14. Velocity phase differences interpolated to the along-shelf transects at the 10-, 25-, and 50-m isobaths: red, blue, and green, respectively. AICWW to COASTAL (top) and MARSH to AICWW (bottom). The blue textured box indicates the portion of coastline $700\,\text{km} \le x \le 1000\,\text{km}$ where the coastal inlets are most densely clustered. The green textured box indicates the region of the intertidal zones: $500\,\text{km} \le x \le 1100\,\text{km}$.

12.2. Energy Dissipation

This section analyzes the energy dissipation characteristics of the COASTAL, AICWW, and MARSH models. The term "model" is used herein to imply that the inputs to the simulation (spatial discretization and node-by-node friction assignment) are used together with the output from the simulation (node-by-node depth-integrated velocities) in calculating energy dissipation. Although it is an *a posteriori* calculation, energy dissipation is not purely a diagnostic measure because of the fact that both the simulation inputs and the outputs, which are a function of the inputs, are used in the diagnosis. In other words, dissipation is diagnosed herein for the purpose of gaining further information pertaining to the inputs of the simulation: in this context with respect to the representation of the estuaries in the mesh.

Locally, energy dissipation due to bottom friction can be expressed as the cubic of the depth-integrated velocity magnitude (Taylor, 1919):

$$\varepsilon = \frac{C_{f_{\min}} \rho}{T} \int_T \left[U(t)^2 + V(t)^2 \right]^{\frac{3}{2}} dt \quad \ldots\ldots\ldots\

over an M2 tidal period. On the shelf, the largest dissipation rates at the midshelf off Georgia's coast: 10^{-1} W/m^2. Note this is also where the shelf velocities are relatively large. Of the entire domain, dissipation is greatest in the estuaries: beyond $10^{-0.1}$ W/m^2.

To better understand the distribution of energy dissipation in the domain, integrals of the dissipation rate are computed as $T_\varepsilon = \iint_A \varepsilon dA$ where the area of integration A is split into three regions: 1) all shelf and ocean waters found seaward of the uninterrupted coastline; 2) the estuary waterbodies; and 3) the intertidal zones. Table 12.1 presents geometric measures and regional energy dissipation rates for the three different areas. The initial observation is that the MARSH model dissipates the most M2 energy of all mesh applications: over 10% more than the AICWW dissipation and more than double the COASTAL dissipation. This is attributed to the increased tidal velocities occurring in the estuaries as well as the increased tidal velocities occurring on the shelf. The implication is that M2 energy dissipation is increased throughout the domain by the estuaries because of their contribution locally in the estuaries as well as remotely over the shelf. This feature is not captured in the COASTAL model because it does not resolve the estuaries in the mesh. This feature is more prevalent in the MARSH dissipation than the AICWW dissipation implying that the intertidal zones contribute an additional effect.

While the estuaries are marginal features with regard to the volume of the entire South Atlantic Bight, they are shown here to be frictionally dominant components in the hydrodynamic system. Incorporating the inlets and waterbodies into the mesh adds 4300 km^2 (0.7% of 637,000 km^2 total) and only 3.1 km^3 (0.0008% of 3.7×10^5 km^3 total) of surface area and volume, respectively, to the model domain but causes for a near 75% increase in dissipation over the shelf and a doubling of the dissipation domain-wide (Table 12.1). The intertidal zones add 3700 km^2

of surface area (0.6% of 637,000 km^2 total) and 1.2 km^3 of volume (0.0003% of 3.7×10^5 km^3 total) to the overall model geometry but contribute substantially to the total regional energy dissipation: ~0.3 gigawatts of the overall ~1.9 gigawatts. Clearly, there is increased bottom stress over the added surface area locally but also over the shelf.

Figures 12.16 and 12.17 display M4 and M6 energy dissipation rates diagnosed from the MARSH solution: the values shown are $\log_{10} \varepsilon$ calculated from Eq. (12.1) based on integration of the velocity fields over M4 and M6 tidal periods. M4 and M6 energy dissipation is less than M2 dissipation generally by three orders of magnitude (note the difference in the logarithmic values). The greatest M4 and M6 dissipation occurs in the estuaries. The midshelf maxima observed in the M2 dissipation are not present in the M4 and M6 because these overtides are not dispersed until shallower waters are encountered.

The M4 and M6 dissipation rates are integrated over the three identified regions (Table 12.1): 1) shelf and ocean waters; 2) estuary waterbodies; and 3) intertidal zones. The first observation is that much more energy is dissipated by the M4 overtide than by the M6. Furthermore, M4 dissipation shows even more sensitivity to the estuarine representation than was found for the M2. This implies some of the M2 energy is transferred to the M4 overtide and that the estuaries contribute to this nonlinear effect. Not only do the estuaries affect the frictional decay of the fundamental M2 tide but they also affect the nonlinear growth of higher harmonics.

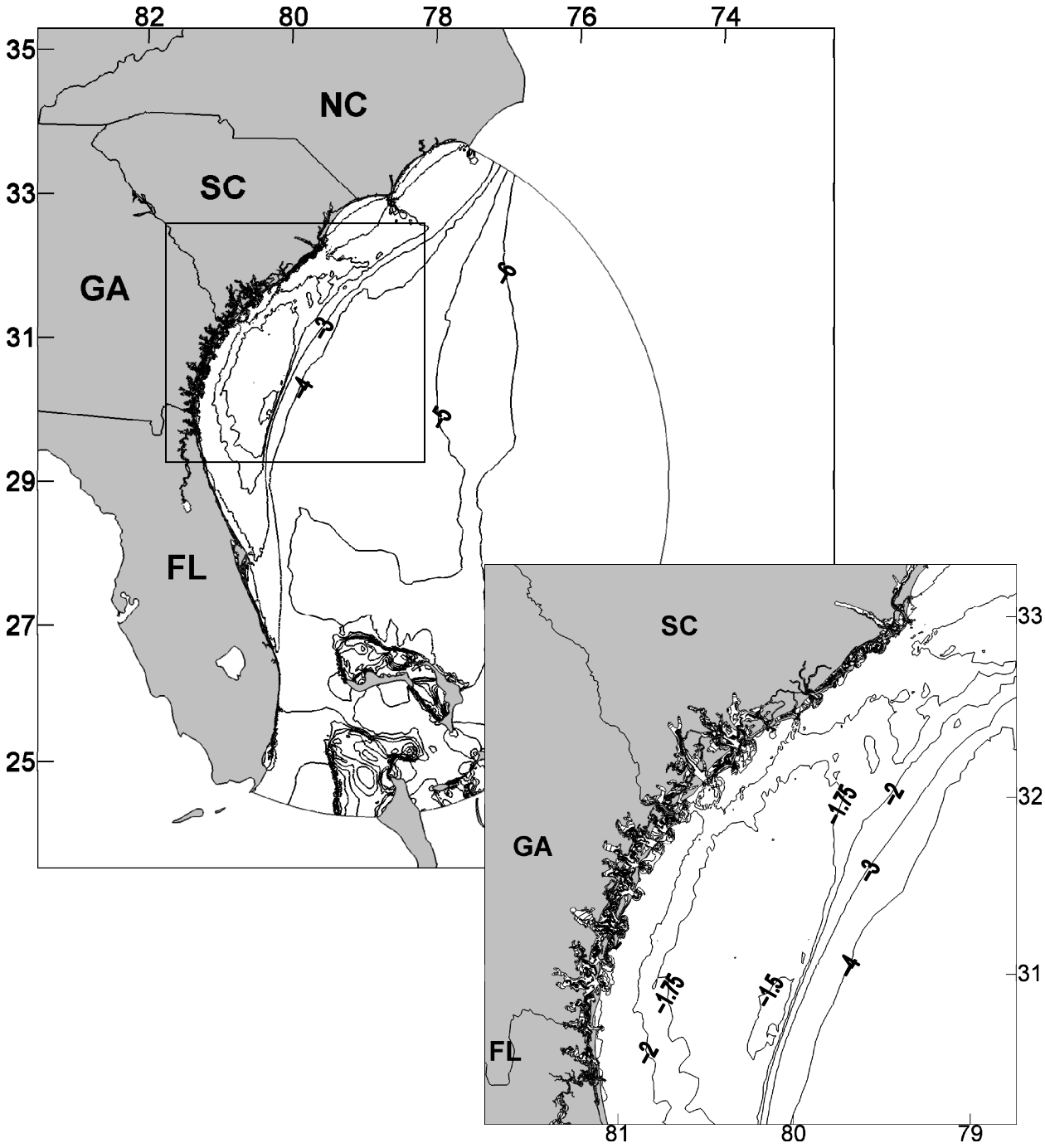

Figure 12.15. M2 Energy dissipation rates diagnosed from the MARSH solution. Shown is the scalar value of $\log_{10} \varepsilon$. The inset follows from the box in the larger view.

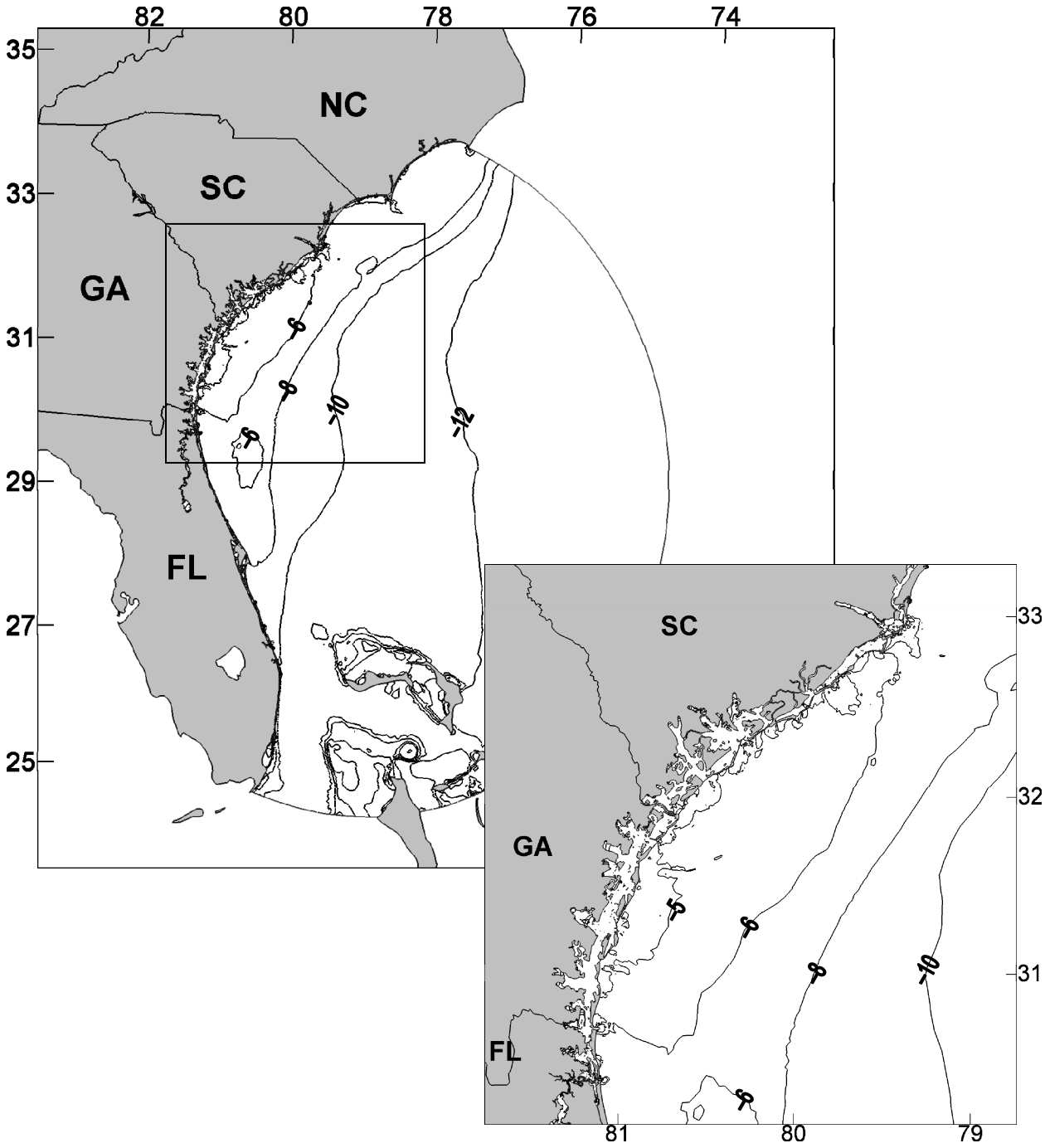

Figure 12.16. M4 Energy dissipation rates diagnosed from the MARSH solution. Shown is the scalar value of $\log_{10} \varepsilon$. The inset follows from the box in the larger view.

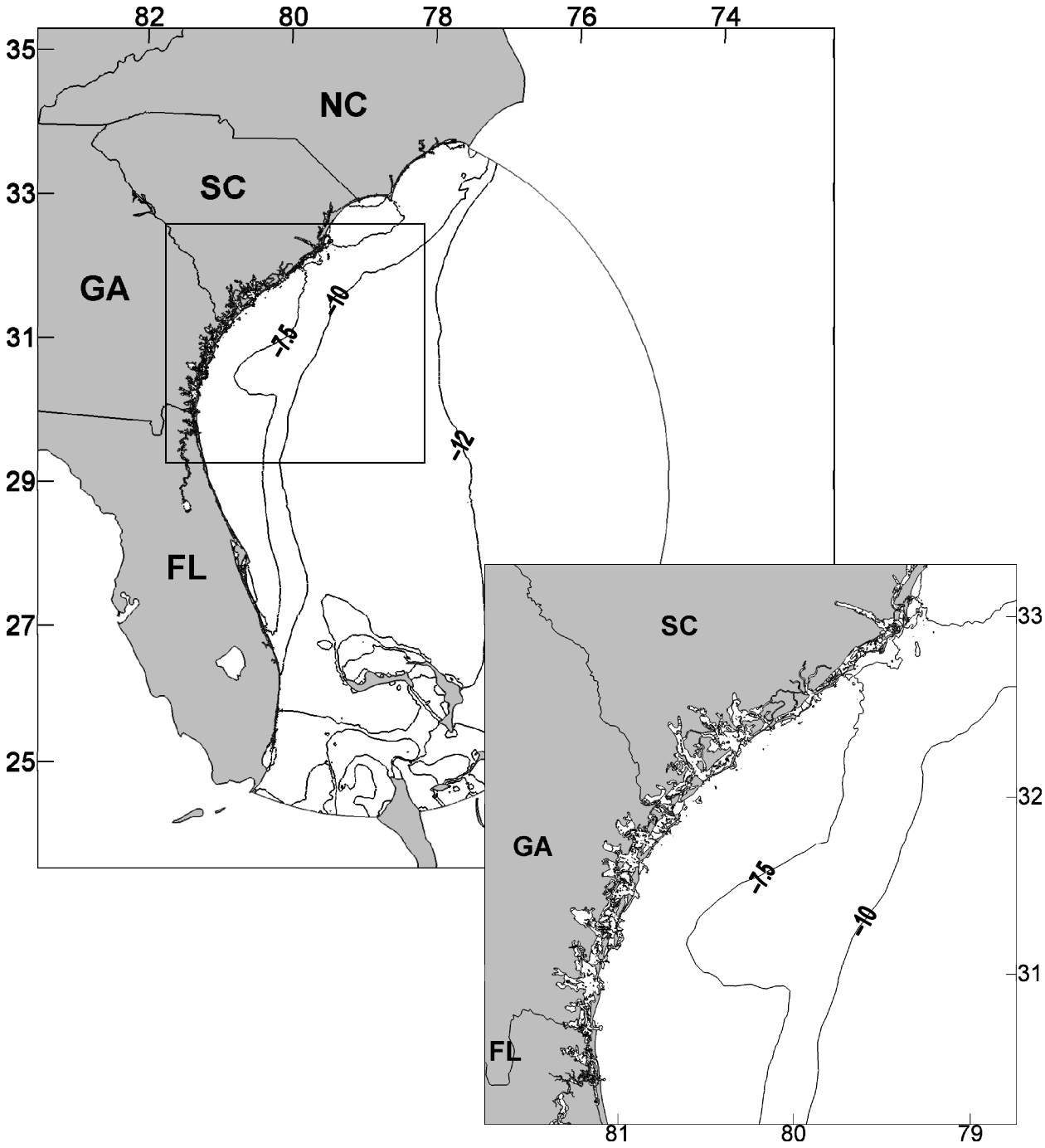

Figure 12.17. M6 Energy dissipation rates diagnosed from the MARSH solution. Shown is the scalar value of $\log_{10} \varepsilon$. The inset follows from the box in the larger view.

Table 12.1. Geometric measures and regional energy dissipation rates ε for three different regions in the domain: 1) all shelf and ocean waters found seaward of the uninterrupted coastline; 2) the estuary waterbodies; and 3) the intertidal zones. Note the COASTAL mesh cannot compute in the estuary waterbodies and intertidal zones and the AICWW mesh cannot compute in the intertidal zones. Note the M4 and M6 dissipation rates are three orders of magnitude less than the M2 rates: units of MW (megawatts) versus GW (gigawatts).

Mesh	Shelf/ocean	Waterbodies[a]	Intertidal	Total
Surface area ($\times 10^3$ km^2)	629	4.3	3.7	637
Volume (km^3)	3.7×10^5	3.1	1.2	3.7×10^5
M2 $\varepsilon_{\text{COASTAL}}$ (GW)	0.78	–	–	0.78
M2 $\varepsilon_{\text{AICWW}}$ (GW)	1.31	0.39	–	1.70
M2 $\varepsilon_{\text{MARSH}}$ (GW)	1.26	0.37	0.29	1.92
M4 $\varepsilon_{\text{COASTAL}}$ (MW)	0.16	–	–	0.16
M4 $\varepsilon_{\text{AICWW}}$ (MW)	0.79	0.12	–	0.91
M4 $\varepsilon_{\text{MARSH}}$ (MW)	2.53	0.36	0.16	3.05
M6 $\varepsilon_{\text{COASTAL}}$ (MW)	0.13	–	–	0.13
M6 $\varepsilon_{\text{AICWW}}$ (MW)	0.16	0.04	–	0.20
M6 $\varepsilon_{\text{MARSH}}$ (MW)	0.19	0.06	0.02	0.27

[a] The Atlantic Intracoastal Waterway constitutes 267 km^2 of the overall 4300 km^2 of waterbody surface area and 0.2 km^3 of the overall 3.1 km^3 of waterbody volume.

CHAPTER 13. CONCLUSIONS

This dissertation presents the development and application of a high-resolution, two-dimensional tidal model for the southeastern United States seaboard. All inlets, the Atlantic Intracoastal Waterway, and estuaries along the coast as well as the Lower St. Johns River are incorporated into the finite element mesh. The volume of these estuarine features is 4.3 km^3 and constitutes a small fraction (0.0011%) of the entire South Atlantic Bight volume of 3.7×10^5 km^3. The surface area of that is covered by these estuarine features (8000 km^2) is three orders of magnitude larger (when expressed as a percentage), yet still a small percentage (1.3%) of the overall domain surface area of 637,000 km^2.

The hypothesis of this dissertation is: where the coastline perforations of the southeastern United States seaboard have been shown to affect the tidal hydrodynamics locally and regionally, the interconnectedness of the system and increased dissipation present in the intertidal zones plays a direct role in the tidal hydrodynamics. To test this hypothesis, two-dimensional barotropic tides were simulated in the South Atlantic Bight using different finite element representations of the domain. The mesh variations described the South Atlantic Bight estuaries with varying degrees of inland extent and comprehensiveness for the purpose of exploring the estuarine influence on shelf tidal dynamics.

Foremost, it was established that tidal elevations and velocities in the nearshore and shelf waters are influenced by the South Atlantic Bight estuaries thereby supporting the hypothesis in part. This remote impact of the estuaries was shown neither to reach the deeper offshore waters nor to extend beyond the region of dense inlets and extensive marsh areas. It was also found that

the estuarine influence is far greater on tidal velocities than on elevations and extends further offshore with velocities than with elevations.

Errors of fit between model solutions and historical data were reduced with further estuarine definition in the mesh. The solution was improved by incorporating the inlets and estuary waterbodies into the mesh but performed best when the mesh included the intertidal zones in addition to the inlets and estuary waterbodies. This was observed at both local and shelf sites: the estuarine influence is not localized to the estuaries but also extends over the shelf.

Constructing the model to incorporate the entire estuarine system and represent their frictional character led to the best performing solution. The increased hydraulic connectivity caused by the Atlantic Intracoastal Waterway was posed initially as a reason for an observed estuarine influence on shelf circulation. This idea came about from a local perspective where the Atlantic Intracoastal Waterway was identified as a greater contributor to tidal circulation than the surrounding tidal flats in the Loxahatchee River estuary (Bacopoulos and Hagen, 2009). This dissertation corroborates their findings with respect to the local influence of the Atlantic Intracoastal Waterway; however, it has been demonstrated that dissipation is the major component behind the estuarine influence on shelf circulation.

The estuary waterbodies occupy 4300 km^2 of surface area with increased bottom stress (relative to offshore) and the additional intertidal zones add a smaller amount of surface area (3700 km^2) with even greater bottom stress. Combined these inshore regions result in ~0.7 GW of additional M2 energy to be locally dissipated. What is remarkable is that the increase in energy dissipation is also exhibited on the shelf. In fact, when the entire estuarine system is included in the model, the total amount of M2 energy dissipated is nearly 2.5 times greater than without the inshore regions.

In closing, the hypothesis has been proven for the most part: while the full estuarine system does interconnect the system hydraulics, it is because of the vast region of shallow water flow with increased dissipation in the marshes that local and regional tidal hydrodynamics are influenced by the estuaries. The final conclusion is that the full estuarine system is an important component to consider with respect to barotropic tides in the South Atlantic Bight. The estuaries should be included when modeling the bight tides especially if circulation is to be accurately simulated from first principles with minimal calibration.

APPENDIX A. STANDING WAVE DYNAMICS

Tides can be described as long waves on a rotating Earth (Pugh, 2004). Consider a progressive wave traveling along a one-dimensional space x (Figure A.1). If the amplitude is small compared with depth and the depth is small compared to the wavelength (i.e., $\zeta << D << \lambda$), then the progressive wave acts as a shallow water wave and travels at a speed c proportional to the square root of the depth:

$$c = \sqrt{gD} \quad \text{(A.1)}$$

and g relates to the acceleration due to gravity. Now express the wave speed as the time T it takes for one wavelength λ to pass a fixed point in space:

$$c = \frac{\lambda}{T} \quad \text{(A.2)}$$

then combine this with the expression given in Eq. (A.1) to isolate the wavelength on the left hand side:

$$\lambda = T\sqrt{gD} \quad \text{(A.3)}$$

Two equal progressive waves traveling in opposite directions results in a fixed (or frozen) wave motion known as a standing wave. The mathematical representation for a standing wave can be derived from a basin where the two equal progressive waves, traveling in opposite directions, reflecting perfectly at both ends of the basin. The behavior is similar to that of a swinging pendulum: maximum potential energy is fully transferred to maximum kinetic energy

and maximum kinetic energy is fully transferred back to maximum potential energy. Figure A.2 depicts this behavior in the context of a standing wave in a basin. Note the natural period of oscillation for the basin is equal to the time it takes for the wave to travel from one end to the other and back:

$$T = \frac{2L}{\sqrt{gD}} \quad \text{(A.4)}$$

where L relates to the length of the basin.

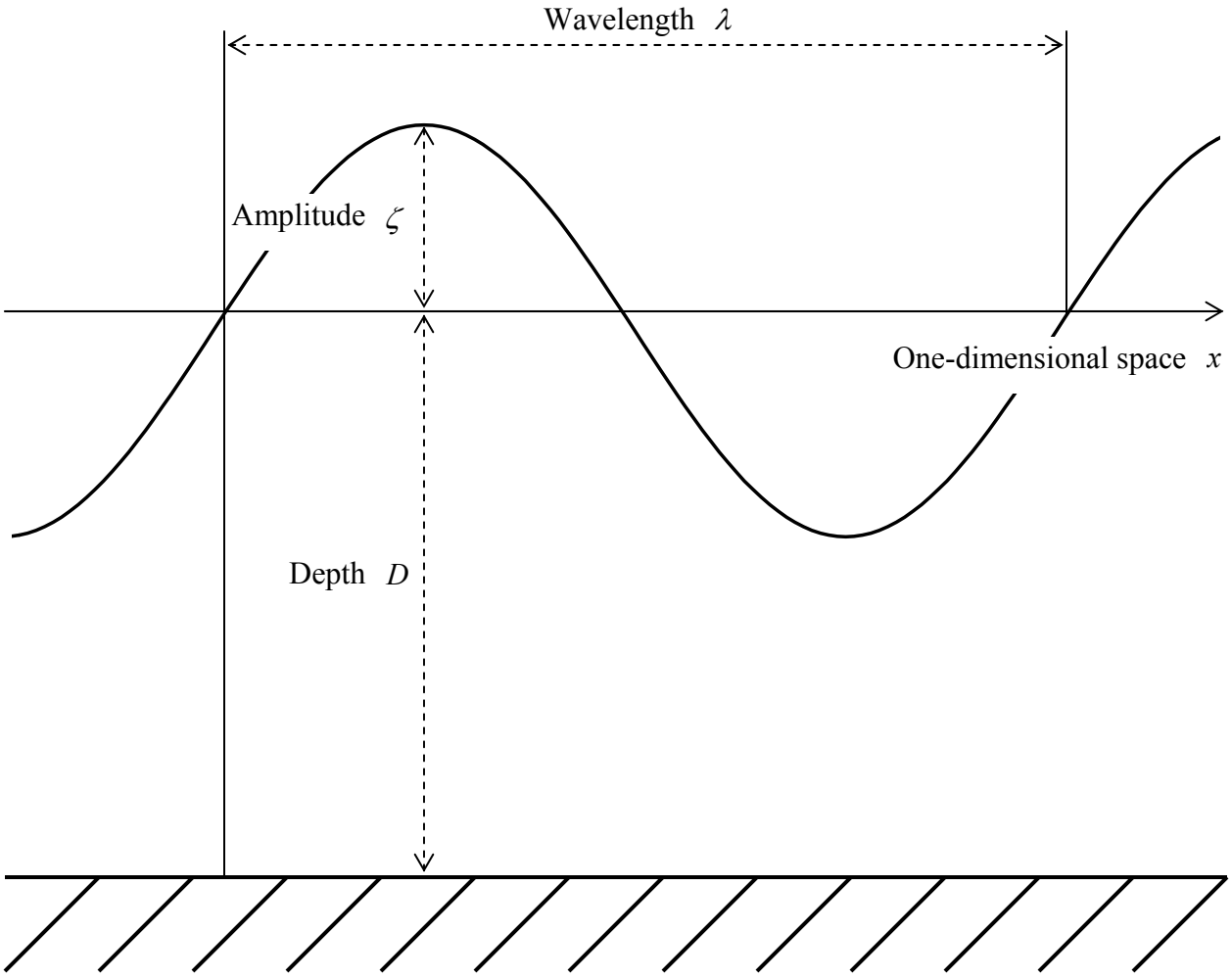

Figure A.1. Characteristics of a one-dimensional progressive wave.

Semi-diurnal tides predominate in the western North Atlantic Ocean because of the basin dimensions. If the length scale is set equal to 4500 km and the depth is approximated as 4000 m, then the resulting natural period of oscillation is calculated as ~12.5 hours: very near the semi-diurnal frequency. This explains the dominance of the M2 tidal constituent in the western North Atlantic Ocean.

APPENDIX B. TIDAL ELLIPSES

The tidal ellipse can be decomposed into two rotary components (Gonella, 1972):

$$w = u + iv \quad \ldots\ldots\ldots\

The longitudinal (traversing meridians of longitude/east-west movement) and latitudinal (traversing parallels of latitude/north-south movement) components of the tidal current are given respectively as:

$$u = a_u \cos(\omega t - \varphi_u) \qquad (\text{longitudinal component})$$

$$v = a_v \cos(\omega t - \varphi_v) \qquad (\text{latitudinal component}) \quad \ldots\ldots\ldots\ldots\ldots\ldots\ldots\ldots\ldots\ldots \text{(B.2)}$$

where a_u, a_v = amplitudes of the *u*- and *v*-component velocities, respectively; and φ_u, φ_v = Greenwich phases of the *u*- and *v*-component velocities, respectively. Now substitute the rotary components of Eq. (B.2) into the complex expression of Eq. (B.1). The resulting relationship is then simplified using Euler's formula, which yields expressions for the two circles generating the tidal ellipse:

$$w = a_u \cos(\omega t - \varphi_u) + i a_v \cos(\omega t - \varphi_v)$$

$$= a_u \frac{e^{i(\omega t - \varphi_u)} + e^{-i(\omega t - \varphi_u)}}{2} + i a_v \frac{e^{i(\omega t - \varphi_v)} + e^{-i(\omega t - \varphi_v)}}{2}$$

$$= \frac{a_u e^{-i\varphi_u} + i a_v e^{-i\varphi_v}}{2} e^{i\omega t} + \frac{a_u e^{i\varphi_u} + i a_v e^{i\varphi_v}}{2} e^{-i\omega t}$$

$$= w_{anti} e^{i\omega t} + w_{clock} e^{-i\omega t}$$

$$\overset{\text{or}}{=} W_{anti} e^{i(\omega t + \theta_{anti})} + W_{clock} e^{i(\omega t + \theta_{clock})} \quad \ldots\ldots\ldots\ldots\ldots\ldots\ldots\ldots\ldots\ldots\ldots\ldots\ldots\ldots\ldots\ldots\ldots\ldots \text{(B.3)}$$

where the counterclockwise and clockwise rotating circles are written explicitly as:

$$w_{anti} \equiv W_{anti} e^{i\theta_{anti}} = \frac{\widetilde{u} + i\widetilde{v}}{2} \qquad (\text{counterclo ckwise rotation})$$

$$w_{clock} \equiv W_{clock} e^{i\theta_{clock}} = \left(\frac{\widetilde{u} - i\widetilde{v}}{2} \right)^{*} \qquad (\text{clockwise rotation}) \quad \ldots\ldots\ldots\ldots\ldots\ldots\ldots\ldots \text{(B.4)}$$

and the $(\ )^{*}$ notation indicates the complex conjugate operator; and $\widetilde{u} = a_u e^{-i\phi_u}$ and $\widetilde{v} = a_v e^{-i\phi_v}$ define the complex *u*- and *v*-component amplitudes, respectively. (The minus signs employed in front of the phase angles signify lags in the tidal currents.)

The rotation of the tidal ellipse is dictated by the relative lengths of the two circular radii:

$$W_{anti} > W_{clock} \qquad (\text{see Eqs.}[\text{A.3 and A.4}]) \quad (\text{counterclockwise rotation in tidal ellipse})$$

$$W_{anti} = W_{clock} \qquad (\text{see Eqs.}[\text{A.3 and A.4}]) \quad (\text{rectilinear behavior in tidal ellipse})$$

$$W_{anti} < W_{clock} \qquad (\text{see Eqs.}[\text{A.3 and A.4}]) \quad (\text{clockwise rotation in tidal ellipse}) \quad \ldots\ldots\ldots\ldots \text{(B.5)}$$

and the tidal current reaches a maximum when the two circular radii are aligned in the same direction (via Eq. [B.3]):

$$\omega t + \theta_{anti} = -\omega t + \theta_{clock} + 2k\pi \qquad ; \qquad k = 0, \pm 1, \pm 2, \ldots \quad \ldots\ldots\ldots\ldots\ldots\ldots\ldots\ldots \text{(B.6)}$$

where the time of maximum tidal current $t_{\max}$ occurs at a phase angle relative to Greenwich:

$$g = \omega t_{\max} = \frac{\theta_{clock} - \theta_{anti}}{2} + k\pi \quad \ldots\ldots\ldots\ldots\ldots\ldots\ldots\ldots\ldots\ldots\ldots\ldots\ldots\ldots\ldots\ldots\ldots\ldots\ldots\ldots\ldots\ldots \text{(B.7)}$$

and it is sufficient to assign $k = 0$ or $k = 1$ due to the fact that the two oppositely rotating circles meet twice per tidal period. The northern axis convention of Foreman (1978) is applied herein to maintain a selection of the major semi-axis whose angle lies within the range $[0,180)$.

Next, substitute the phase angle of Eq. (B.7) into the complex expression of Eq. (B.3):

$$\begin{aligned} w_{\max} &= W_{anti} e^{i(\omega t_{\max} + \theta_{anti})} + W_{clock} e^{-i(\omega t_{\max} - \theta_{clock})} \\ &= W_{anti} e^{i\left(\frac{\theta_{clock} + \theta_{anti}}{2} + k\pi\right)} + W_{clock} e^{-i\left(\frac{-\theta_{clock} - \theta_{anti}}{2} + k\pi\right)} \\ &= W_{anti} e^{i\left(\frac{\theta_{clock} + \theta_{anti}}{2} + k\pi\right)} + W_{clock} e^{i\left(\frac{\theta_{clock} + \theta_{anti}}{2} - k\pi + 2k\pi\right)} \\ &= \left(W_{anti} + W_{clock}\right) e^{i\left(\frac{\theta_{clock} + \theta_{anti}}{2} + k\pi\right)} \quad \ldots\ldots\ldots\ldots\ldots\ldots\ldots\ldots\ldots\ldots\ldots\ldots\ldots\ldots\ldots\ldots\ldots\ldots\ldots\ldots\ldots\ldots \text{(B.8)} \end{aligned}$$

where the magnitude and phase angle of the complex maximum velocity produce the length and angle of inclination, respectively, of the semi-major axis:

$$a = |w_{\max}| = W_{anti} + W_{clock} \qquad (\text{length, semi} - \text{major axis})$$

$$\theta = \arg(w_{\max}) = \frac{\theta_{clock} + \theta_{anti}}{2} + k\pi \qquad (\text{angle of inclination, semi} - \text{major axis}) \quad \ldots\ldots\ldots\ldots\ldots\ldots \text{(B.9)}$$

and the following integer count is employed so as to comply with the northern axis convention of Foreman (1978):

$$k = \frac{\mathrm{mod}\left(\frac{\theta_{clock} + \theta_{anti}}{2} + 2\pi, 2\pi \right)}{\pi} \quad \ldots\ldots\ldots\

where the time of minimum tidal current $t_{\min}$ occurs when the following criterion is satisfied:

$$\omega t_{\min} = \frac{\theta_{clock} - \theta_{anti}}{2} + \left(k + \frac{1}{2}\right)\pi \quad \ldots\ldots\ldots\

Positive eccentricity values relate to counterclockwise rotating tidal ellipse and negative eccentricity values relate to a clockwise rotating tidal ellipse (refer also to Eq. [B.5]).

APPENDIX C. INLET CROSS SECTIONS

Six cross-sectional representations are available in central Florida. The cross sections are for 4 tidal inlets (Ponce de Leon, Sebastian, Fort Pierce, and St. Lucie) that service the Indian River lagoon and for 2 inland channels (Haulover Canal and Dragons Point) inside the lagoon (Figure C.1). Bathymetric survey data are available for each cross section (courtesy of the St. Johns River Water Management District). The mesh representation of each cross section agrees very well with the bathymetric survey data (see Figures C.2 through C.7).

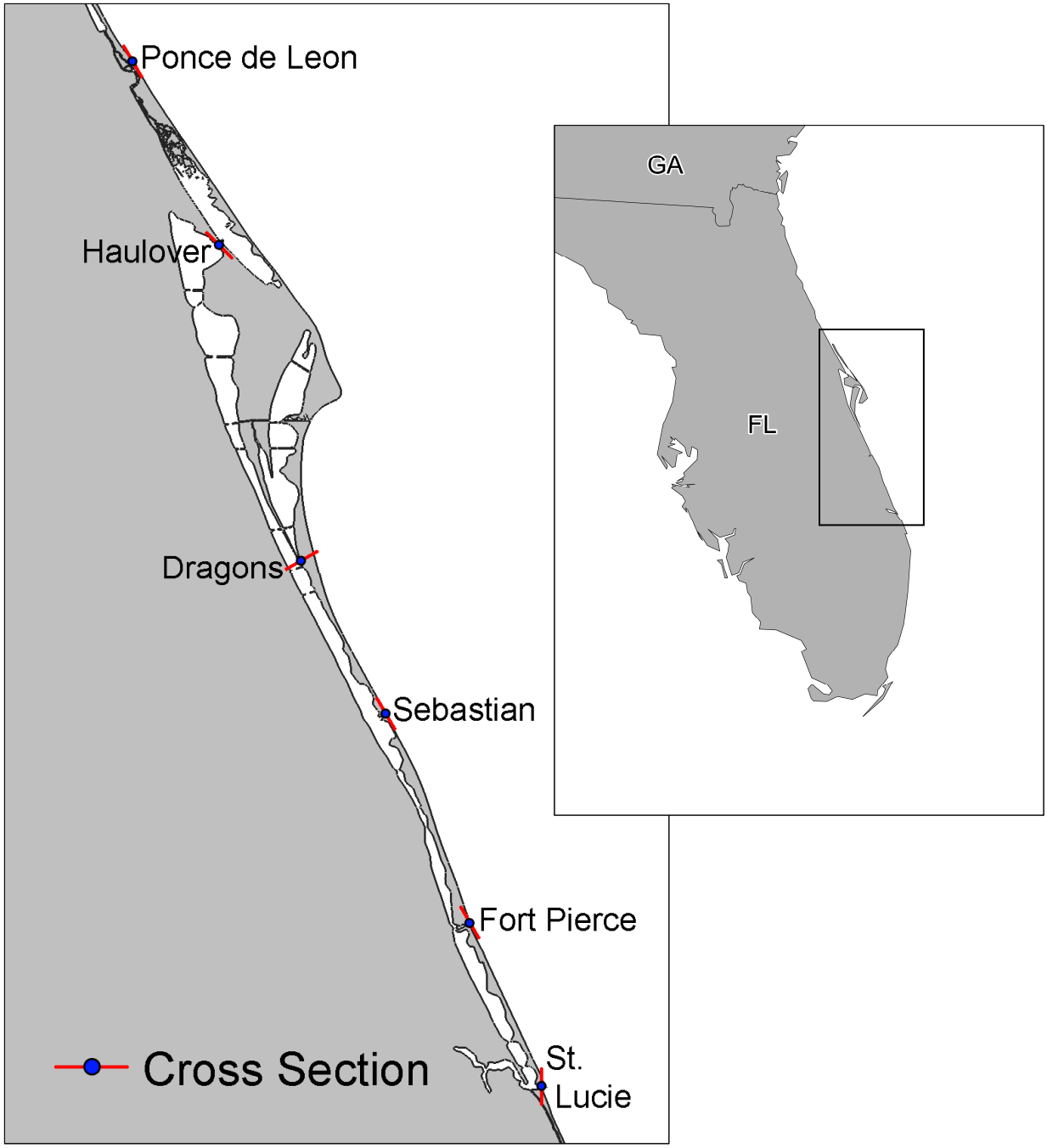

Figure C.1. Six cross-sectional representations are available in central Florida: four tidal inlets (Ponce de Leon, Sebastian, Fort Pierce, and St. Lucie) that service the Indian River lagoon; and two inland channels (Haulover Canal and Dragons Point) inside the lagoon.

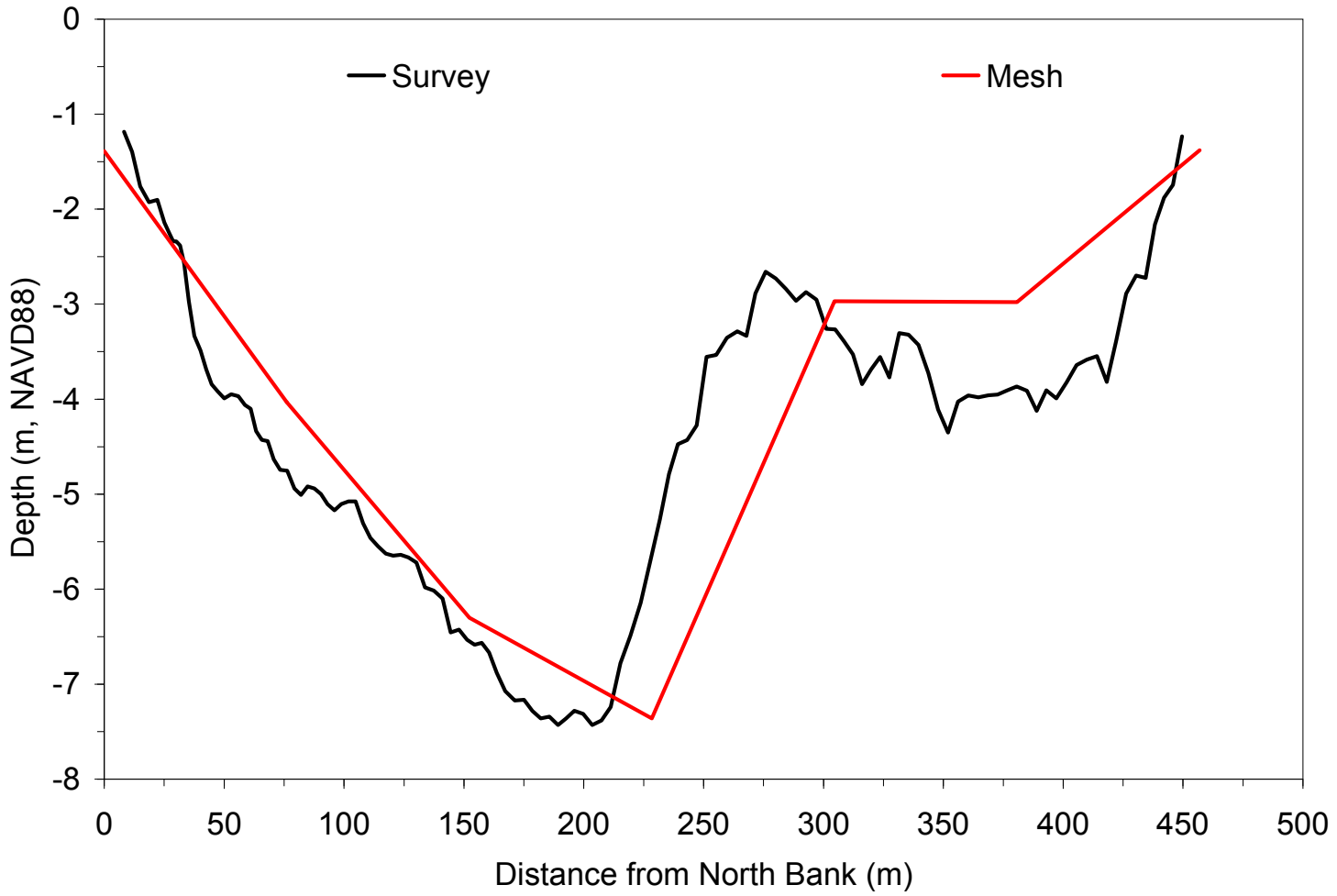

Figure C.2. Cross-sectional representation of Ponce de Leon Inlet. The survey consists of 128 points; the mesh spans 6 elements across (7 points). The mesh represents the cross section with an area of 1905.61 m^2, which compares to 1951.30 m^2 estimated from the survey.

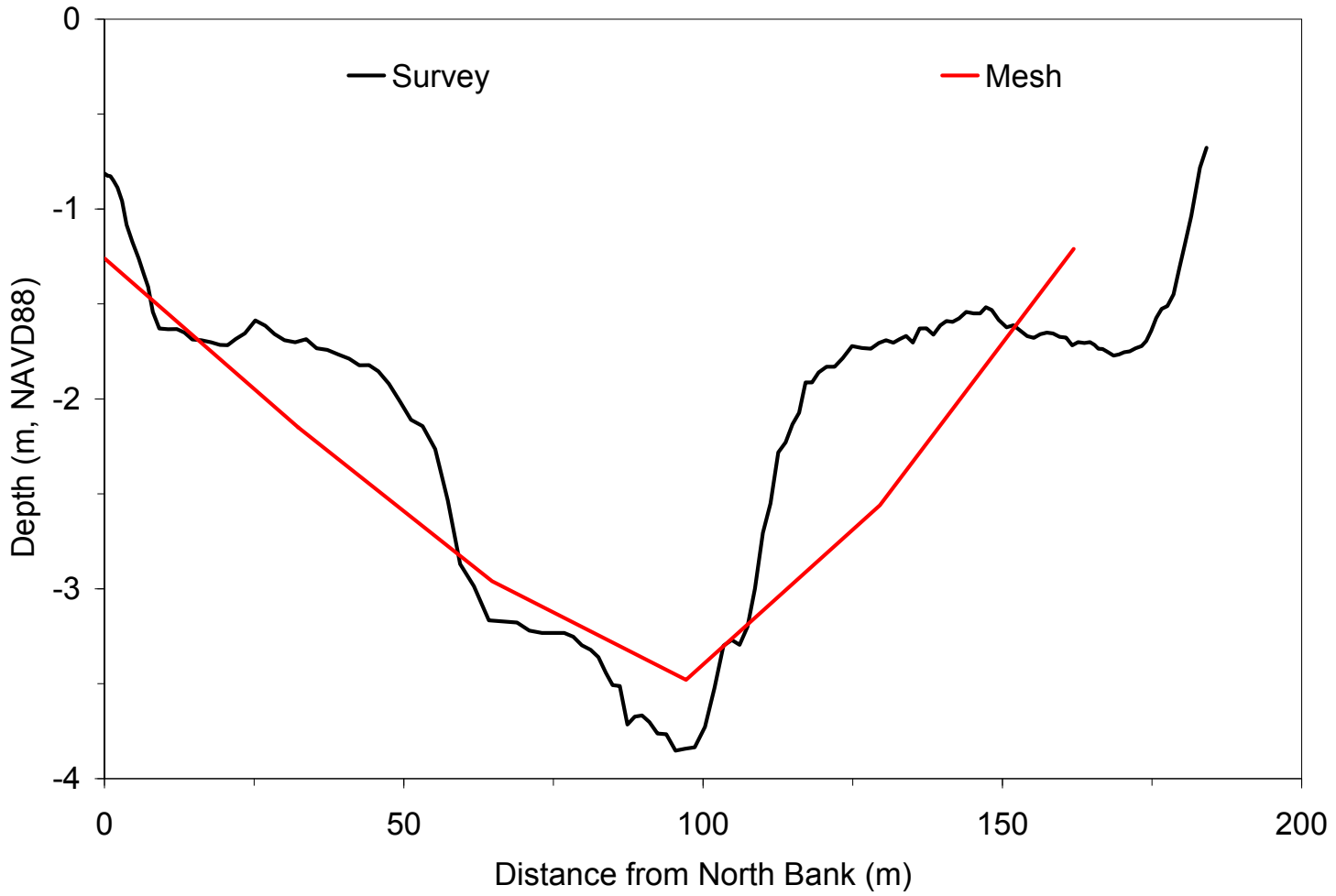

Figure C.3. Cross-sectional representation of Sebastian Inlet. The survey consists of 143 points; the mesh spans 5 elements across (6 points). The mesh represents the cross section with an area of 401.08 m^2, which compares to 399.25 m^2 estimated from the survey.

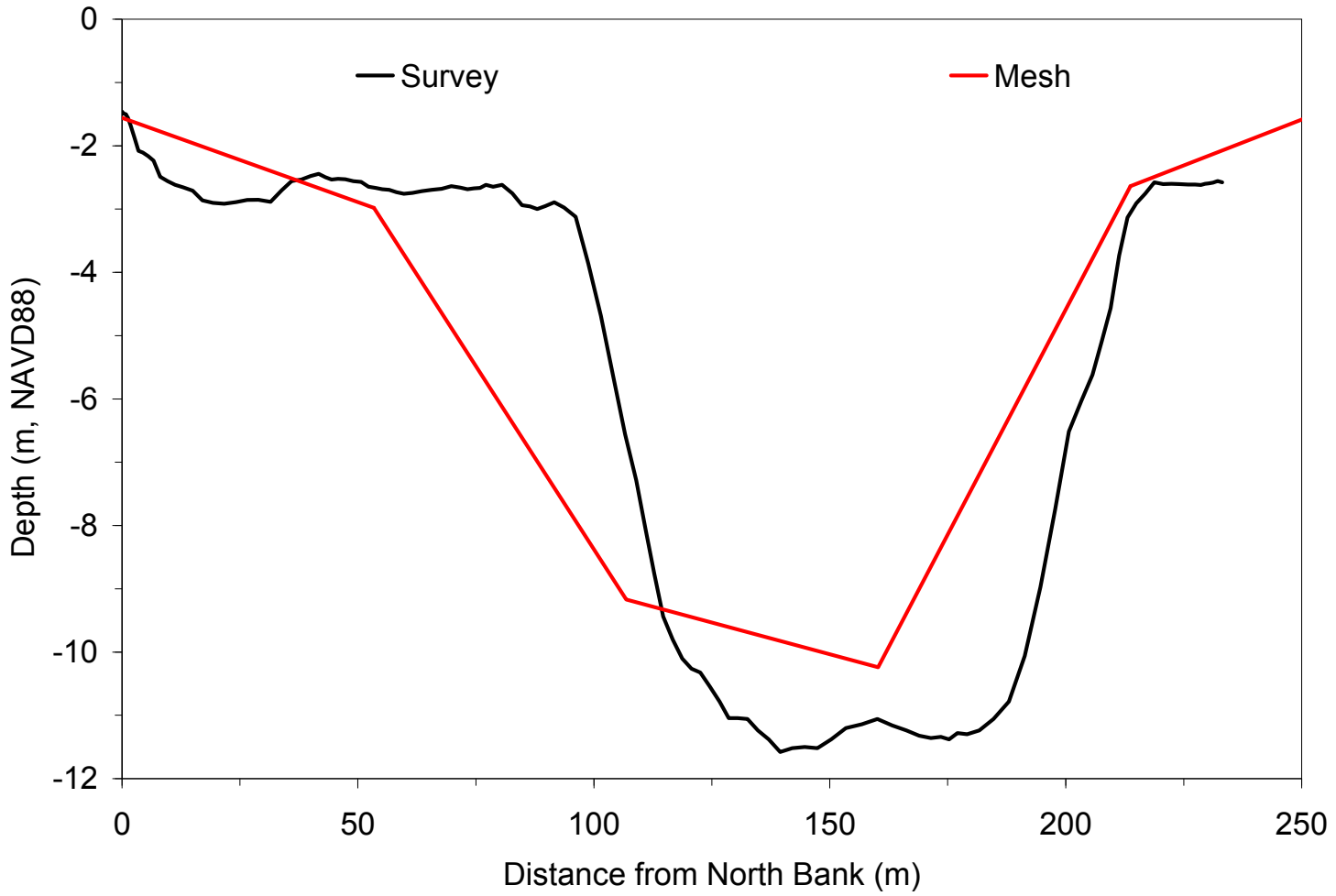

Figure C.4. Cross-sectional representation of Fort Pierce Inlet. The survey consists of 121 points; the mesh spans 5 elements across (6 points). The mesh represents the cross section with an area of 1407.88 m^2, which compares to 1412.43 m^2 estimated from the survey.

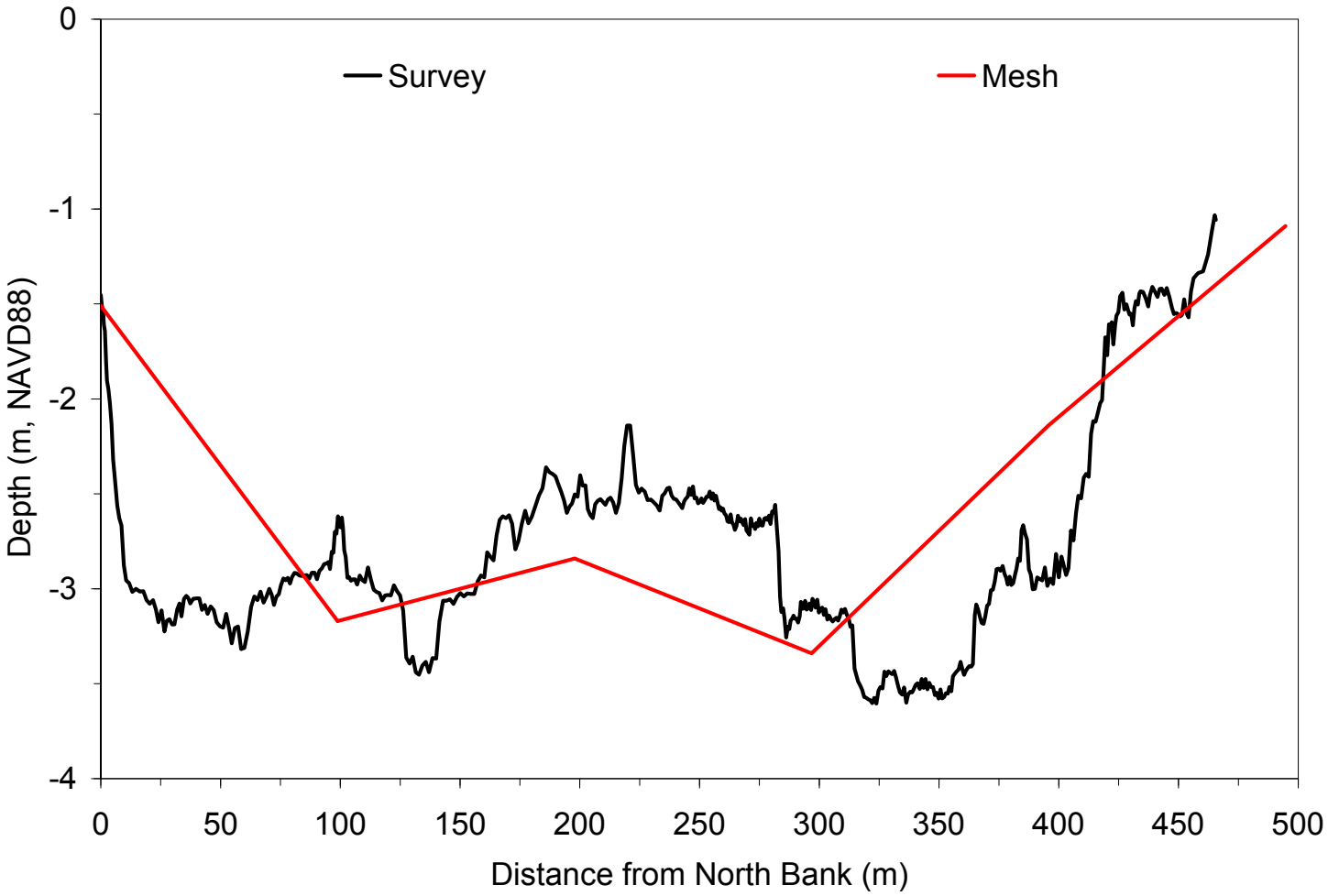

Figure C.5. Cross-sectional representation of St. Lucie Inlet. The survey consists of 504 points; the mesh spans 5 elements across (6 points). The mesh represents the cross section with an area of 1265.19 m^2, which compares to 1290.34 m^2 estimated from the survey.

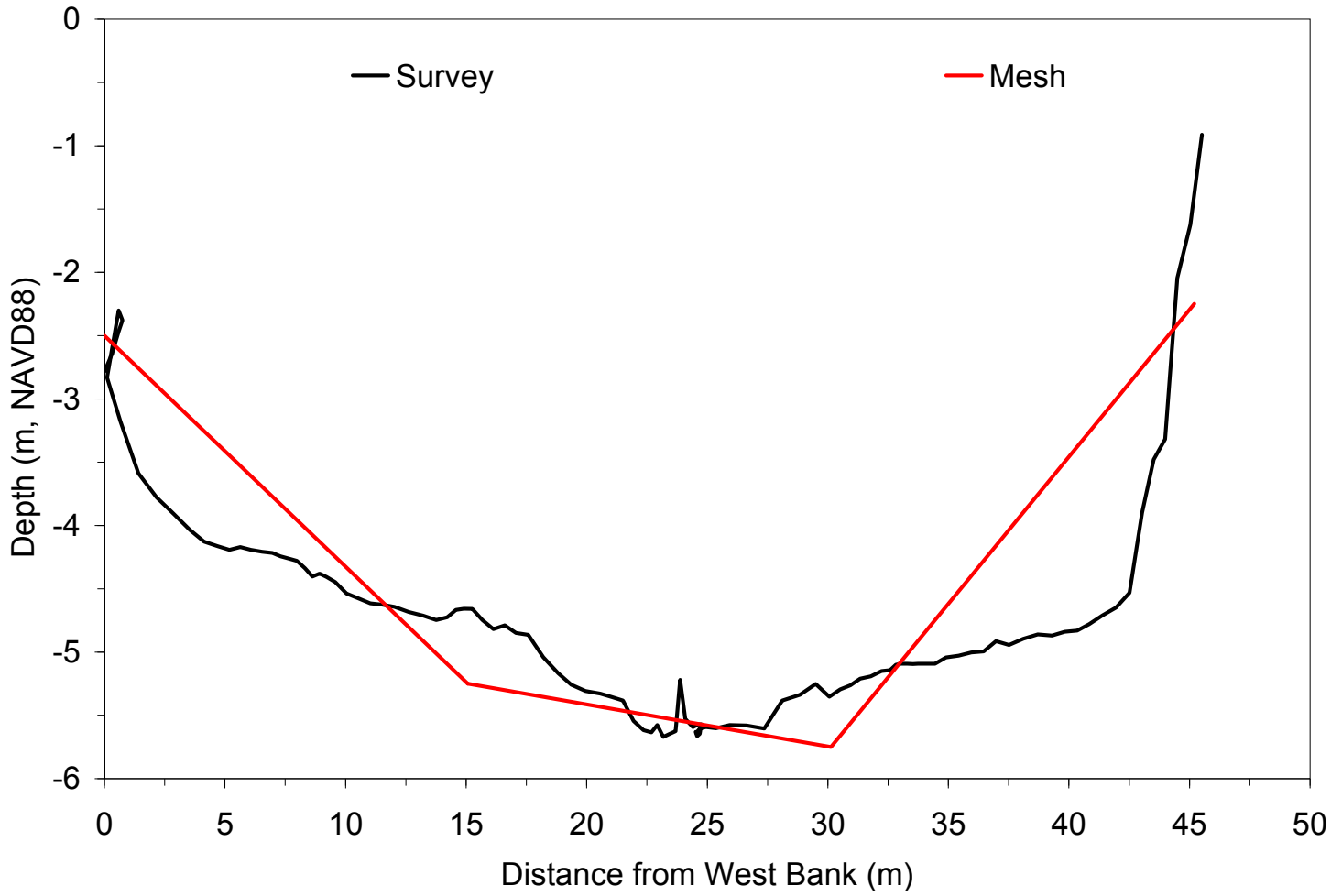

Figure C.6. Cross-sectional representation of Haulover Canal. The survey consists of 110 points; the mesh spans 3 elements across (4 points). The mesh represents the cross section with an area of 201.52 m^2, which compares to 213.93 m^2 estimated from the survey.

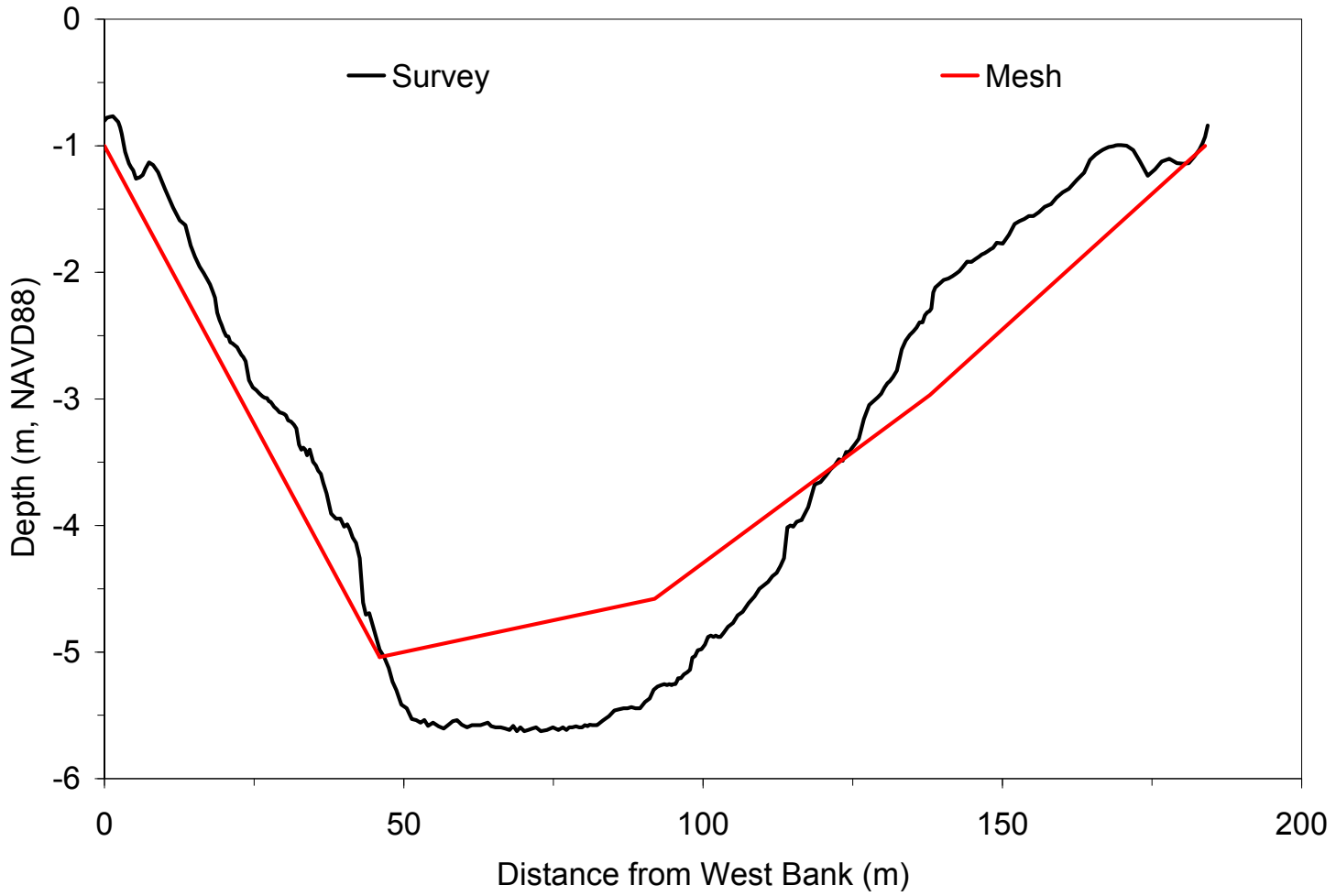

Figure C.7. Cross-sectional representation of Dragons Point. The survey consists of 296 points; the mesh spans 4 elements across (5 points). The mesh represents the cross section with an area of 624.66 m^2, which compares to 623.07 m^2 estimated from the survey.

APPENDIX D. TIDAL RESYNTHESIS PLOTS

The following plots are of resynthesized tidal signals for the 13 estuary stations reported in Table 11.2. The tidal resynthesis offers a qualitative comparison between computed and observed tides. Tidal resyntheses are carried out over 14 days in order to span a complete spring-neap tidal cycle.

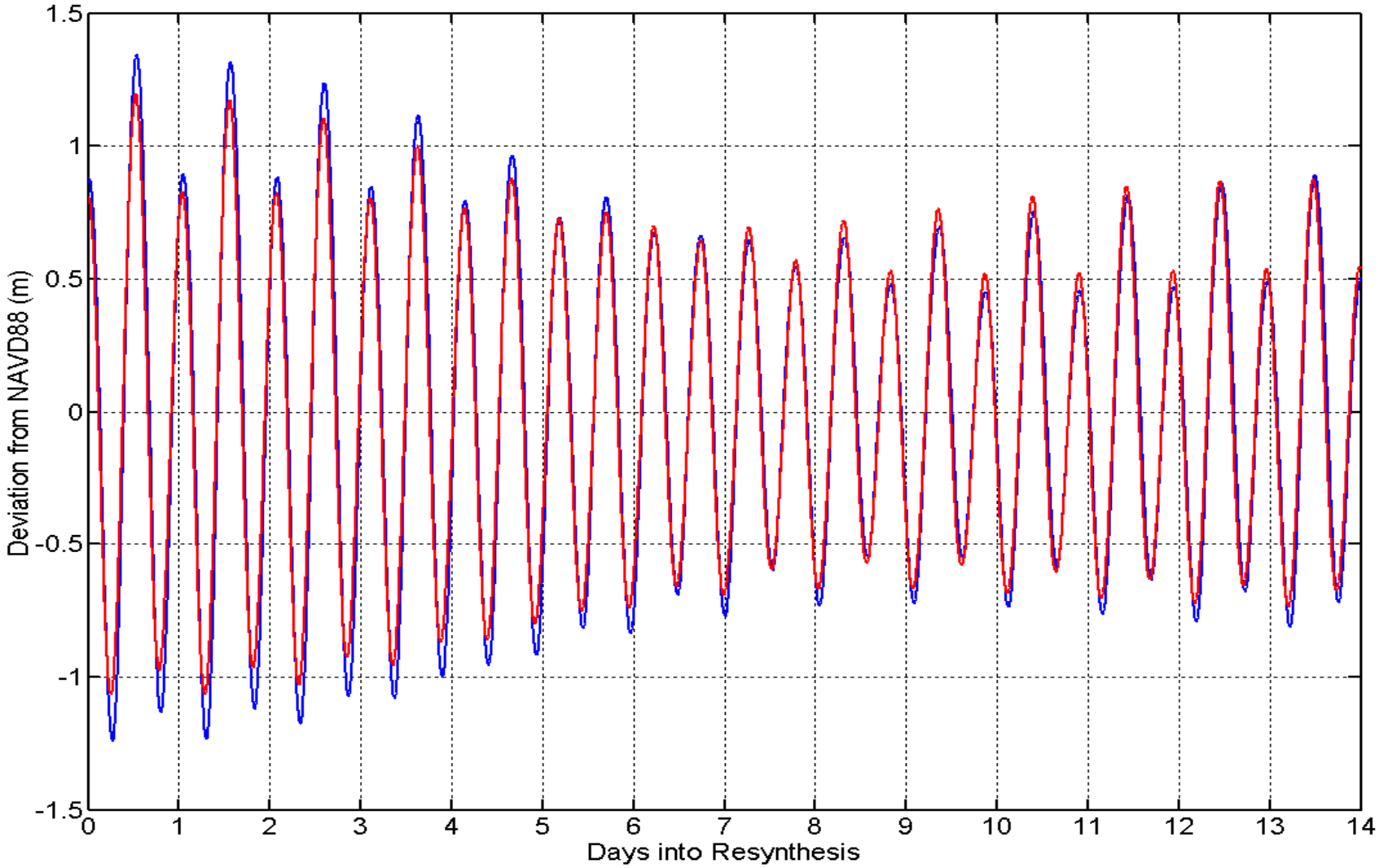

Figure D.1. Resynthesized tidal signals for station ChHr. The red curve corresponds to the simulated tide and the blue curve corresponds to the observed tide. Water levels are referenced to NAVD88.

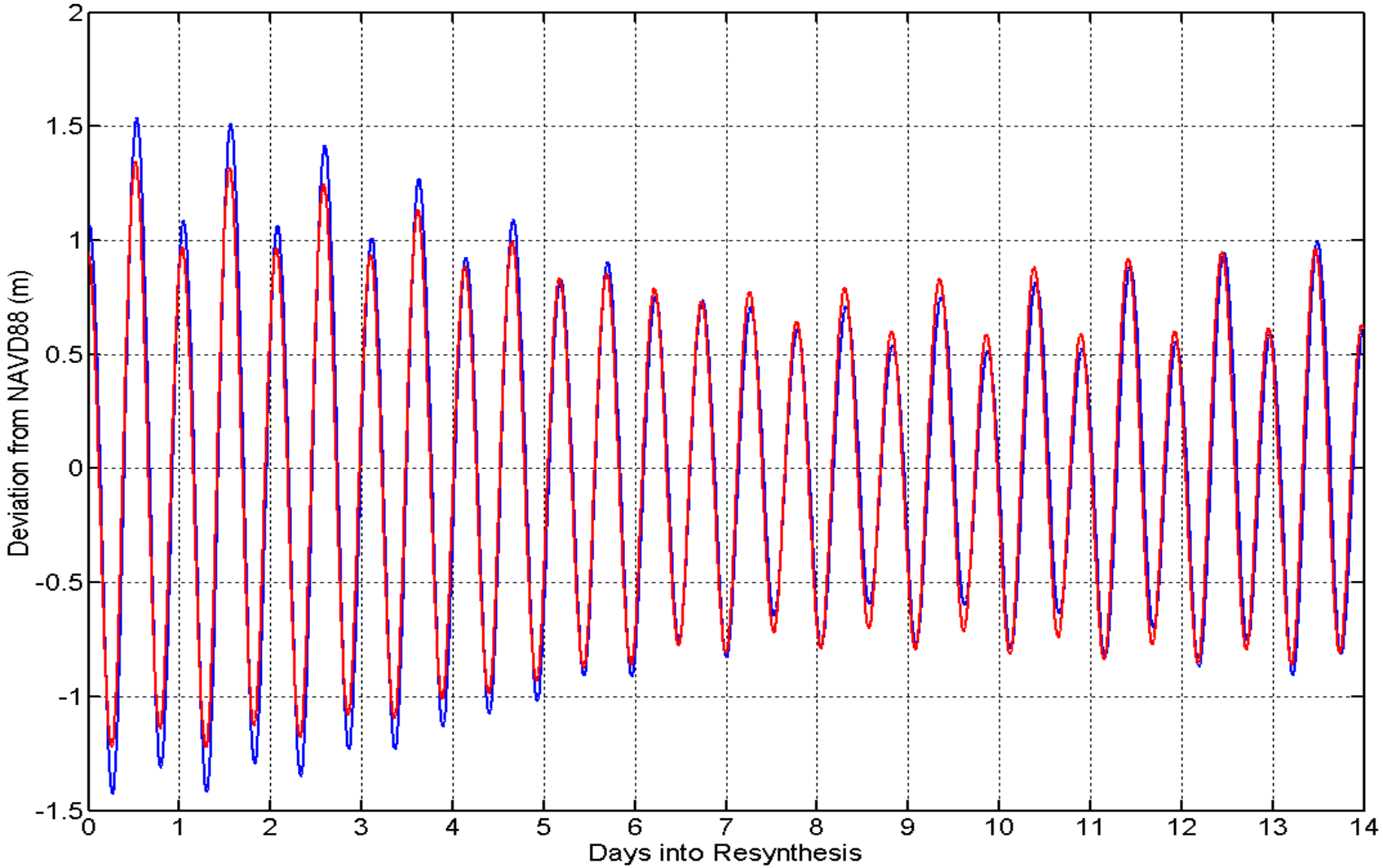

Figure D.2. Resynthesized tidal signals for station FRPS. The red curve corresponds to the simulated tide and the blue curve corresponds to the observed tide. Water levels are referenced to NAVD88.

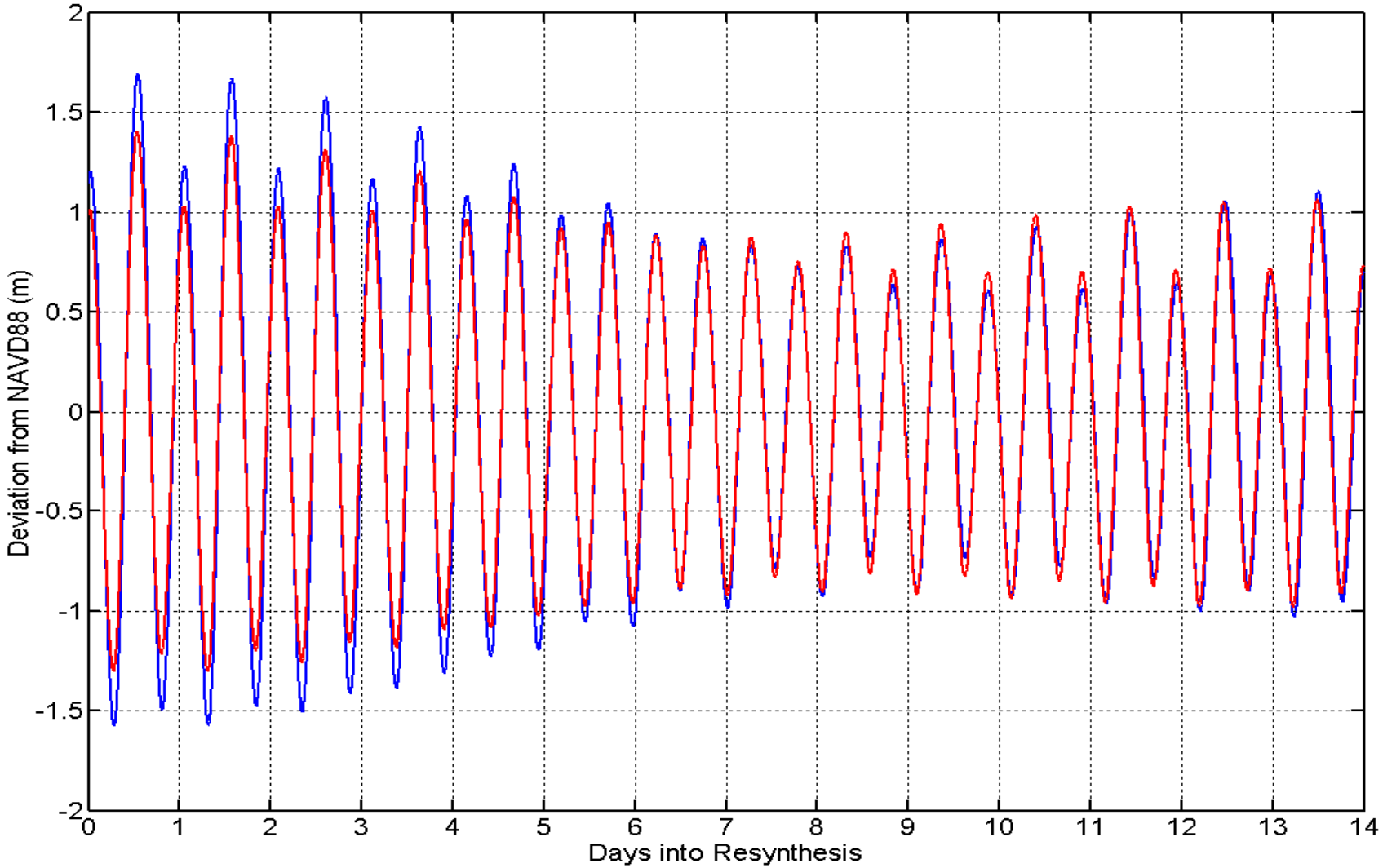

Figure D.3. Resynthesized tidal signals for station PUL. The red curve corresponds to the simulated tide and the blue curve corresponds to the observed tide. Water levels are referenced to NAVD88.

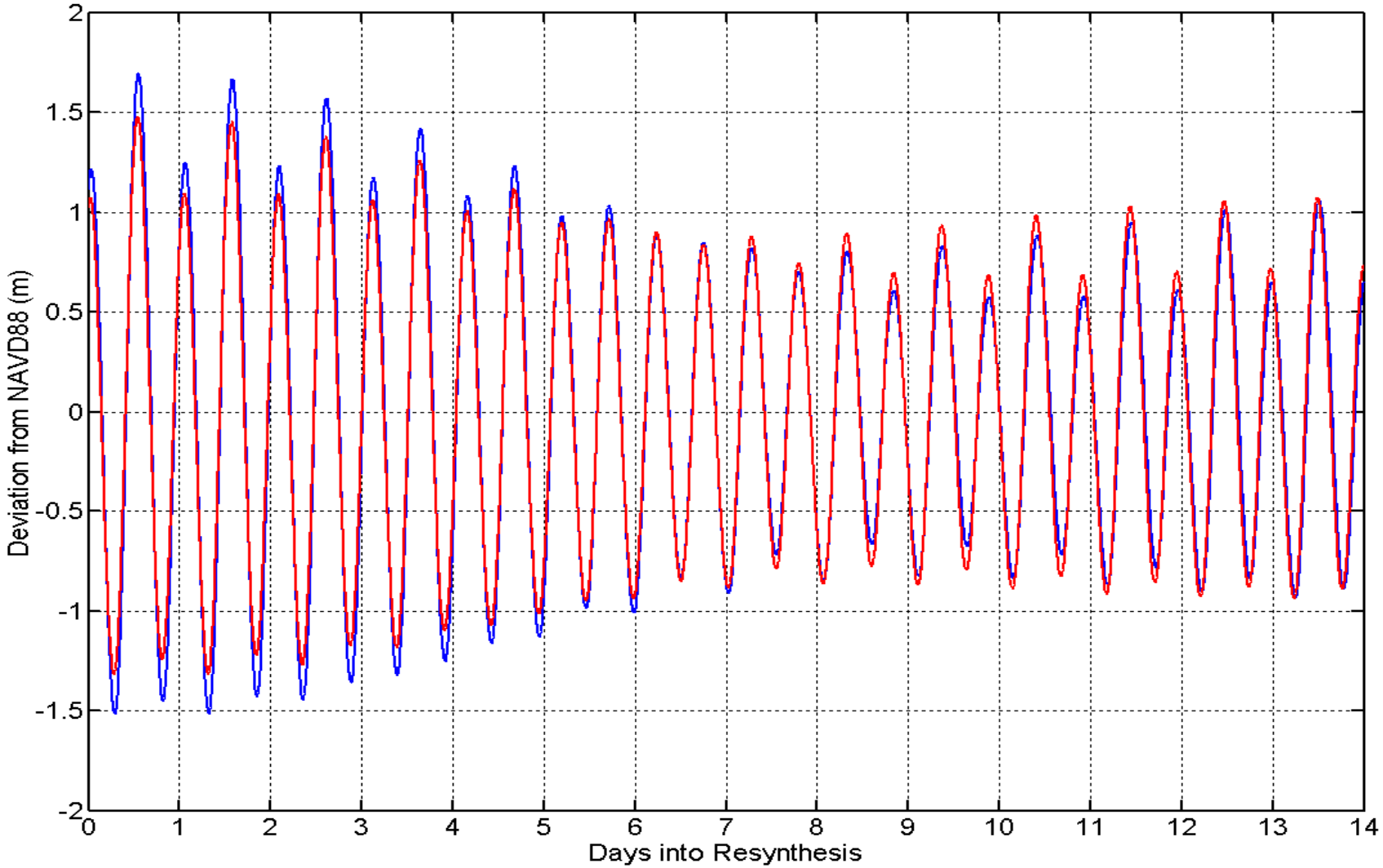

Figure D.4. Resynthesized tidal signals for station SIM. The red curve corresponds to the simulated tide and the blue curve corresponds to the observed tide. Water levels are referenced to NAVD88.

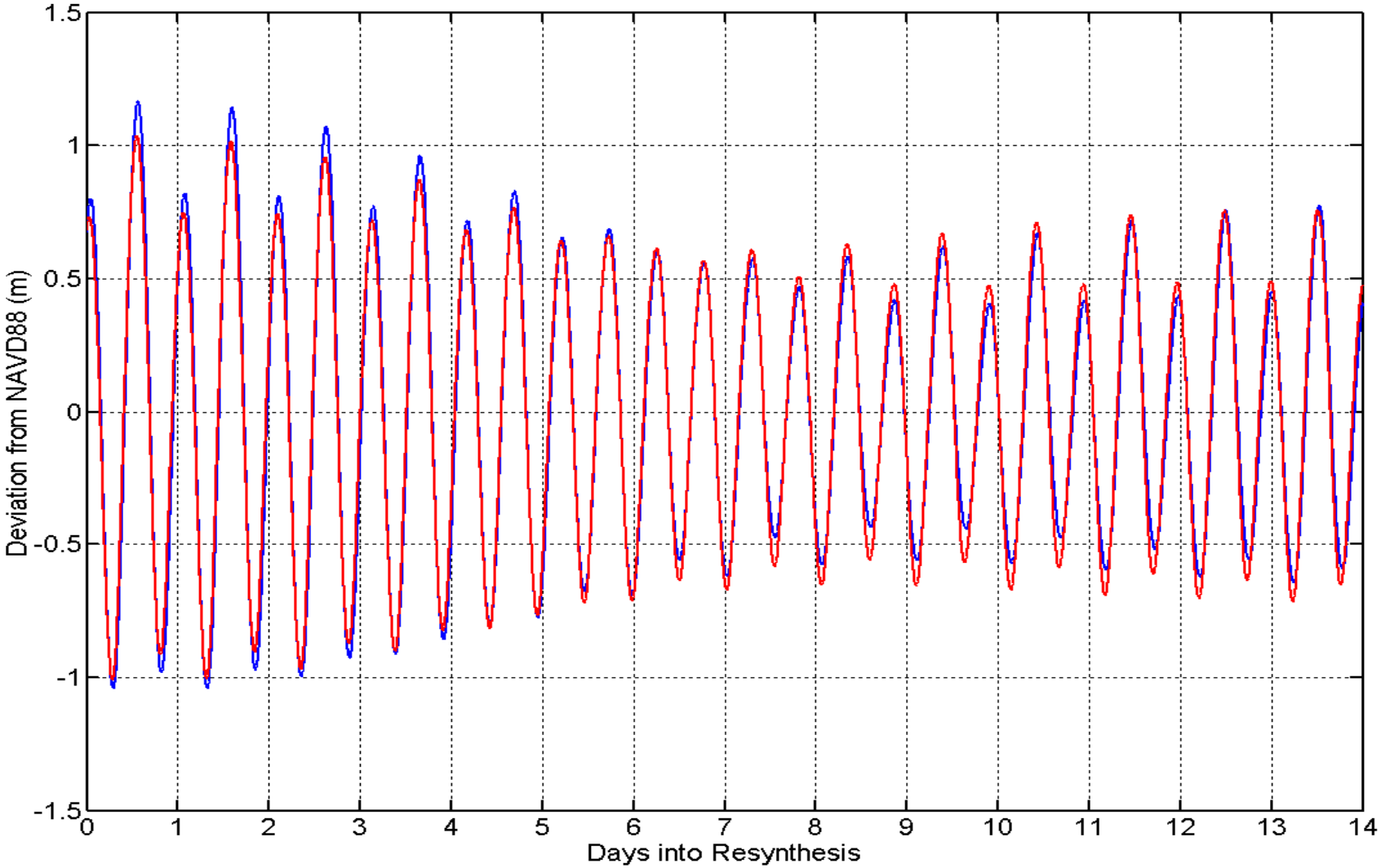

Figure D.5. Resynthesized tidal signals for station MAY. The red curve corresponds to the simulated tide and the blue curve corresponds to the observed tide. Water levels are referenced to NAVD88.

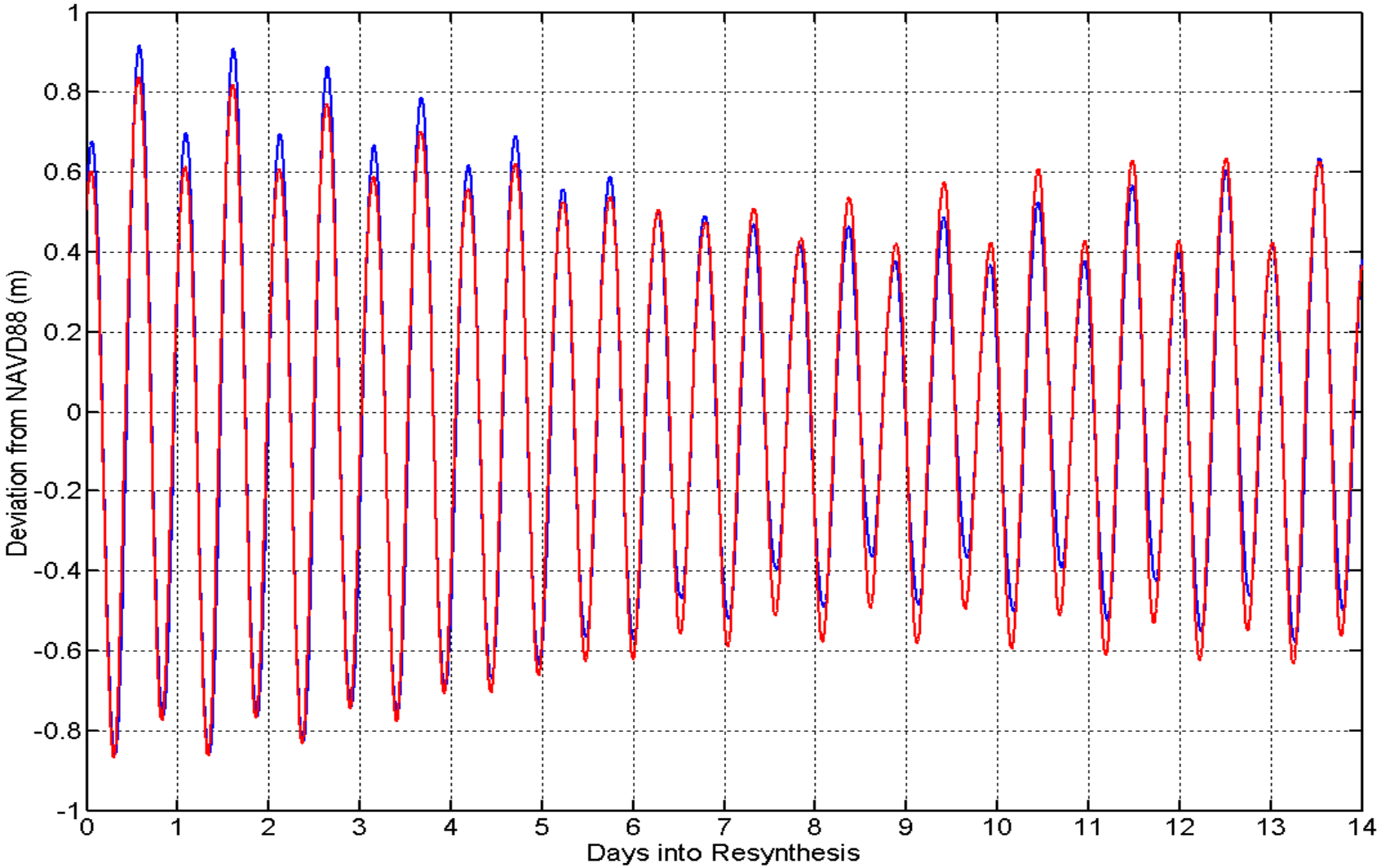

Figure D.6. Resynthesized tidal signals for station FUL. The red curve corresponds to the simulated tide and the blue curve corresponds to the observed tide. Water levels are referenced to NAVD88.

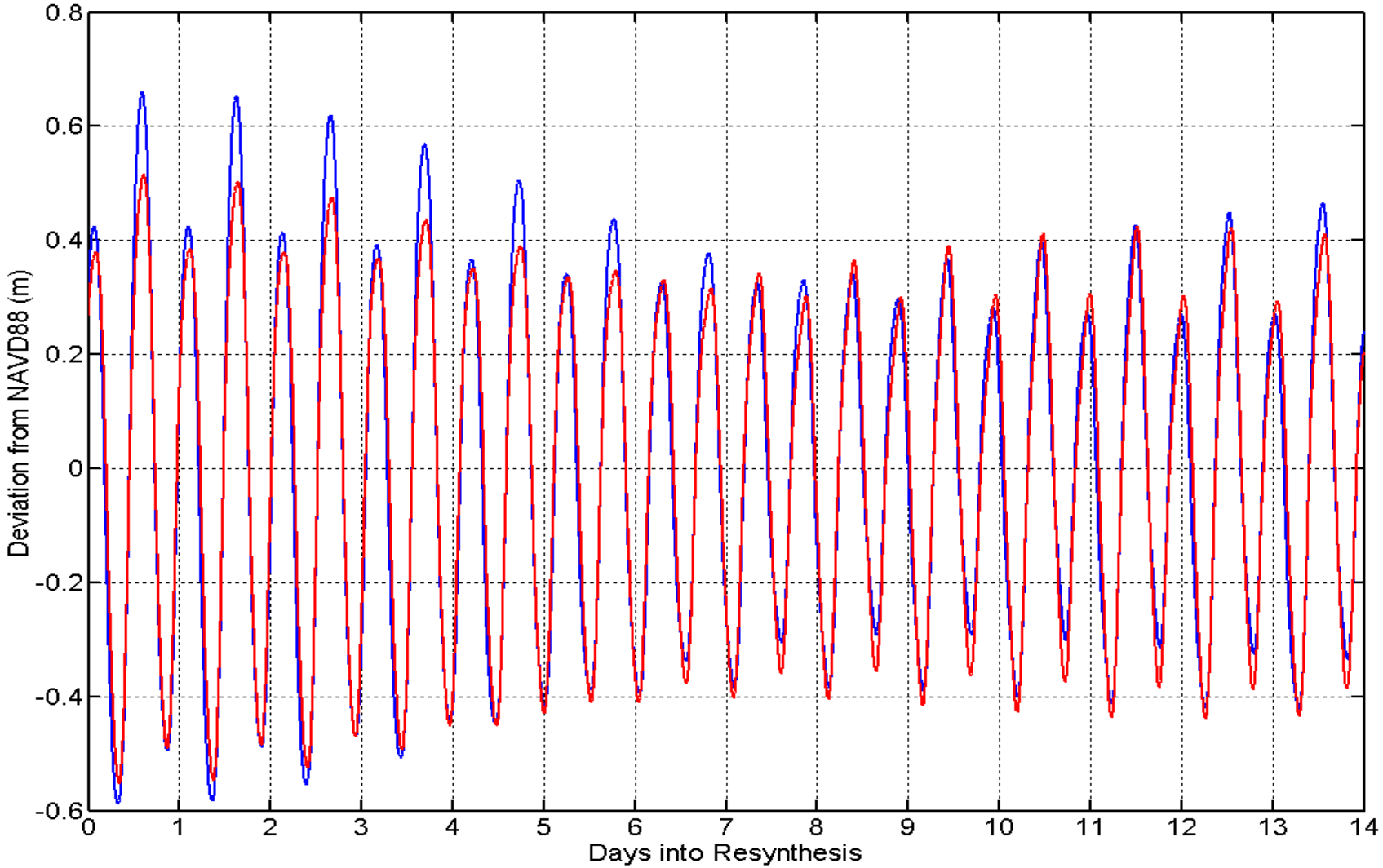

Figure D.7. Resynthesized tidal signals for station JAX. The red curve corresponds to the simulated tide and the blue curve corresponds to the observed tide. Water levels are referenced to NAVD88.

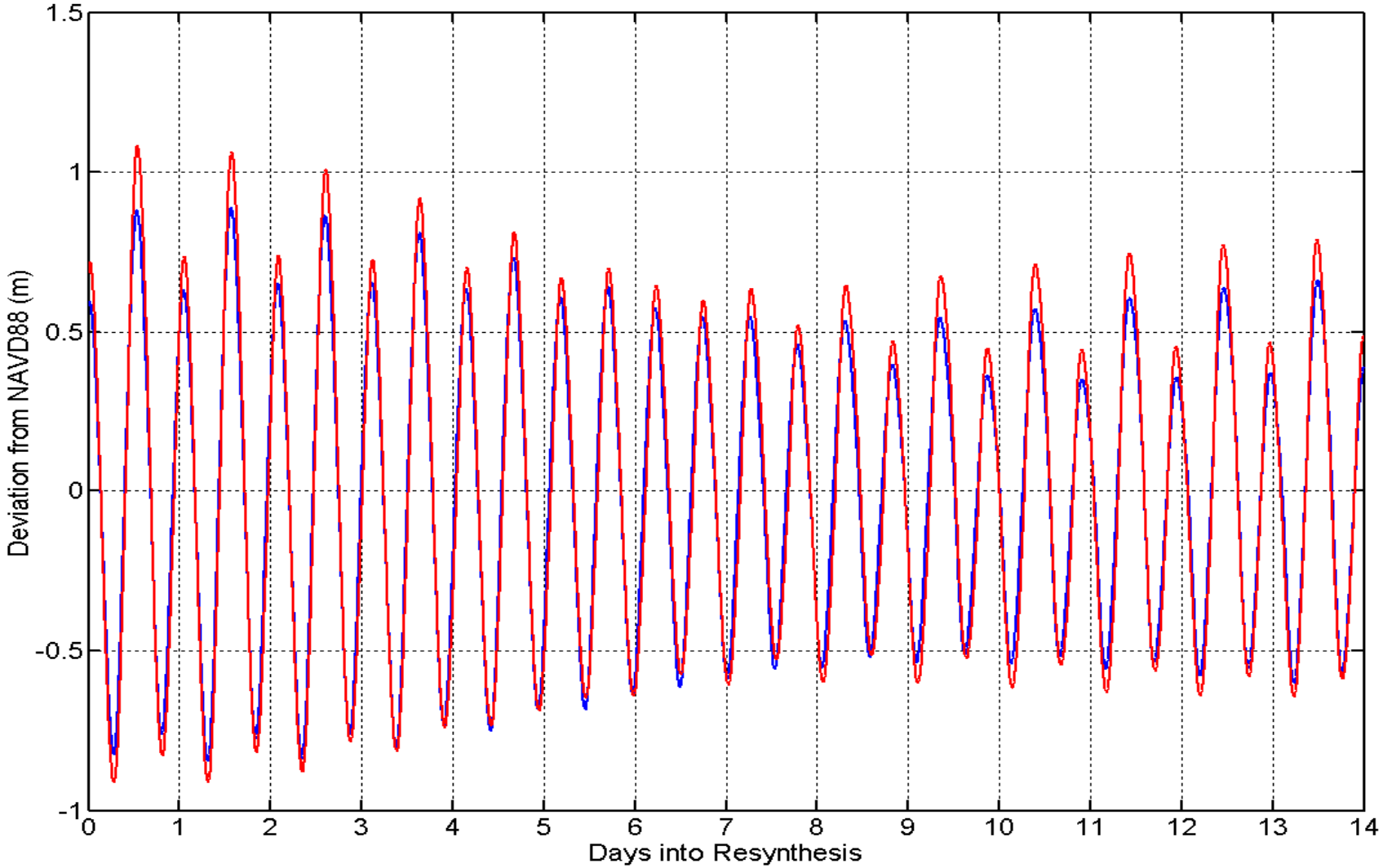

Figure D.8. Resynthesized tidal signals for station FtMz. The red curve corresponds to the simulated tide and the blue curve corresponds to the observed tide. Water levels are referenced to NAVD88.

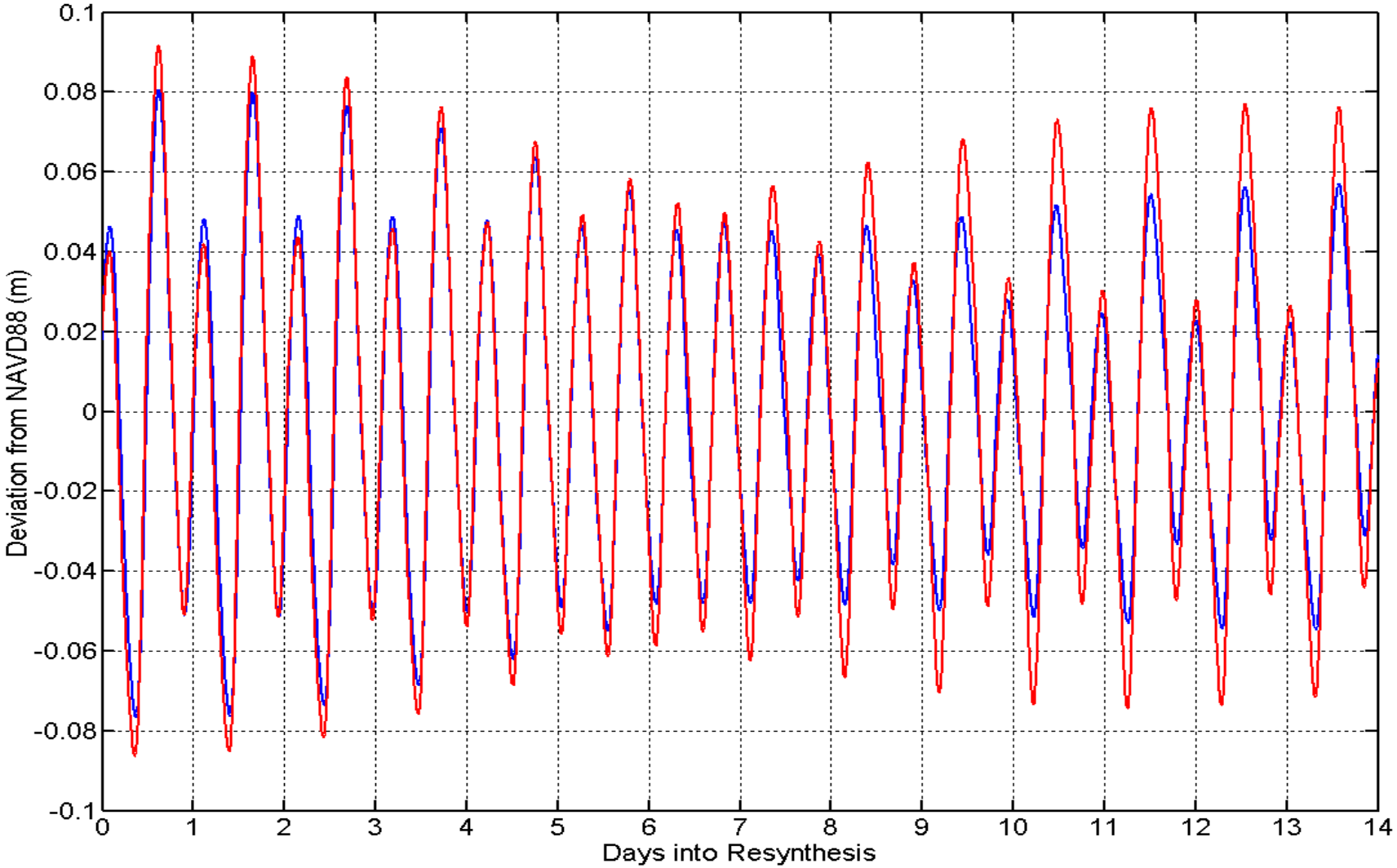

Figure D.9. Resynthesized tidal signals for station SEB. The red curve corresponds to the simulated tide and the blue curve corresponds to the observed tide. Water levels are referenced to NAVD88.

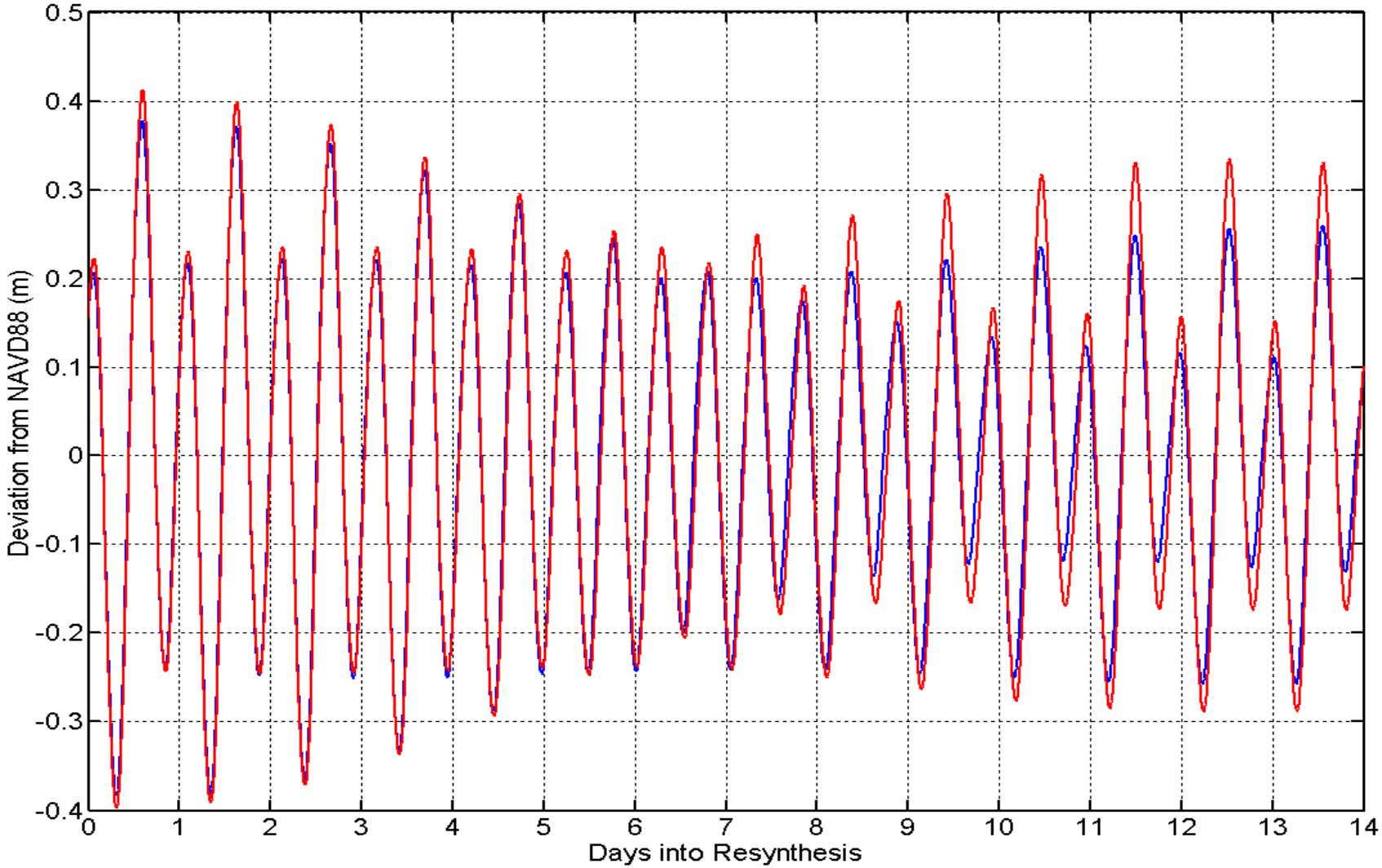

Figure D.10. Resynthesized tidal signals for station FtP. The red curve corresponds to the simulated tide and the blue curve corresponds to the observed tide. Water levels are referenced to NAVD88.

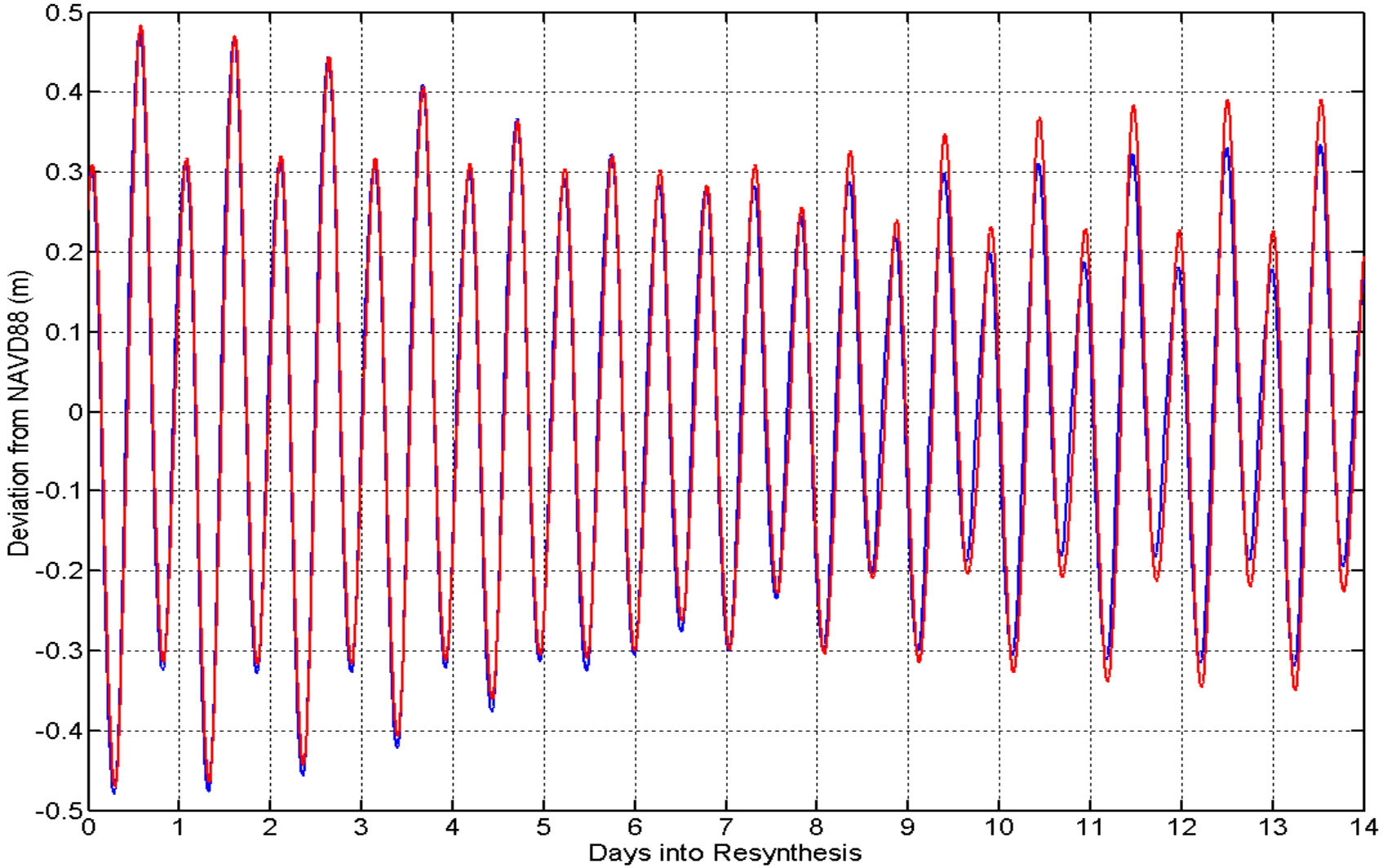

Figure D.11. Resynthesized tidal signals for station LUC. The red curve corresponds to the simulated tide and the blue curve corresponds to the observed tide. Water levels are referenced to NAVD88.

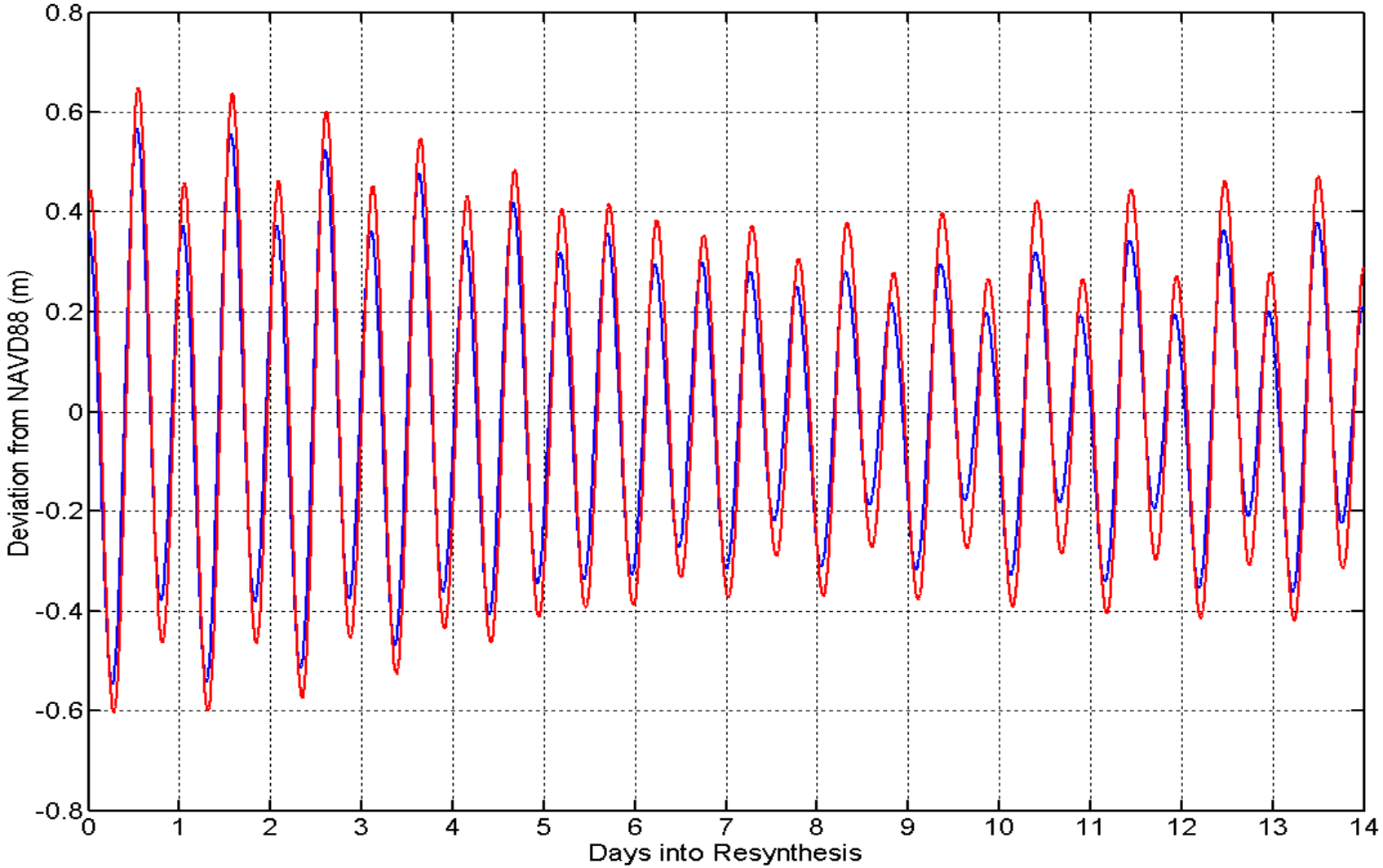

Figure D.12. Resynthesized tidal signals for station CGD. The red curve corresponds to the simulated tide and the blue curve corresponds to the observed tide. Water levels are referenced to NAVD88.

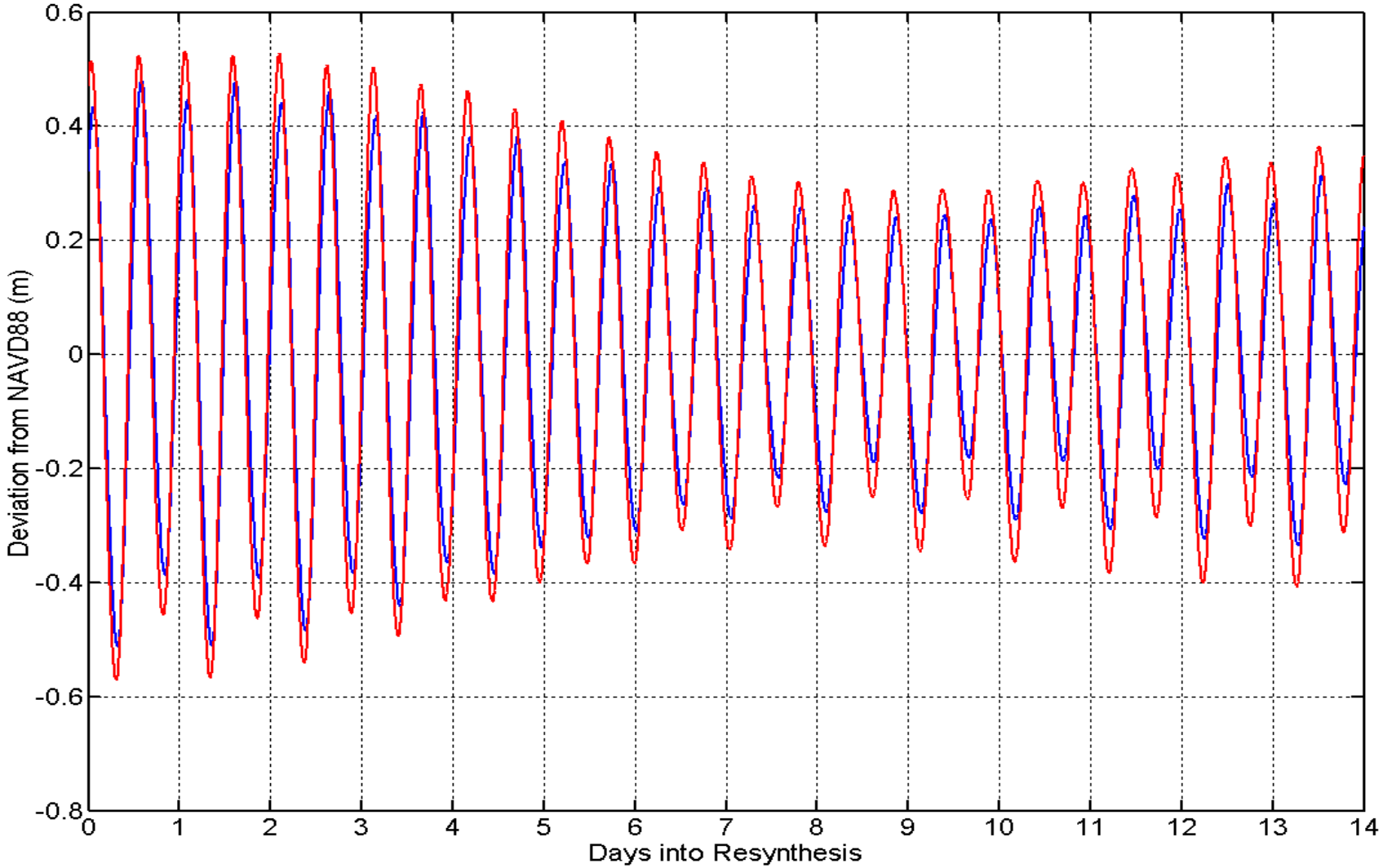

Figure D.13. Resynthesized tidal signals for station BIS. The red curve corresponds to the simulated tide and the blue curve corresponds to the observed tide. Water levels are referenced to NAVD88.

LIST OF REFERENCES

Alexander, C. E., Brontman, M. A., and Field, D. W. (1986). "An inventory of coastal wetlands in the USA." *Technical Report*, National Oceanic and Atmospheric Administration, National Ocean Service, U.S. Department of Commerce, Washington, DC.

American Society of Mechanical Engineers. (2006). "Guide for verification and validation in computational solid mechanics." *ASME V&V 10-2006*, American Society of Mechanical Engineers, New York, New York.

Arcement, G. J., and Schneider, V. R. (1989). "Guide for selecting Manning's roughness coefficients for natural channels and floodplains." *Water Supply Paper 2339*, United States Geological Survey, Tallahassee, Florida.

Atkinson, L. P., and Menzel, D. W. (1985). "Introduction: Oceanography of the southeast United States continental shelf." *Oceanography of the Southeastern U.S. Continental Shelf*, L. P. Atkinson, D. W. Menzel, and K. A. Bush, eds., AGU Press, Washington, DC, 1–19.

Aubrey, D. G., and Speer, P. E. (1985). "A study of non-linear tidal propagation in shallow inlet/estuarine systems, I: Observations." *Estuarine, Coastal and Shelf Science*, 21, 185–205.

Bacopoulos, P., Funakoshi, Y., Hagen, S. C., Cox, A. T., and Cardone, V. J. (2009). "The role of meteorological forcing on the St. Johns River (northeastern Florida)." *Journal of Hydrology*, 369, 55–70.

Bacopoulos, P., and Hagen, S. C. (2009). "Tidal simulations for the Loxahatchee River estuary (Southeastern Florida): On the influence of the Atlantic Intracoastal Waterway versus the

surrounding tidal flats." *Journal of Waterway, Port, Coastal, and Ocean Engineering*, in press.

Barnes, H. H. (1967). "Roughness characteristics of natural channels." *Water Supply Paper 1849*, United States Geological Survey, Tallahassee, Florirda.

Battisti, D. S., and Clarke, A. J. (1982). "A simple method for estimating barotropic tidal currents on continental margins with specific application to the M2 tide off the Atlantic and Pacific coasts of the United States." *Journal of Physical Oceanography*, 12, 8–16.

Blanton, B. O., Werner, F. E., Seim, H. E., Luettich, R. A. Jr., Lynch, D. R., Smith, K. W., Voulgaris, G., Bingham, F. M., and Way, F. (2004). "Barotropic tides in the South Atlantic Bight." *Journal of Geophysical Research*, 109(C12024), 1–17.

Blanton, J. O. (1980). "The transport of freshwater off a multi-inlet coastline." *Modeling of Estuaries and Wetland Processes*, P. Hamilton and K. B. MacDonald, Plenum Publishing, New York, New York, 49–64. Wiegert, R. G., and Freeman, B. J. (1990). "Tidal salt marshes of the Southeast Atlantic coast: A community profile." *Biological Report 80(7.29)*, Fish and Wildlife Service, U.S. Department of the Interior, Slidell, Louisiana.

Blanton, J. O. (1981). "Ocean currents along a nearshore frontal zone on the continental shelf of the southeastern United States." *Journal of Physical Oceanography*, 11, 1627–1637.

Blanton, J. O., and Atkinson, L. P. (1983). "Transport and fate of river discharge on the continental shelf of the southeastern United States." *Journal of Geophysical Research*, 88(C8), 4730–4738.

Blanton, J. O., Schwing, F. B., Weber, A. H., Pietrafesa, L. J., and Hayes, D. W. (1985). "Wind stress climatology in the South Atlantic Bight." *Oceanography of the Southeastern U.S.*

Continental Shelf, L. P. Atkinson, D. W. Menzel, and K. A. Bush, eds., AGU Press, Washington, DC, 10–22.

Blumberg, A. F., and Mellor, G. L. (1987). "A description of a three-dimensional coastal ocean circulation model." *Three-Dimensional Coastal Ocean Models*, N. S. Heaps, ed., AGU Press, Washington, DC, 1–16.

Boicourt, W. C., Wiseman, W. J. Jr., Valle-Levinson, A., and Atkinson, L. P. (1998). "Continental shelf of the Southeastern United States and the Gulf of Mexico: In the shadow of the western boundary current." *The Sea, Volume 11*, A. R. Robinson and K. H. Brink, eds., John Wiley & Sons, Inc., New York, New York, 135–182.

Chalmers, A. G. (1982). "Soil dynamics and the productivity of *Spartina alterniflora*." *Estuarine Comparisons*, V. S. Kennedy, ed., Academic Press, New York, New York, 231–243.

Chow, V. T. (1959). "Open-channel hydraulics." McGraw-Hill, New York, New York.

Coastal Assessment and Data Synthesis System. (1999). "Physical and hydrological characteristics of coastal watersheds." *National Coastal Assessments Branch, Special Projects Report*, National Ocean Service, National Oceanic and Atmospheric Administration, Silver Spring, Maryland.

Clarke, A. J. (1991). "The dynamics of barotropic tides over the continental shelf and slope (review)." *Tidal Hydrodynamics*, B. B. Parker, ed., John Wiley & Sons, Inc., New York, New York, 79–108.

Clarke, A. J., and Battisti, D. S. (1981). "The effect of continental shelves on tides." *Deep Sea Research*, 28, 665–682.

Cowen, W. L. (1956). "Estimating hydraulic roughness coefficients." *Agricultural Engineering*, 37(7), 473–475.

Crawford, W. G. Jr. (2006). “Florida’s big dig: The Atlantic Intracoastal Waterway from Jacksonville to Miami, 1881 to 1935.” Florida Historical Society Press, Cocoa, Florida.

Critcher, T. S. (1967). “The wildlife values of North Carolina estuarine lands and waters.” *North Carolina Wildlife Resources Commission*, Raleigh, North Carolina.

Dame, R., Alber, M., Allen, D., Mallin, M., Montague, C., Lewitus, A., Chalmers, A., Gardner, R., Gilman, C., Kjerfve, B., Pinckney, J., and Smith, N. (2000). “Estuaries of the South Atlantic coast of North America: Their geographical signatures.” *Estuaries*, 23(6), 793–819.

Dietsche, D., Hagen, S. C., and Bacopoulos, P. (2007). “Storm surge simulations for Hurricane Hugo (1989): On the significance of inundation areas.” *Journal of Waterway, Port, Coastal, and Ocean Engineering*, 133(3), 183–191.

Eleuterius, L. N. (1976). “The distribution of *Juncus roemerianus* in the salt marshes of North America.” *Chesapeake Science*, 17, 289–292.

Fathi-Moghadam, M., and Kouwen, N. (1997). “Nonrigid, nonsubmerged, vegetative roughness on floodplains.” *Journal of Hydraulic Engineering*, 123(1), 51–57.

Florida Department of Transportation. (1985). “Florida land use, cover and forms classification system.” *Procedure Report 550-010-001-A*, State Topographic Bureau, Thematic Mapping Section, Florida Department of Transportation, Tallahassee, Florida.

Foreman, M. G. G. (1978). “Manual for tidal currents analysis and prediction.” *Pacific Marine Science Report 78-6*, Institute of Ocean Sciences, Patricia Bay, Victoria, British Columbia.

Gonella, J. (1972). “A rotary-component method for analysing meteorological and oceanographic vector time series.” *Deep-Sea Research*, 19, 833–846.

Gray, W. G. (1982). “Some inadequacies of finite element models as simulators of two-dimensional circulation.” *Advances in Water Resources*, 5(3), 171–177.

Hagen, S. C., Zundel, A. K., and Kojima, S. (2006). “Automatic, unstructured mesh generation for tidal calculations in a large domain.” *International Journal of Computational Fluid Dynamics*, 20(8), 593–608.

Homer, C., Huang, C., Yang, L., Wylie, B., and Coan, M. (2004). “Development of a 2001 national land-cover database for the United States.” *Photogrammetric Engineering and Remote Sensing*, 70(7), 829–840.

Hsu, M. H., Kuo, A. Y., Kuo, J. T., and Liu, W. C. (1999). “Procedure to calibrate and verify numerical models of estuarine hydrodynamics.” *Journal of Hydraulic Engineering*, 125(2), 166–182.

Kinnmark, I. P. E. (1985). “The shallow water wave equations: Formulation, analysis and application.” *Lecture Notes in Engineering 15*, C. A. Brebbia and S. A. Orszag, eds., Springer-Verlag, 15, New York, New York, 1–187.

Kolar, R. L., and Gray, W. G. (1990). “Shallow water modeling in small water bodies.” *Computational Methods in Surface Hydrology*, Gambolati et al., eds., WIT Press, Billerica, Massachusetts, 149–155.

Kolar, R. L., Gray, W. G., Westerink, J. J., and Luettich, R. A. Jr. (1994a). “Shallow water modeling in spherical coordinates: Equation formulation, numerical implementation, and application.” *Journal of Hydraulic Research*, 32(1), 3–24.

Kolar, R. L., Westerink, J. J., Cantekin, M. E., and Blain, C. A. (1994b). “Aspects of nonlinear simulations using shallow-water models based on the wave continuity equation.” *Computers and Fluids*, 23(3), 523–538.

Kundu, P. K., Blanton, J. O., and Janopaul, M. M. (1981). "Analysis of current observations on the Georgia shelf." *Journal of Physical Oceanography*, 11, 1139–1149.

Luettich, R. A. Jr., and Westerink, J. J. (2006a). "ADCIRC: A parallel advanced circulation model for oceanic, coastal and estuarine waters; users manual for version 45.08." [Available online at http://adcirc.org/document/ADCIRC_title_page.html.]

Luettich, R. A. Jr., and Westerink, J. J. (2006b). "Formulation and numerical implementation of the 2D/3D ADCIRC finite element model, version 44.XX." [Available online at http://adcirc.org/document/ADCIRC_title_page.html.]

Luettich, R. A. Jr., Westerink, J. J., and Scheffner, N. W. (1992). "ADCIRC: An advanced three-dimensional circulation model for shelves, coasts, and estuaries, I: Theory and methodology of ADCIRC-2DDI and ADCIRC-3DL." *Technical Report DRP-92-6*, U.S. Army Corps of Engineers, Waterways Experiment Station, Vicksburg, Mississippi.

Lynch, D. R., and Gray, W. G. (1979). "A wave equation model for finite element tidal computations." *Computers and Fluids*, 7, 207–228.

Lynch, D. R., Smith, K. W., Blanton, J. O., Werner, F. E., and Luettich, R. A. Jr. (2004). "Forecasting the coastal ocean: Resolution, tide and operational data in the South Atlantic Bight." *Journal of Atmospheric and Oceanic Technology*, 21(7), 1074–1085.

Marshall, H. L. (1974). "Irregularly-flooded marsh." *Coastal Ecosystems of the United States, Volume 2*, H. T. Odum et al., eds., The Conservation Foundation, Washington, DC.

Mattocks, C., Forbes, C., and Ran, L. (2006). "Design and implementation of a real-time storm surge and flood forecasting capability for the state of North Carolina." *UNC-CEP Technical Report*, University of North Carolina, Chapel Hill, North Carolina.

Lee, T. N., and Brooks, D. (1979). “Initial observations of current, temperature, and coastal sea level response to atmospheric and Gulf Stream forcing.” *Geophysical Research Letters*, 6, 321–324.

Lee, T. N., Ho, W. J., Kourafalou, V., and Wang, J. D. (1984). “Circulation on the southeast U.S. continental shelf, I: Subtidal response to wind and Gulf Stream forcing.” *Journal of Physical Oceanography*, 14, 1001–1012.

Parker, B. B. (1991). “The relative importance of the various nonlinear mechanisms in a wide range of tidal interactions (review).” *Tidal Hydrodynamics*, B. B. Parker, ed., John Wiley & Sons, Inc., New York, New York, 237–268.

Parkman, A. (1983). “History of the waterways of the Atlantic coast of the United States.” *Navigation History NWS-83-10*, National Waterways Study, U.S. Army Engineer Water Resources Support Center, Institute for Water Resources, Alexandria, Virginia.

Pietrafesa, L. J., Blanton, B. O., Wang, J. D., Kourafalou, V. H., Lee, T. N., and Bush, K. A. (1985). “The tidal regime in the South Atlantic Bight.” *Oceanography of the Southeastern U.S. Continental Shelf*, L. P. Atkinson, D. W. Menzel, and K. A. Bush, eds., AGU Press, Washington, DC, 63–76.

Pugh, D. T. (2004). “Changing sea levels: Effects of tides, weather and climate.” Cambridge University Press, Cambridge, United Kingdom.

Redfield, A. (1958). “The influence of the continental shelf on the tides of the Atlantic coast of the United States.” *Journal of Marine Research*, 17, 432–448.

Reid, R. O. (1990). “Tides and storm surges.” *Handbook of Coastal and Ocean Engineering, Volume 1: Wave Phenomena and Coastal Structures*, J. B. Herbich, ed., Gulf Publishing Company, Houston, Texas, 533–590.

Schwiderski, E. W. (1980). “On charting global ocean tides.” *Reviews of Geophysics and Space Physics*, 18(1), 243–268.

Seim, H. E. (2000). “Implementation of the South Atlantic Bight synoptic offshore observational network.” *Oceanography*, 13(2), 18–23.

Sucsy, P. V., and Morris, F. W. (2002). “Calibration of a three-dimensional circulation and mixing model of the Lower St. Johns River.” *Technical Report*, St. Johns River Water Management District, Palatka, Florida.

Tabeau, P. A., and Lee, T. N. (1979). “Wind induced circulation on the Georgia shelf.” *Technical Report 79003*, University of Miami, Miami, Florida.

Taylor, G. I. (1919). “Tidal friction in the Irish Sea.” *Philosophical Transactions of the Royal Society of London*, 220A, 1–33.

The History Channel (2006). “Atlantic Intracoastal Waterway (DVD documentary, AAE-76312).” *A&E Television Networks*, New York, New York.

Vernberg, F. J., Vernberg, W. G., Blood, E., Fortner, A., Fulton, M., McKellar, H., Michener, W., Scott, G., Siewicki, T., and El Figi, K. (1992). “Impact of urbanization on high-salinity estuaries in the southeastern United States.” *Netherlands Journal of Sea Research*, 30, 239–248.

Walters, R. A., and Werner, F. E. (1991). “Nonlinear generation of overtides, compound tides, and residuals.” *Tidal Hydrodynamics*, B. B. Parker, ed., John Wiley & Sons, Inc., New York, New York, 297–320.

Werner, F. E., and Lynch, D. R. (1987). “Field verification of wave equation tidal dynamics in the English channel and southern North Sea.” *Advances in Water Resources*, 10(3), 115–130.

Westerink, J. J., Luettich, R. A., Feyen, J. C., Atkinson, J. H., Dawson, C., Roberts, H. J., Powell, M. D., Dunion, J. P., Kubatko, E. J., and Pourtaheri, H. (2008). "A basin- to channel-scale unstructured grid hurricane storm surge model applied to Southern Louisiana." *Monthly Weather Review*, 136, 833–864.

Westerink, J. J., Luettich, R. A. Jr., and Muccino, J. C. (1994). "Modeling tides in the western North Atlantic using unstructured graded grids." *Tellus*, 46A, 178–199.

Zundel, A. K. (2006). "Surface-water Modeling System 9.2, tutorials." Environmental Modeling Research Laboratory, Brigham Young University, Provo, Utah.